Nanoscale

ROYAL SOCIETY OF CHEMISTRY

REVIEW

View Article Online
View Journal | View Issue

Check for updates

Cite this: *Nanoscale*, 2025, **17**, 20606

Negative differential resistance in memristive systems: historical evolution, mechanisms and neuromorphic applications of niobium oxide devices

Hongyi Lu,†[a] Shiyu Xie,†[a] Weijian Zhang, *†[a] Yue Chen, *[a] Jianming Tao,[a,b] Chinmayee Mandar Mhaskar, [d] Ayan Roy Chaudhuri, *[d] Yingbin Lin, [a,c] Jiaxin Li,[a,c] Sanjay Mathur *[b] and Zhigao Huang [a,c,e]

Received 11th June 2025,
Accepted 11th August 2025

DOI: 10.1039/d5nr02491a

rsc.li/nanoscale

The synergy between the memristive effect and negative differential resistance (NDR) offers promising prospects for advancing electronic devices and circuits. Predictable outcomes include the development of devices with improved performance and functionality that are applicable across a wide range of fields, from computing architecture to neuromorphic engineering. Despite the growing body of literature exploring this convergence, the effective implementation of the NDR effect in memristors faces many challenges. Several memristive materials—including VO_2, TaO_x, and chalcogenides—have demonstrated promising NDR effects. Among them, niobium oxide uniquely combines steep (<3 ns), endurable (>10^{12} cycles) negative differential resistance with biophysically plausible spiking dynamics—enabled by its dual current-controlled and thermally driven mechanisms—making it ideal for energy-efficient neuromorphic primitives. This paper reviews the complex phenomenon of NDR and its applications in niobium oxide memristors while analyzing its potential future applications in electronic systems. By outlining the NDR effect and its applications in niobium oxide memristors, this paper aims to provide valuable insights for researchers in the field.

1 Introduction

In traditional complementary metal oxide semiconductor (CMOS) technology, complex auxiliary circuits and a large number of capacitors are often employed in neural circuits to mimic the biological dynamics of neurons.[1–3] However, due to limitations in the space and energy efficiency of integrated circuits, this approach is not suitable for constructing scalable artificial neural circuits. In recent years, memristive technology has rapidly emerged as a potential alternative to traditional CMOS technology, which is facing fundamental limitations in its development in neuromorphic computing.

Since the first demonstration of oxide-based resistive switching devices as memristors in 2008, memristive devices have gained significant attention due to their biomimetic memory properties and promising improvements in energy efficiency in computing applications.[4] For instance, the training of deep neural networks (DNNs) using von Neumann architecture and high-precision digital computations leads to substantial energy consumption stemming from data transfers between the processor and off-chip memory. Although cloud computing platforms handle such demanding training tasks, their energy-intensive nature poses a challenge for edge computing deployments. By contrast, memristor-driven neuromorphic computing mitigates data movement through its in-memory computing design and analog computing approach. It has also been demonstrated that a memristor crossbar array can store analog synaptic weights and efficiently perform parallel vector-matrix multiplication (VMM) operations in a single computational step, achieving time- and energy-efficient on-chip data processing.[5]

To date, memristor devices have leveraged various switching mechanisms, including filamentary switching, interface-

---

[a] *College of Physics and Energy, Fujian Normal University, Fujian Provincial Key Laboratory of Quantum Manipulation and New Energy Materials, Fuzhou, 350117, China. E-mail: qbx20230089@yjs.fjnu.edu.cn, yuechen@fjnu.edu.cn*
[b] *Institute of Inorganic and Materials Chemistry, University of Cologne, Greinstr.6, 50939 Cologne, Germany. E-mail: sanjay.mathur@uni-koeln.de*
[c] *Fujian Provincial Engineering Technical Research Centre of Solar-Energy Conversion and Stored Energy, Fuzhou, 350117, China*
[d] *Materials Science Centre, Indian Institute of Technology Kharagpur, Kharagpur 721302, India. E-mail: ayan@matsc.iitkgp.ac.in*
[e] *Fujian Provincial Collaborative Innovation Centre for Advanced High-Field Superconducting Materials and Engineering, Fuzhou, 350117, China*
† These authors contributed equally to this perspective review.

type switching, Mott transition-based switching, phase change, and electrically driven nonlinear conduction.[4] Each mechanism contributes uniquely to device performance, with trade-offs in speed, stability, and energy efficiency. Memristors based on negative differential resistance (NDR), a unique electrical property where an increase in voltage across a device results in a decrease in the current flowing through it, stand out for their fast, tunable switching and oscillatory behavior, which is ideal for neuromorphic computing. Unlike filamentary mechanisms prone to degradation or phase change mechanisms requiring thermal cycling, NDR offers stable, energy-efficient switching and can mimic neural spiking, making it particularly advantageous for dense, adaptive neural networks and real-time processing in neuromorphic systems. More importantly, NDR is vital for memristors in neuromorphic computing because it enables oscillatory behavior and threshold-dependent transitions, which are essential for mimicking neural functions, such as spiking and synaptic plasticity.[6–8]

Although NDR remains an old physical phenomenon, it has significant implications in cutting-edge research domains at the nanoscale, including quantum computation, reversible logic, and neuromorphic computing.[9] Therefore, it is crucial to investigate the origin of the negative differential resistance phenomenon and develop reliable negative resistance devices that are common in nanoscale devices for high-frequency applications or new computing architectures, such as reversible computation,[10] quantum computation,[11] and neuromorphic computing.[12] In this review paper, we comprehensively investigate the history and proposed mechanisms of NDR in Section 2, followed by an introduction to niobium oxide memristors in Section 3, which typically exhibit NDR behaviour. Finally, Section 4 discusses recent advancements in the application of NDR in niobium oxide memristors. This study seeks to provide important insights for researchers in this field by discussing the NDR effect and its applications in memristor devices.

2 Negative differential resistance

The static resistance of an electric device is defined as $R_s = V/I$, while the differential resistance is given by $R_{\text{diff}} = \mathrm{d}V/\mathrm{d}I$. Depending on their sign, which dictates the direction of current flow and the sign of electrical power, we can categorize various electronic devices with various functions. In particular, NDR devices have resistance of $R_s > 0$ and differential resistance of $R_{\text{diff}} < 0$.[9]

Negative differential resistance phenomena are commonly observed in certain diodes, such as tunnel diodes, and in some gases when they are discharged.[16–18] Meanwhile, chalcogenide glasses,[19] organic semiconductors,[20,21] and conductive polymers[22] exhibit similar negative resistance characteristics. In addition, reversible metal–insulator transition materials often exhibit NDR, with potential applications in memristors and neuromorphic computing.[9] There are two different current–voltage dependencies for NDR devices, as shown in Fig. 1 (red solid lines). The current-controlled S-shaped and voltage-controlled N-shaped dependencies refer to these types as negative conductors and negative resistors, respectively. The S-type NDR is termed the controlled-current NDR because a single voltage value can be associated with multiple current values. In contrast, for a voltage-controlled NDR exhibiting an N-shaped current–voltage relationship, a single current value

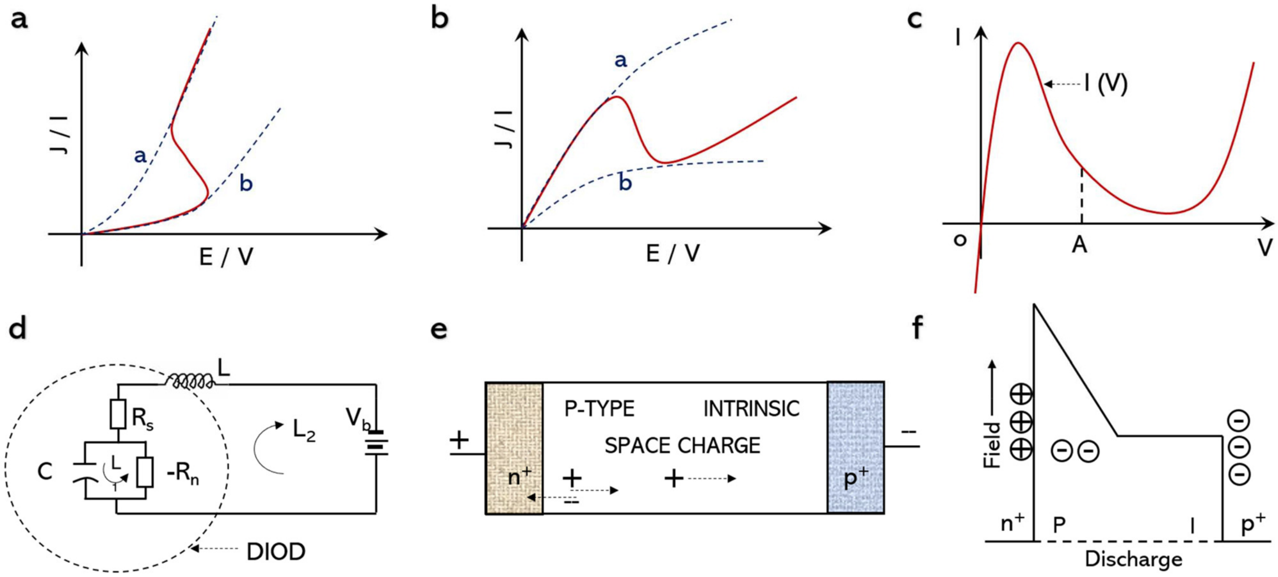

Fig. 1 Current–voltage dependence curves of (a) S-shaped and (b) N-shaped NDR devices.[9] The blue dashed lines show the field-induced transition that occurs between states a and b.[13] (c) *I*–*V* characteristics of the Esaki diode. (d) A simple equivalent circuit of an Esaki diode connected to a battery.[14] (e) Structure of IMPATT. (f) Fixed charge and field distributions in various regions.[15]

corresponds to multiple voltage values. Interestingly, as shown in Fig. 1, the appearance of the negative differential resistance region can be attributed to the occurrence of a transition between states a and b (blue dashed lines), triggered by an external field.[9] The exact mechanism for the generation of negative differential resistance[9,13] is explained in Subsection 2.2.

It is noteworthy that to accurately measure the NDR and obtain a stable NDR curve, certain conditions must be met by modifying the circuit structure and input signal.[23,24]

2.1 Early history of NDR

In the 19th century, during the exploration of electric arcs for illumination, the phenomenon of negative resistance was first observed although it was initially regarded by researchers as a secondary effect caused by temperature changes.[25] In 1895, Ayrton's experiments established the existence of a negative slope region in the curve and introduced the concept of differential resistance dV/dI because the resistance of passive devices cannot be negative.[25] In 1918, Hull *et al.* invented the world's first solid-state device with a negative resistance effect: Dynatron.[26] They found that changing the anode voltage did not change the value of the negative resistance. It only changes the range in which negative resistance occurs. In 1922, Lossev *et al.* built solid-state amplifiers and oscillators using the phenomenon of negative differential resistance found in a zinc oxide point contact junction.[27] However, with the success of vacuum tube technology, researchers have largely overlooked the potential applications of negative resistance devices.

In 1939, Terman *et al.* discussed the use of negative feedback to develop stabilized negative resistors that were essentially independent of tube and supply voltages.[28] Brunetti introduces an ideal negative resistance oscillator and a transition oscillator, and he further deduced that, with the fulfilment of a specific criterion: $-R_n = L/RC$, a negative resistance connected to a tuned circuit can function as a reliable energy source, ensuring that the tuned circuit remains in a consistent oscillation state.[29] Hahn introduced a streamlined approach to examining vacuum tube functionality at extremely high frequencies, disentangling the impacts of electron speed, conduction current, and induced current. If the grid is operated at an angle of $\pi/2$, then the grid impedance becomes a negative resistance. This theory has led to the development of various new tubes.[30]

In 1940, Tuttle *et al.* pointed out that transfer impedance exhibits unique characteristics, such as negative resistance, which is unattainable in conventional impedance. In a series resonant circuit incorporating negative resistance, there exists a resonant frequency point where the transfer impedance manifests purely as a negative resistance.[31] In 1953, Ryder *et al.* demonstrated an interesting fall in the mobility of electrons in Ge with an increasing electrical field.[32] Kromer was the pioneer who first proposed the concept of an NDR mechanism in 1953. Originating from observations of the degraded valence band structure in Ge and similar semiconductors, NDR theory emerged, suggesting that under a large electric field, holes are propelled into regions where their effective mass becomes negative. Additionally, it was anticipated that above a critical field threshold, the differential mobility of these holes would shift to a negative value. Nevertheless, subsequent investigations revealed that the quantity of holes occupying these negative-mass states was conspicuously insufficient, thereby maintaining a consistently positive differential mobility, despite the initial theoretical projections.[33,34] Kromer was later awarded the Nobel Prize in Physics in 2000 for the development of semiconductor hetero-structures applied to high-speed optoelectronic components.

In 1954, Shockley *et al.* explored the negative resistance in semiconductor diodes caused by transmission time. Shockley pointed out that negative resistance occurs if

$$\int_0^\infty D(t)\cos\omega t\,dt < 0. \tag{2.1.1}$$

The impulsive impedance $D(t)$ for a two-terminal device is characterized by its transient reaction to an impulse of current.[35] Bratton, alongside John Bardeen and William Shockley, co-invented the world's first transistor, known as the point-contact semiconductor amplifier, and their groundbreaking work on transistors and the discovery of the transistor effect later earned them the 1956 Nobel Prize in Physics.

In August 1958, Leo Esaki invented a tunnel diode (also known as an Esaki diode). The Esaki diode was the first quantum-electron device. Contrary to the mechanisms that govern most semiconductor devices, the current flow in an Esaki diode is facilitated by quantum-mechanical electron tunnelling across a potential barrier.[36] This diode exhibits an effective "negative resistance" stemming from the quantum-mechanical phenomenon known as tunnelling. Tunnel diodes possess a heavily doped p–n junction, approximately 10 nm wide, where heavy doping leads to a disrupted band gap, aligning the conduction band electron states on the N-side with the valence band hole states on the P-side to a certain extent. A typical I–V characteristic of an Esaki diode is illustrated in Fig. 1(c). In mixer applications, the section of the 'forward' bias range marked as O–A on the voltage axis, encompassing the area of negative gradient, holds significant importance. Fig. 1(d) shows a simple equivalent circuit of an Esaki diode connected to a battery.[14,37] In 1973, Esaki was awarded the Nobel Prize in Physics for his discovery of the quantum tunnelling effect of electrons in semiconductors.

Additionally, in 1958, Read proposed the avalanche diode, alternatively known as the Impact Ionization Avalanche Transit-Time Diode (IMPATT), which is a unique diode variety intended for operation in the field of reverse or avalanche breakdown. The structure of IMPATT is shown in Fig. 1(e). Unlike conventional PN junction diodes, which are prone to excessive current concentration and subsequent hot spots that can lead to irreversible damage, the IMPATT diode's junction is engineered to mitigate such concentration and hot spots. This design ensures that the IMPATT diode remains unaffected in the avalanche breakdown region. It comprises a high-field avalanche zone and a drift region, which, at microwave frequencies, generates dynamic negative resistance. This negative resistance trait emerges owing to a temporal lag, resulting in a phase shift between the components of AC and voltage, a distinct phenomenon in contrast to tunnelling diodes. As depicted in Fig. 1(f), the depiction of the field distribution and stationary charges across the various regions under reverse bias is presented. Notably, the applied voltage consistently surpasses the punch-through threshold, which ensures that the space-charge region spans from the n^+–p junction, traversing through the p and intrinsic (i) regions to the i–p^+ junction.[15]

In 1961, Ridley investigated the potential applications of negative resistance effects in semiconductors. The methodology lies in heating carriers within a high-mobility sub-band using an electric field, triggering their transition to a higher-energy, low-mobility sub-band once they attain a sufficient temperature. The prerequisites for achieving negative resistance are broadly examined, and by solving the Boltzmann equation, more tailored conditions are derived for simplified scenarios involving spherical and ellipsoidal bands. Their analysis reveals that the most favorable scenario arises when the sub-bands are sufficiently energy-separated, enabling optical phonon emission to become the primary mechanism for energy relaxation in both sub-bands.[38]

In 1962, Hickmott found negative resistance and a large current density in the DC-voltage characteristics of five metal–oxide–metal structures. Hickmott found that the breakdown of oxide films, in the sense of a sharp increase in current, produces irreversible and permanent changes in the aluminum oxide film; the original high resistivity and the exponential dependence of the current on voltage cannot be recovered. However, the breakdown leading to an increase in conductivity and negative resistance of the oxide film can be distinguished from dielectric breakdown, which destroys the insulating film. The term 'formation' in the oxide film implies the establishment of a negative resistance region in the *I–V* curves by non-destructive breakdown of the film. During the formation process, the maximum current through the oxide film increases as the voltage applied to the oxide film increases.[39]

In 1963, Gunn discovered the Gunn effect.[40] Microwave oscillations are induced when a constant DC voltage, exceeding a critical threshold, is applied to the opposing surface of an N-type GaA contact electrode. By establishing ohmic contact electrodes at both ends of the N-type gallium arsenide sheet, the electric field generated by the DC voltage can surpass 3 kV cm^{-1}. Owing to the unique properties of GaAs, this leads to the generation of current oscillations, with frequencies reaching up to 10^9 Hz.[40] Devices with Gunn oscillations are known as Gunn diodes, serving as generators of microwave signals.

In 1966, Copeland put forward a novel operational framework for bulk negative resistance oscillators. During Limited Space-charge Accumulation (LSA) oscillation, the electric field across the diode undergoes a rapid increase, surpassing the threshold value and reaching a level more than twice the value of the threshold field. The high-field domain lacks sufficient time to establish its characteristic space charge distribution. Consequently, an accumulation layer is predominantly observed near the source contact, while the electric field over the majority of the device remains in the negative resistance domain.[41]

In 1969, Berglund constructed an idealized layered structure of vanadium dioxide (VO_2), demonstrating that under certain voltage bias conditions, a high temperature and low resistance filament can be generated in the VO_2 film. The location where the filaments form is related to the positions of the external heating and excitation sources (applied voltage), and it gradually moves to the point closest to the electrode spacing. The width of the filament depends on the applied current, and under the influence of time-varying electrical excitation, the conductive filament exhibits characteristics similar to those of an inductor.[42] Subsequently, in 1970, Berglund used VO_2 to create a type of thin-film inductor. He determined the variation in the conductivity of the VO_2 thin film with temperature through mathematical derivation and experimental verification. Based on the relationship between conductivity and temperature, the current–voltage relationship showed a clear negative differential resistance behavior, and Berglund also verified this in subsequent experiments. This is because the VO_2 films exhibited rather significant thermal hysteresis and latent heat effects during the crystal phase transition process.[43] In 1971, Berglund discussed the role of thermal effects in the process of resistance switching in solid films. It was shown that thermally initiated events complete the switching by thermal processes. Electronically initiated events complete the switching either by an electronic or by a thermal mechanism. Under high voltage conditions, the effect of thermal energy becomes more pronounced. When there is a voltage collapse, electrostatic energy is released, and the temperature rises rapidly at a rate proportional to the square of the switching field, determining whether the device switches or breaks down.[44]

In 1972, Tellegen introduced three assumptions about the NDR effect.

Assumption 1: The impedance behavior of the negative resistance is mathematically described by

$$Z = \frac{(a+bs)}{(c+ds)}, \tag{2.1.2}$$

where the ratios of the coefficients are contingent upon the specific point on the direct current (DC) characteristic curve that *Z* pertains to.

Assumption 2: At points on the DC characteristic curve situated far from the region of the negative slope, the impedance function exhibits a positive characteristic.

Assumption 3: As the point traverses the DC characteristic curve, a pole (or zero) of the impedance function migrates from the left to the right half of the *s*-plane, or conversely, precisely when the slope of the voltage-current characteristic changes its sign by traversing an infinite [or zero] point, and at that instant, the pole (or zero) traverses the $s = 0$ point.[45]

In early studies of negative differential resistance, researchers discovered the existence of the negative differential resistance effect in a vacuum tube, but there was no understanding of its mechanism and properties. For example, Terman, Brunetti, and Hann *et al.* performed a preliminary exploration of negative differential resistance in vacuum tubes. They obtained some methods and empirical formulas to regulate negative differential resistance. However, they did not go deeper into the substantive reasons for the negative differential resistance. Subsequent to the invention of the diode and the increase in the semiconductor industry, researchers began to discover the negative differential resistance effect in semiconductor materials and applied it to high-frequency oscillators, high-speed switches, and power amplifiers. Examples include the Esaki diode, Gunn diode and the IMPATT diode. They innovatively applied the negative differential resistance in transistors to oscillate signals or amplify them. The transistors they prepared played an important role in the development of electronics. However, owing to the limitations of time and technology, early researchers were unable to conduct an exhaustive study of negative differential resistance. Later, Kromer, Shockley, Ridley and others conducted in-depth studies on the mechanism of negative differential resistance and gained a deeper understanding of the physical nature of negative differentials. Subsequently, the advent of advanced instrumentation has further advanced the study of negative differential resistance. Presently, it is evident that the field of memristors has become a major area of research interest, thus bringing negative differential resistors to the attention of the general public once again. The negative differential resistance effect exists in many materials and is generated by various mechanisms. In the future, the study of the negative differential resistance effect will be further emphasized, and the negative differential resistance in some materials will be further applied, as in the case of materials with a negative differential resistance effect used for the preparation of transistors.

Based on the above discussion, we summarized a timeline of the key research reports on the NDR effect, as shown in Fig. 2. It should be noted that extensive studies on negative differential resistance have been conducted over time and have continued to grow, with numerous researchers dedicated to the field. In the history of NDR research, there are still many significant studies, such as the research conducted by Simmons and Verderber in 1967,[46] and Mott's research in 1968.[47] This study provides only a brief, one-sided introduction. Since the 1980s, most studies on NDR have primarily focused on applications and refining previously proposed mechanisms. A more comprehensive review of recent NDR studies can be found in ref. 9.

2.2 Mainstream perspectives on the NDR effect generation mechanism

In this subsection, we review the mechanisms that generate NDRs, including scattering-induced, electron-transfer, and percolation-induced mechanisms. A more detailed discussion can be found in the studies by Ridley,[13] Dearnaley[48] and others.[9,49,50]

2.2.1 Scattering-induced NDR. Under certain conditions, NDR may occur owing to multiple scattering events, which comprise four main types of scattering. First, the electron–electron scattering process is considered. Electron–electron scattering suppresses spin relaxation and indirectly stabilizes

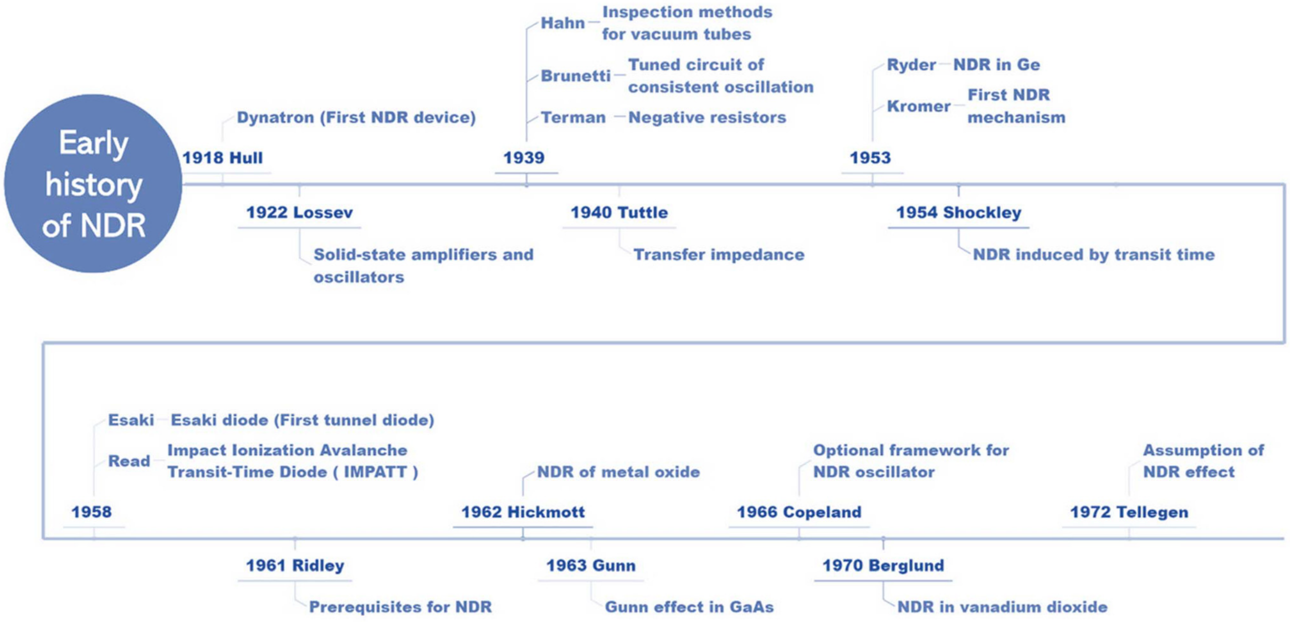

Fig. 2 Timeline of the key research reports on NDR before the 1980s.

carrier transport paths, thus contributing to NDR at specific biases.[51,52] Second, the interaction between polar longitudinal optical (LO) phonon scattering and acoustic phonon scattering in a parabolic band may yield the NDR phenomenon.[13] Third, when the magnetic field exceeds a critical threshold, polar LO phonon scattering is unable to sustain energy equilibrium. This results in a transition towards deformation-potential scattering through acoustic modes. When the relative strengths of polar and deformation-potential coupling fall within specific boundaries, the transfer from dominant LO phonon scattering to acoustic-phonon scattering can lead to an NDR outcome.[13,53] Fourth, when the temperature rises, electrons gain sufficient energy to transition to a higher energy state. The Fermi level μ approaches the valence band bottom, and the electron distribution in the conduction band is dominated by Boltzmann statistics. Consequently, the suppression of the NDR effect at high temperatures is mainly due to electron–phonon scattering.[54] More fundamentally, inelastic scattering enhances the effect of temperature on the tunnel effect.[55] Overall, multiple scattering mechanisms can trigger NDR in a synergistic manner, with a shift of different scattering mechanisms.

2.2.2 Non-parabolicity. Thermal electron effects in semiconductor devices affect the stability of the devices, and these thermal electron effects are usually related to scattering and acceleration processes at extremely high energies, thus being influenced by the characteristics of the band structure. This can alter the potential energy distribution of electrons through a non-parabolic linear variation of energy momentum, thereby influencing their motion trajectories and scattering frequencies. In non-polar semiconductors, the drift velocity of electrons is expected to saturate in a parabolic band owing to optical-phonon emission. This saturation leads to a reduction in the field when the band is non-parabolic, resulting in an NDR.[13] The dispersion relationship derived by the model is generally non-parabolic and linear. In general, we can deal with non-parabolic properties by defining an energy function.[56] When non-parabolicity is fully considered in numerical simulation, NDR is less sensitive to changes in thermal conductivity. From an experimental perspective, non-parabolic linearity is important in the hydrodynamic transport model (HTM).[57] The NDR phenomenon may also arise in scenarios involving polar LO phonon scattering, where even a modest level of non-parabolicity can prevent runaway effects at the expense of NDR instability.[13,58]

2.2.3 Electron-transfer. The mechanism represents the migration of electrons from a valley with a light effective mass to one with a heavy effective mass, driven by elevated temperatures.[13] One straightforward method to achieve this involves using electric field heating to transition electrons from high mobility sub-bands to high energy sub-bands with lower mobility.[38] In some nanoscale molecular devices, NDR properties are caused by electron transport involving discrete states in the electronic structure.[59–61] In certain semiconductors, such as GaAs, the electrons have a high-mass low velocity state as well as their normal low-mass high-velocity state. The movement of electrons between these two states results in the generation of a pulsed current. A Gunn diode is built from this electron transfer mechanism and the negative mass mechanism.[40] Other nonlinear electron transportations, such as Poole–Frenkel (PF) emissions, are also an important cause of NDR.[62]

2.2.4 Negative mass. Spatial undulations occur when subjected to the propulsive force of a direct current (DC) electric field. This remarkable behavior, termed Bloch oscillations, arises inherently from the quantum nature of electrons and their innate responsiveness to accelerating DC fields, demonstrating oscillatory motions.[63,64] The origins of Bloch oscillations can be traced to the phenomenon of Bragg reflections and are intimately tied to energy domains within the conduction band, where electrons assume a unique state characterized by a negative effective mass.[65] These peculiar regions of negative mass are encountered in specific crystallographic alignments near the zone center within the heavy-hole band. Within GaN, negative mass NDR can be attained by leveraging conduction band structures and accelerating electrons ballistically under exceedingly high electric fields.[66] However, it should also be noted that when electrons are transferred into the energy valley on a large scale, negative mass NDR is replaced by electron transfer NDR.[67] The precise value of the negative effective mass depends on the electron density and scattering time.[68] Theoretically, if a substantial concentration of holes could be coaxed to populate these states under intense electric fields, this could lead to the achievement of intriguing electronic behaviors, such as an NDR effect. However, the prevalent scattering mechanisms in practical settings pose significant challenges to utilizing Bloch oscillations to achieve NDR-like functionalities, making this endeavor notably challenging.[13]

2.2.5 Optically induced NDR. Monochromatic light induces the optical stimulation of electrons from a well-defined energy level (often impurity-mediated) into a precisely matched series of levels within the conduction band. This process can yield a quasi-delta function distribution in the electron energy spectrum, constrained by resonance between the initial and final states. This distribution is the premise of the optically induced NDR. This process necessitates that the recapture of electrons occurs at a rate significantly faster than scattering processes.[13] The scattering process is related to the density and mobility of the photogenerated carriers. By affecting the carriers, the scattering process can be influenced, which further affects the distribution function and leads to NDR. For example, the density and mobility of the photo-generated carrier are decreased by applying a bias[69,70] or by the capture and release of charge.[71,72] Light exposure causes the injection barrier to be lower, and the trapped electrons effectively pass through the barrier between the source and the channel.[72] In addition, optical-induced NDR may result from gate-dependent surface recombination and potential well-induced photocarrier confinement.[73] If the energy level of the excited electron is slightly below the energy threshold of the emission of the optical phonon, negative resistance may result. For example, in the graphene structure, optically induced NDR is mainly affected by the resonant tunneling of charge carriers through minibands.[74] In GaAs, the photogenerated charges accumulate in the double barrier quantum well (DBQW) region, causing built-in electric field modulation, which in turn leads to NDR.[75] However, in practice, the rate of electron capture is typically much slower than scattering, resulting in a distribution function that deviates significantly from the desired form. Therefore, it is difficult to obtain a stable NDR effect using this method. In theory, the use of two strong laser beams can produce a suitable distribution function, but again, it leads to instability of the NDR.[13]

2.2.6 Magnetically induced NDR. In a situation where a strong magnetic field quantizes the system, confining all electrons to the lowest Landau level, electronic transport is mediated by scattering events between spatially distinct magnetic states. An essential aspect here is that the scattering rate is directly linked to the availability of final states. In this quasi-one-dimensional (quasi-1D) system, the density of the states diminished as the energy rose. Consequently, in the presence of an electric field, a single charge carrier tends to propagate towards regions of higher potential.[13] The magnetic tunnel feature is explained by the arrangement of the quantized 2D Landau levels in the trap and emitter deposits. According to the principle of conservation of transverse momentum, this mechanism should produce a sharp NDR effect in the tunneling regime.[76,77] NDR-capable semiconductor can be integrated with magnetic materials exhibiting the anomalous Hall effect to create three-terminal magnetic devices. The interaction of the two effects results in devices with excellent thermal stability.[78]

2.2.7 Percolation NDR. In semi-insulating materials, the occurrence of significant potential variations, often stemming from impurity clustering, can significantly hinder transport mechanisms, confining them to few percolation pathways.[79,80] At elevated electric fields, it is anticipated that the increased energy of charge carriers will facilitate the expansion of existing percolation paths or create a new one. In a memristor, conductive percolating networks form similarly to conductive filaments. Percolating conductive atoms or oxygen vacancies increases the conductive phase of the memristor, thus changing the device from an insulating state to a conductive state.[81] However, there also exists the possibility that a greater number of carriers may be energized into non-conductive zones, where they become effectively trapped and immobilized. If this latter phenomenon prevails, it can lead to a notable reduction in overall conductivity, potentially demonstrating an NDR effect.[13] Percolation also appears as recombination between similar substances. The composite material, composed of carbon black nanoparticles, graphene and graphite, effectively acts as a percolation network in which transport is carried from one nanoparticle to the next *via* a tunnel-assisted transition. The composites oscillate in the NDR region at frequencies exceeding 10 kHz. Besides, in highly oriented pyrolytic graphite (HOPG), low-temperature NDR is derived from percolation transport through HOPG nodes with anisotropic conductivity.[50] Owing to the high mobility and saturation rate of graphene, the NDR effect in graphite is higher than that in silicon. Thus, through the Dirac point splitting effect induced by drain bias, an inverter with two identical devices can be provided.[82]

2.2.8 Two-level impurity NDR. Various mechanisms for a current-modulated NDR effect encompass the interaction of impurities through impact ionization. One scenario involves an impurity center that possesses both a ground state and an excited state. The impurity barrier effect stems from the entrapment of impurities around the barrier. Carriers are easily trapped by impurities; thus, electrons at the impurity location cannot be thermally ionized to the conduction band. However, trapped electrons can be ionized to the conduction band by accelerated free electrons (called shock ionization) driven by an external electric field. Thus, free carriers can be trapped by ionized impurity sites or released by the shock ionization of trapped electrons.[83] For example, when silver is employed as an electrode, silver ion diffusion may occur, resulting in the formation of impurity bands at the charge transport level and deeper charge capture levels.[84] This mechanism operates by the cumulative effects of impact ionization into the excited state and impacts excitation from the ground state to the excited state. These processes enhance the occupancy of the excited state at the cost of depopulating the ground state. Since the excited state exhibits a higher propensity for subsequent impact ionization compared to the ground state, a reduced electric field is required to sustain a given current flow. This behavior aligns with the characteristic S-shaped NDR pattern.

2.2.9 Double injection. In a high conductivity state, the carrier concentration increases from the thermal equilibrium value owing to the simultaneous injection and neutralization of holes and electrons. Deep impurities can no longer trap them, and the substrate region becomes highly conductive. Current-modulated NDRs may manifest when such a semiconductor exhibits semi-insulating characteristics.[85] This condition is feasible when a recombination center is fully occupied by electrons in its equilibrium state. The underlying cause of the NDR in this instance stems from a transition from an effective single-carrier injection mechanism to a double-carrier injection process. In some cases, this transition can be achieved by heating[86] and applying voltage.[87] This transition can also occur when the injection of one carrier type is impeded until the electric field at the blocking contact reaches a threshold level sufficient to either initiate tunneling or trigger impact ionization near the contact, thereby enabling the flow of both carrier types. Consequently, the I/V characteristic abruptly shifts from a single-carrier to a dual-carrier trajectory, resulting in a current-controlled NDR effect.[13] In some cases, fluctuations in the minority carrier supply can lead to a double NDR behavior on the inner electrode. If the double NDR is to be tuned, the minority carrier supply can be varied by changing the bias conditions.[88]

2.2.10 Transit-time NDR. The mechanisms for negative differential resistance (NDR) previously elaborated upon function under direct current (DC) conditions. However, there exists a class of devices, notably the IMPATT (impact ionization avalanche transit time) diode and Gunn diode,[40,89] which exhibit NDR phenomena at microwave frequencies, serving as potent solid-state sources of microwave radiation.[90–92] These devices were based on Read's 1958 diode concept,[15] which evolved from Shockley's earlier explorations of transit-time devices in 1954.[35] Essentially, the IMPATT diode incorporates a high-field zone where injected charge carriers trigger an avalanche multiplication process *via* impact ionization. This is followed by a low-doped drift region, where the generated electrons, owing to the intense field, propagate at their saturation drift velocity. Two critical phase delays are integral to its operation: the first is related to the injection of carriers into the drift space, while the second is linked to the transit time through this region. Transit time effects dominate the intrinsic negative resistance of a quantum well-biased NDR.[93] By carefully designing these phase delays, it becomes feasible to engineer the device such that the real component of its impedance becomes negative, enabling unique microwave frequency operations.

2.2.11 Phase transformation-induced NDR. Phase transformation is a prevalent phenomenon in materials, and in the future, it may broaden the limited class of materials that showcasing NDR. Harumoto *et al.* demonstrated the first experimental demonstration of NDR induced by metal-to-metal-hydride phase transformation in the literature.[94,95] When metal hydrogenation begins, a solid solution is formed owing to the slight incorporation of hydrogen atoms into the metal lattice. However, the metal's crystal structure is retained at this stage, resulting in a low resistance state. Further, an increase in hydrogen gas pressure deforms the initial metal state, and a new phase with a different crystal structure of metal and hydrogen is formed, exhibiting a relatively higher resistance state. This resistance state change is advantageous for fabricating hydrogen gas storage devices.[96,97]

When metal is heated, it can undergo three mechanisms: first, an increase in resistance due to increased phonon scattering; second, decreased resistance resulting from the slight hydrogen escape from the metal-hydride lattice; and third, resistance decrease owing to metal-hydride-to-metal phase transformation. The third mechanism significantly and abruptly impacts resistance compared to the other two mechanisms. However, it occurs only at the phase transformation temperature, where the change in the crystal structure abruptly results in a decrease in the hydrogen concentration. This sudden decrease in resistance induces an NDR property. The resistance *vs.* temperature response is a sum of these three impacts. When heat sufficient for the phase change is supplied, the impact of phase transformation may exceed the phonon scattering effect, inducing NDR.[94]

Overall, the research and exploration of the origin of NDR continues to develop, but we are unable to introduce all other NDR mechanisms, such as the hot phonon negative differential resistance effect,[98] blocked carrier injection,[99] and the impurity barrier effect,[82] in a comprehensive and detailed manner in this review paper.

The following table provides a brief overview of representative materials with negative differential resistance. Furthermore, the relevant references listed in the table are not representative documents of this material in the field, but rather documents that consider both the application of the material and the NDR mechanism (Table 1).

It has been demonstrated that N-type NDR is linked to the creation of high-field domains. Typically, the high-field domain forms between two low-field domains, which are positioned perpendicular to the current direction on the surface.[104] For example, in the superlattices composed of the graphene/h-BN, when subjected to an electric field, the discrete energy levels specific to quantum wells undergo delocalization, resulting in extended minibands. Within these minibands, carriers undergo spatial confinement owing to repetitive Bragg reflections, leading to the emergence of quantized Stark ladders. This field-driven oscillatory motion of carriers constitutes Bloch oscillations, which inherently generate a negative differential resistance (NDR) signature in the current–voltage characteristics.[9] For an explanation of the principles of negative mass, please refer to Subsubsection 2.2.4.

Moreover, n-type NDR materials have been widely applied on a large scale. For instance, GaN is used in light-emitting diodes and high-frequency stage microwave communication (specifically, it is applied in RF power amplifiers in 5G communication systems). However, the S-type NDR devices are currently still in the experimental stage and face issues such as performance stability and integrated manufacturing. In S-type

Table 1 Representative materials with negative differential resistance

Materials	NDR type	Mechanism	Application	Ref.
NbO_2	S-type	NDR-1: PF effect NDR-2: Mott-MIT	Sensor Image recognition task	100
VO_2	S-type	Mott-MIT	Image recognition task	101
CoFeB	S-type	Magnetically induced	Boolean logic operations	78
TiO_2	N-type	Redox; ion migration	Computing-storage integrated chip	102
GaAs	N-type	Gunn effect	Oscillatory neurons	75
GaN	N-type	Negative mass	Diode oscillator	92
Graphene/h-boron nitride	N-type	Resonant tunneling	Flexible oscillators	50
Doped silicon	N-type	Double injection		88
SiC	N-type	Transit time	IMPATT diode	103
Silver-electrode memristor	N-type	Two-level impurity	Multilevel memory devices	84

NDR devices, NbO_2 exhibits a higher Mott temperature than VO_2, making them less susceptible to external temperature fluctuations. Compared to TiO_2, NbO_2 can achieve a lower operating voltage and a faster switching speed. NbO_2 is currently one of the few materials that possess both current-controlled PF-NDR and temperature-controlled Mott-NDR dual mechanisms. Its wide temperature range, stability and dual-mode control capabilities are irreplaceable in neuromorphic computing and extreme environment electronics. Therefore, NbO_2 is expected to become an S-type NDR material for large-scale applications. In the subsequent sections, we briefly reviewed recently reported negative differential resistance phenomena in niobium oxide memristors.

3. Brief overview of niobium oxide memristors

3.1 Brief description of the memristor

As shown in the relationship between the basic circuit elements and their variables depicted in Fig. 3(a), Chua found that there is a lack of an unknown device between magnetic flux and electric charge and therefore proposed a concept of memory resistor, memristance (M).[105] M follows the law of $V = MI$, which is similar to the mathematical representation of the resistor, but the value of M depends on the total amount of charge that has flowed through the device in the past, which is similar to the function of having a memory.[106] Therefore, the name of the memory resistor (memristor) was proposed, and the four basic two-terminal circuit components are resistance, capacitance, inductance and memristor, as shown in Fig. 3(a). It is noteworthy that in 1976, Chua and Kang expanded the concept of the memristor to a memristor system, where the value of magnetic flux is no longer solely determined by the charge. This means that the value of M can no longer be simply defined as $M = \mathrm{d}q/\mathrm{d}\varphi$.[107] After that, memristors were usually referred to as generalized memristors, that is, memristor systems.

Memristors can be classified into analog and digital memristors based on whether the electrical conductivity undergoes a sudden change. Based on its abrupt current change characteristics, a digital memristor possesses discrete resistance states, typically representing binary values (0 or 1), and can therefore be integrated into chips used for signal sensing and neural network computing.[108,109] It switches between these states in a digital manner akin to conventional digital memory elements like flip-flops. Analog memristors, unlike their digital counterparts, display a gradual change in resistance values in response to varying currents. This characteristic enables them to demonstrate a wide range of resistance states, facilitating the storage and processing of information in a manner that closely resembles the continuous nature of real-world signals. These features make analog memristors well-suited for applications, such as neuromorphic computing, where they can replicate the behavior of biological synapses, thereby supporting the creation of efficient and brain-inspired computational systems.[110]

Moreover, memristors can be categorized into non-volatile memristors and volatile memristors based on their ability to maintain data, *i.e.*, whether the resistance state is maintained after a power failure. Volatile memristors necessitate a continuous power supply to sustain the state, leading to data loss following a power failure, suitable for dynamic computing scenarios (*e.g.* synaptic simulation for neuromorphic computing).[111] In contrast, non-volatile memristors can preserve stored data even in the absence of a power source. Various non-volatile memristor units have been employed for synaptic storage and on-chip neurosynaptic computation and embodied into the basic framework for neural networks after the integration of a memristor, enabling *in situ* synaptic plasticity, on-chip programming and on-chip learning by applying voltage pulses. This approach allows for the construction of dense, large-scale neuromorphic processors with in-memory computational capabilities.[112]

In 2008, researchers at Hewlett-Packard Labs prepared the first nanoscale Pt/TiO_2/Pt memristor and validated its resis-

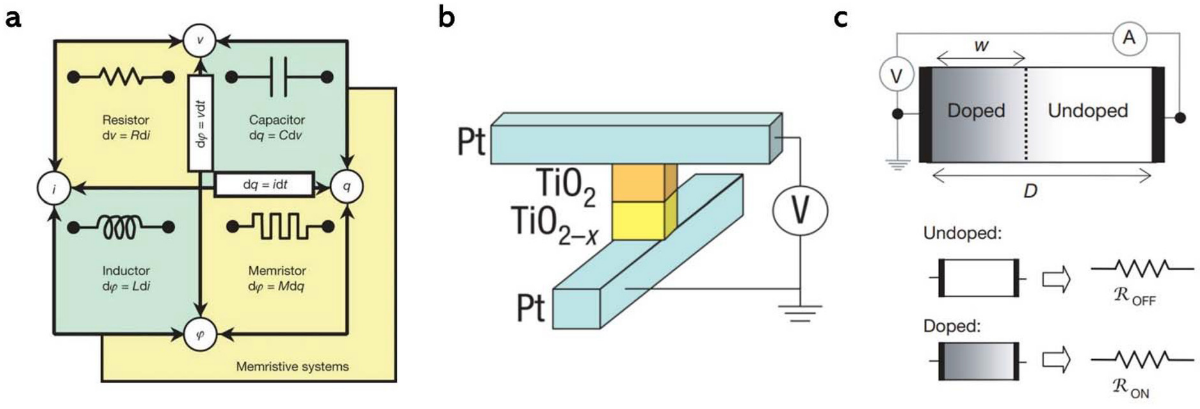

Fig. 3 (a) Relationship between basic passive circuit elements and basic circuit variables. (b) Fabric of Pt/TiO_2/Pt memristor. (c) Conception of the resistive switching principle.[108]

tance modulation capability (Fig. 3(b) and (c)).[108] The researchers believe that the resistance change in this device is caused by the migration of oxygen vacancies under the influence of an electric field, which leads to a change in the thickness of the insulating TiO_2 and low resistance TiO_{2-x} layers. These two layers are similar to the series connections of the two variable resistors. In this system, oxygen vacancies act as mobile positively charged dopants. They proposed two equations to explain their conjecture:

$$v(t) = \left[R_{\mathrm{ON}}\frac{w(t)}{D} + R_{\mathrm{OFF}}\left(1 - \frac{w(t)}{D}\right)\right]i(t), \tag{3.1.1}$$

$$M(q) = R_{\mathrm{OFF}}\left(1 - \frac{\mu_{\mathrm{V}}R_{\mathrm{ON}}}{D^2}q(t)\right), \tag{3.1.2}$$

where R_{ON} is the resistance value of the low-resistance state, R_{OFF} is the resistance value of the high-resistance state, D is the thickness of the device, and $w(t)$ represents the state variable of the device, which is the length of the doped segment containing oxygen vacancies, and is defined as follows:

$$w(t) = \mu_{\mathrm{V}}\frac{R_{\mathrm{ON}}}{D}q(t), \tag{3.1.3}$$

where μ_{V} is the average ion mobility and $q(t)$ represents the electric charge as a function of time.

When the R_{OFF} is significantly greater than R_{ON}, the part in parentheses in eqn (3.1.1), which represents the memristance, can be expressed as (3.1.2).[108] Pickett *et al.* conducted electrical characterization and state-evolution procedures on the memristor of this structure, experimentally verifying the viewpoint of Hewlett-Packard Labs that during the electroforming process, a localized conducting channel is formed, which almost connects the upper and lower electrodes, leaving only a very narrow insulating gap. Moreover, they put forward an important conclusion regarding memristors: the energy required to switch a metal–oxide device decreases exponentially with increasing applied current.[113] Similarly, such conductive channels were also observed in the niobium oxide memristor, namely a complete crystalline NbO_2 channel.[7,114] The specific details in this regard are elaborated in Subsubsubsection 4.2.1.1.

Despite recent advances in brain-inspired computing systems based on traditional CMOS technology, significant challenges remain in terms of integration and power consumption.[115] Memristors, which exhibit continuously adjustable resistance under an applied electric field, represent an ideal neurosynaptic component. They offer a promising avenue for developing high-density, low-power brain-inspired computing chips. Moreover, memristor arrays can facilitate the construction of more integrated neural network structures, including artificial neural networks (ANNs),[116] convolutional neural networks (CNNs),[117] deep neural networks (DNNs),[118] recurrent neural networks (RNNs),[119,120] and spike neural networks (SNNs).[121] The memristor arrays employ Ohm's law for addition and Kirchhoff's law for multiplication, thereby facilitating parallel multiplication-accumulation (MAC) operations essential for neural networks, which remarkably enhances the speed and power efficiency of neural networks.[115,122,123] In digital memristors, resistance switching requires a resistive switching process with a threshold transition, which is how the resistive switching mechanism is categorized. Memristors can be classified into electrochemical metallization cells (ECM, also known as conductive bridge RAM, CBRAM), which are usually formed owing to the formation of conductive thin filaments, as well as oxidative valence mechanism memories (VCM, also known as metal–oxide resistive memories, OxRAM), which are usually formed based on the formation of oxygen vacancies, and thermochemical mechanism (TCM) devices.[4,124]

In numerous practical applications, the negative slope phenomenon often arises from a temporal discrepancy, or phase shift, existing between the voltage response waveform, denoted as $V(t)$, and its originating stimulus—the current waveform, labelled $I(t)$. This misalignment or phase difference visually represents the negative slope phenomenon of the NDR.[106] NDR stands out among other mechanisms because it uniquely combines dynamic, tunable switching with the potential for oscillatory behavior, which is particularly advantageous for neuromorphic computing. However, an ideal memristor cannot exhibit small-signal negative resistance unless it is locally active at the origin, a condition achieved only if the memristor possesses an internal power source, such as light, a chemical reaction, a nuclear reaction, or a battery.[106] S-type NDR in various electronic devices is not as common as N-type NDR, but it has long been encountered, such as in the insulator–metal transitions (IMTs) of various oxides (also known as Mott transitions). Recently, S-type NDR has regained significant attention in the context of memristor development and the expansion of its applications in neuromorphic circuits.[9]

3.2 Brief description of niobium oxide memristor

In addressing memristor functionalities, the challenge of leakage currents within resistive random-access memory (RRAM) arrays often leads to performance impairments, such as faulty read/write operations. Addressing this issue without compromising cell size necessitates innovative solutions. The unique current window exhibited by the niobium oxide memristor (especially NbO_2) can enhance the selectivity of the device, enabling its utilization as a memristor that can be serially integrated with nonvolatile memory. Additionally, the higher Mott insulator–metal transition temperature (1081 K) of NbO_2 compared to VO_2 (340 K) allows for a more practical operating range.[125] Therefore, niobium oxide memristors have now become promising oxide memristors that have attracted significant research interest.

With different circuit configurations, the niobium oxide memristor can be used as a selector and neuron, as shown in Fig. 4. It is noteworthy that different *I*–*V* characteristic curves occur for voltage and current scans, but the two curves correspond to the same "inflection points" (*i.e.*, the points where the resistance changes abruptly, which are often called the

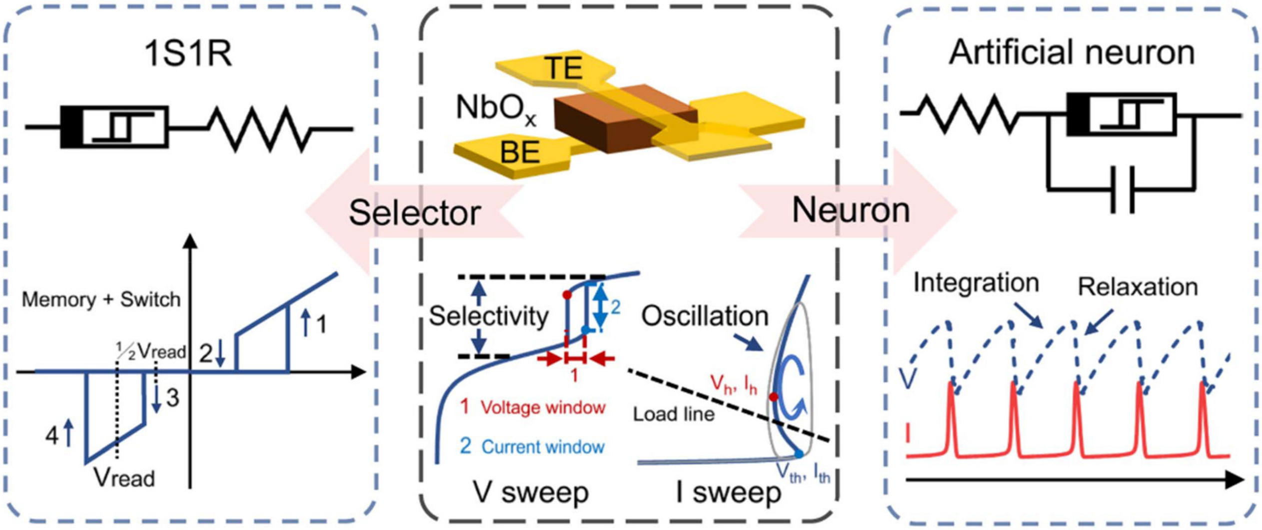

Fig. 4 Typical structure of a niobium oxide device: top electrode, niobium oxide functional layer, and bottom electrode. Threshold switching imagery under voltage scanning, and negative differential resistance effects under current scanning. Niobium oxide memristor is used as a selector or neuron by combining it with an electronic component, and the electrical characterization of both of them.[126]

threshold voltage V_{th} and the holding voltage V_{h}). These memristors can be integrated with memory cells, which maintain the compactness of the RRAM device, thereby fulfilling both integration and operational criteria without increasing the overall footprint.[126] The NbO_2 memristors demonstrate a reversible transition from an insulating state to a metallic state triggered by the current flow, generating ample thermal energy.[127] Specifically, the NbO_x-based memristor represents a nanometer-scale element that exhibits distinct S-shaped NDR behavior. This unique device can function as a selector within a crossbar architecture comprising memristors, facilitating both reading and writing functions in non-volatile memory arrays. In 2012, researchers proposed a scalable neuristor built with NbO_2 Mott memristors. The device constitutes a neuroresistive element crafted from a duo of nano-scale Mott memory resistors, known as Mott memristors. These novel devices exhibit remarkable dynamic properties, exhibiting fleeting memory capabilities alongside NDR phenomena during a phase transition from an insulating state to a conducting one, induced by the energetic process of Joule heating. It is well established that Mott insulators, such as NbO_2, exhibit current-controlled NDR, commonly referred to as threshold switching, when employed in two-terminal devices.[128] This neuristor leverages advanced materials and intricate structures that are compatible with ultra-dense integration strategies, either in conjunction with silicon transistors or independently, to achieve pivotal neural functionalities. These functionalities include the generation of binary-like spike pulses, characterized by an all-or-nothing response with signal amplification, as well as the production of periodic spike patterns across two interconnected nodes, which represents a significant advancement in mimicking and enhancing the operational mechanisms observed in biological neural networks.[128] Subsequent research on neuronal circuits for niobium oxide memristors has developed rapidly.

4. NDR effect on niobium oxide memristor

NDR behavior in oxide memristors, especially those using NbO_2, has attracted renewed interest owing to its potential applications in neuromorphic computing.[100] The presence of negative differential resistance, or the transition of resistance between high and low resistance states, gives devices, such as niobium oxide[129,130] and vanadium oxide,[131–133] the potential to build neuronal pulse circuits.[115,134]

4.1 Early research

In some of the early studies of niobium oxide NDR, although the concept of memristors was not yet available or had little connection with memristors, there have been preliminary studies of oscillatory circuits, periodic pulses, threshold voltage, switching delay time, residual on-state voltage and other important characteristics of memristors.

In 1963, Geppert *et al.* discovered a room-temperature negative resistance in niobium–niobium oxide. Circuits were employed to assess the oscillation abilities of the device. Sustainable sine-wave oscillations were easily generated, reaching up to approximately 6 MHz, which is the maximum frequency they attempted. Additionally, parasitic oscillations at around 100 MHz were frequently observed.[135]

In 1963, during Chopra's examination of the electron transportation dynamics within niobium–niobium–oxide–metal thin film architectures, unusual current–voltage behaviors characterized by negative resistance were encountered. The features of niobium oxide-layered structures typically exhibit a progression from linear to exponential current regions, culminating in a sharp current surge that leads to intrinsic failure. However, proximity to this failure threshold often destabilizes these regular patterns, abruptly shifting to a state characterized by negative resistance. This transformation, which tends to be unpredictable and unstable at ambient temperatures, exhibits greater stability at lower temperatures.

The negative resistance region observed here is governed primarily by current modulation, contrasting with voltage-dominated mechanisms observed in phenomena such as superconductor tunneling, Esaki diodes, and select oxide films. As temperatures decrease, the required current density diminishes, necessitating increased voltages to induce a negative resistance state. Notably, the *I–V* characteristics display near symmetry across current flow directions. Moreover, pronounced hysteresis within the voltage characteristics is evident, even under direct current conditions, a characteristic commonly associated with insulating materials possessing numerous trapping sites. This negative resistance region possesses the capacity to sustain oscillations.[134]

In 1965, Hiatt and Hickmott developed a type of niobium oxide diode with bistable switching properties, which was the predecessor of the niobium oxide memristor. He revealed that the *I–V* characteristic of Nb–Nb_2O_5-metal diodes does not rely on the metal electrode, which is incorrect. The *I–V* characteristics of the Nb–Nb_2O_5-metal diode are influenced by the type of metal used before the electroforming process. Moreover, unlike Al_2O_3 diodes with voltage-controlled negative resistance, niobium oxide diodes do not need to enhance conductivity in a vacuum to achieve NDR.[136] Subsequently, in 1969, Hickmott made further progress by developing Nb_2O_5 diodes that exhibited electroluminescence and bistable switching properties. He discovered that conductive and bistable switching (voltage-controlled negative resistance, VCNR) occurs at the singularity point of the oxide, and it is determined by the electronic properties of the insulator rather than the thermal effect at the singularity point. He discovered that the electroluminescence phenomenon and VCNR of the device are related to whether the metal electrode acts as a positive or negative electrode. When the voltage reaches a certain level, electroluminescence occurs regardless of diode polarity.[137] In his research published in 1970, Hickmott further demonstrated that when low work-function metals, such as In, Cd, Zn, or Pb, are used as counter-electrodes in Nb–Nb_2O_5-metal diodes, VCNR occurs in a high conductivity state. He also pointed out the significant influence of the electric breakdown process and impurity energy levels, as well as singularities, on the bistable switching of the device.[138]

In 1976, Gaule *et al.* developed a prototype metal oxide threshold switching (MOTS) device. The MOTS prototype is mounted in a microwave diode housing with niobium strip pressure contacts. Gaule built a series configuration that combined conventional with MOTS devices to protect the receiver input from antenna-generated transients. The aforementioned applications primarily utilized MOTS technology for 'voltage regulation' (or suppression). The authors recognized the potential of integrating MOTS in series with a pulse generator for current control, which can generate steep current pulses. To demonstrate the efficacy of pulse refinement, they conducted an experiment in which the MOTS was substituted with a short circuit. In this scenario, the current pulse profile mirrored that of the applied voltage. Notably, the MOTS functions to "retain" the current flow until a specific threshold is reached. Furthermore, the triggered operations mitigate "time jitter" issues that may arise from slow-rising pulses. Additionally, it is feasible to adjust the main voltage pulse generated to a sub-threshold level. This adjustment diminishes pre-switching leakage current and offers flexibility in precisely tailoring the current pulse by strategically positioning the 100 ns rising-time trigger pulse at an optimal point. Pre-switching becomes feasible owing to the recovery effect outlined, further enhancing the overall performance and versatility of the system.[139]

In 1979, Philipp and Levinson's study established that NbO_x, with an approximate x value of 2, exhibits a remarkable threshold-switching behavior, transitioning swiftly from a state of high impedance to one of low impedance, characterized by a short increasing period, which measures significantly less than 500 picoseconds.[140] In 1979, Vezzoli *et al.* prepared polycrystalline packaged NbO_x devices and single-crystal packaged NbO_x devices and tested the devices for threshold voltage, switching delay time, and residual on-state voltage. Their data suggest a threshold interruption duration of approximately 200 nanoseconds, beyond which a switch-off transition does not occur. This threshold interruption is interpreted as the characteristic lifetime of trapped carriers within polycrystalline NbO_2, reflecting its inherent properties.[141]

In 1981, Vezzoli *et al.* performed double-pulse and pulse-interrupt testing on niobium oxide single-crystal devices and polycrystalline switching devices. They found that the recovery time of the threshold switching phenomenon of the device is very fast, ranging from 0.8 to 1.2 microseconds, and is independent of the polarity of the first and second pulses. The interval between the holding voltage and the transition state is perhaps owing to the lifetime of the carrier trapping process as well as the emission time. The nonstoichiometric compound of NbO_x enables repeatable threshold switching in polycrystalline devices solely when the value of x is greater than or equal to 1.87, signifying this specific oxygen content as the minimum requirement for consistent switching behavior. NDR regions are found in both polycrystalline and single-crystal NbO_x devices, but the difference is that in single-crystal devices, there is no switch off transient present in the on state.[142]

In 1984, Lee *et al.* made high-quality niobium oxide films by reactive ion-beam sputtering and observed for the first time that niobium oxide films could regulate electrostimulation light. As shown in Fig. 5(a), the niobium oxide device *I–V* characteristics exhibit a negative differential resistance segment. As shown in Fig. 8(b) and (c), niobium oxide devices exhibit different transient responses under conditions of no

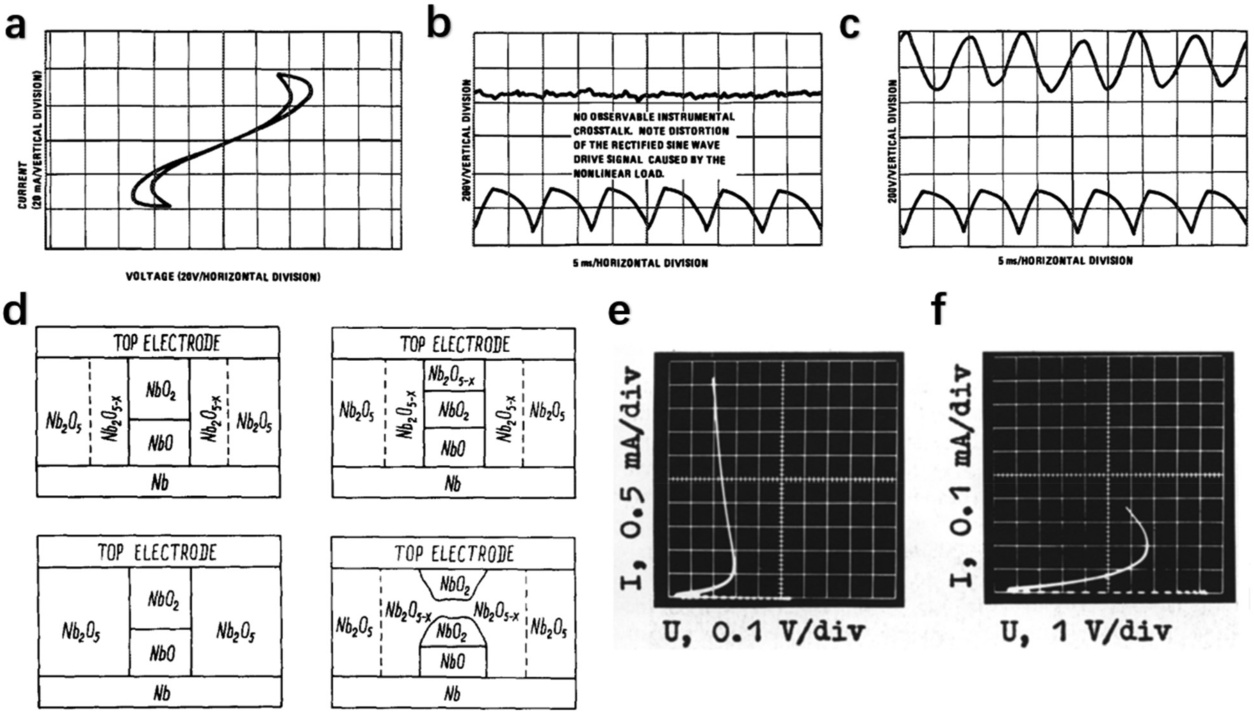

Fig. 5 (a) *I*–*V* characteristic of the NbO_2 device. (b) Temporal modulation response of a device in the absence of light. (c) Temporal modulation of the device under high illumination.[143] (d) Phase diagram of different phase distributions of a-Nb_2O_5 film. (e) *I*–*V* characteristics of current channels in the high conductivity state. (f) *I*–*V* characteristics of current channels in a low conductivity state.[144]

light and strong external light. Experiments have shown that NbO_2, as the basis for a fast electro-optical switch, can be reversibly switched between an open transparent state and a closed reflective state.[143]

In 1985, Boiko *et al.* studied the metal/insulator/semiconductor (MIS) structure of Nb a-Nb_2O_5/MnO_2. As shown in Fig. 5(d), after the electroforming process, there are two situations: one is that the conductive channel (CC) contains only NbO and NbO_2 so that CC is in a high conductive state (HCS). The other is the case in which niobium oxide is still present with a high oxygen content; in this case, CC is in a low conductive state (LCS). It is noteworthy that the junction of niobium oxide and Nb metal electrodes usually forms NbO. As shown in Fig. 5(e) and (f), the presence of different crystal phases between the niobium layer and the top electrode affects the conductive state and thus affects the NDR properties. Experimental results showed that thin insulator film interaction caused permanent electrochemical breakdown in the MIS structure, followed by step-like electrothermal breakdown under certain conditions.[144]

In general, early research on niobium oxide can be divided into three stages. The first stage is the phenomenal observation stage. In 1963, Geppert *et al.* first observed the room temperature negative resistance effect in niobium–niobium oxide structures and achieved sustainable oscillations of $\leq$6 MHz and found the 100 MHz parasitic oscillation phenomenon. In the same year, Chopra revealed nonlinear current–voltage characteristics and a more stable negative resistance state at low temperatures in niobium–niobium–oxide–metal thin films. In 1965, Hiatt *et al.* developed bistable switching niobium-oxide diodes (Nb–Nb_2O_5-metal structure) but misjudged that their electrical characteristics were electrode-independent (in fact, they were affected by metal type). The second stage is the mechanism analysis stage. Hickmott confirmed in 1969 and 1970 that electrode polarity affects electroluminescence and voltage-controlled negative resistance (VCNR) and that low work function metal electrodes (In, Cd, *etc.*) can induce high-conductance VCNR and revealed the key roles of electrode breakdown and impurity energy levels in bistable switching. Philipp *et al.* in 1979 clarified that NbO_2 can have sub-500 picosecond ultrafast threshold switching behavior. In the same year, Vezzoli *et al.* used the characteristic lifetime of trapped carriers within polycrystalline NbO_2 to explain the threshold interruption. Vezzoli *et al.* in 1981 demonstrated that the NbO_2 threshold recovery time is independent of pulse polarity and attributed it to the lifetime of the carrier trapping process as well as the emission time. The third stage is device application and performance optimization. Gaule *et al.* developed metal oxide threshold switches (MOTS) in 1976 for antenna transient protection, pulse shaping, reduction in pre-switching leakage current and suppression of time jitter. In 1984, Lee *et al*. first observed the electrical stimulation optic modulation ability of niobium oxide thin films, leading to light-reversible switching between transparent and reflective states, laying the foundation for high-speed electro-optical switching.

Even though there have been many studies on the electrical properties, memristor properties of niobium oxide, there are still many questions that need to be solved, verified and explored. Therefore, numerous studies need to be conducted.

4.2 Mechanism governing the NDR behavior of niobium oxide

There are different opinions in the academic community about the generation of negative differential effects in niobium oxide devices, such as the Mott metal–insulator transition (Mott-MIT),[114] Peierls transition,[145] threshold switch triggered by changes in electronic structures[62] and analytical models based on Poole–Frenkel *et al.*[146] In this section, we present some studies on the mechanisms of negative differential resistance generation in niobium oxide.

4.2.1 Mott insulator–metal transition and Peierls transition. In 1968, Mott[47] proposed a new mechanism for the transformation of metal insulators by considering strong electron–electron interactions, which is based on Wilson's theory.[147] The new mechanism is known as the Mott metal–insulator transition (MIT). Briefly, Mott MIT is the field-induced increase in charge carrier concentration that shields the Coulomb interaction, leading to the elimination of the Mott–Hubbard energy band at $T < T_t$.[47]

Mott MIT is a mechanism that can cause threshold switching (TS). The threshold switching phenomenon is a change in the resistance value, which is the same as the conductivity change when the NDR is generated. Threshold switching occurs when the voltage across both sides of the device reaches a specified threshold voltage, leading to sudden changes in resistance and resulting in a rapid increase or decrease in current. When the voltage drops below the threshold, the device returns to its initial resistance state. This switching between high and low resistance states in response to the magnitude or polarity of the voltage resembles the operation of a switch, hence the term 'threshold switch'.[148]

Researchers have begun to think about what structures of materials would yield such an insulator–metal transition. For example, some nonstoichiometric oxide systems, such as NbO_x, where x is not a discrete value but can be a continuous value. Such systems have been shown to consist of a series of homologous discrete phases. Such shear structures have regular spacing of planes, and generating stabilization about the new periodicity only requires entropic energy greater than that required for diffusion to occur, *i.e.* sufficient temperature. Similar to the metal–semiconductor transition, a narrower energy band leads to improved stabilization. The extensive inclusion of d-orbital electrons in such systems gives such oxide systems the potential to undergo insulator–metal transitions.[149,150]

4.2.1.1 Electroforming. The generation of threshold switches usually requires an electroforming process, which is generally owing to crystallinity or channel formation,[7,114] but this is also related to the anodic oxide film (AOF) generated, where the probe comes into contact with the film.[39] The electroforming process typically involves repeated scanning of the device with a high voltage and low compliance current to achieve a "soft" breakdown. The occurrence and extent of forming are related to the insulating material, electrode material, temperature and the atmosphere during the forming process. Moreover, the formation voltage did not depend on the thickness. When the thickness of the insulating material is greater than 1 μm but less than 10 nm, electroforming is almost impossible to achieve. The magnitude of the voltage V_F can be approximately calculated by performing simple operations on the Gibson free energy, bandgap energy or Madelung energy.[48]

Some researchers have proposed models for the changes that occur during the electroforming process. For instance, Hickmott proposed that impurities in insulators undergo the Pool-Frenkel process, leading to the formation of impurity energy bands while carrying surface charges. Consequently, electrons can enter the crystal without the need for thermal excitation, thus completing the electroplating process.[151] Simmons and Verderber proposed that the forming process occurs because the metal ions in the electrodes enter the insulator, thereby creating a broad band of impurities that can conduct electricity. Interestingly, this model was met with much skepticism at that time, but now it has become a category of memristors, namely the conductive bridge type memristor.[46] Dearnaley proposed that the contact interface between the metal electrode and the insulator is not smooth, resulting in particularly high voltages in some areas, causing the insulator structure to change and form a conductive filament, until it connects the upper and lower electrodes.[48] Furthermore, there are models such as Greene's model, which accurately explains the formation process of ionic crystals, and Barra's model, which discusses ion conduction, spatial charge conduction, and the generation of electron traps, among others.[48]

It is noteworthy that the electroforming process here is different from the electrically triggered NDR, but rather a voltage (or current) that helps the device obtain the preconditions for MIT to be able to occur, and the specific case of electrically triggered NDR is discussed hereinafter.

In vanadium-based and niobium-based structures, the electroforming process usually leads to S-type NDR curves. In the presence of an applied electric field, oxygen ions are transported and recombined with the metal electrodes, *e.g.* $Nb + Nb_2O_5 \rightarrow NbO_2$, to produce NbO_2. The area where NbO_2 is formed is often referred to as a dendritic channel or oxygen vacancy filament.[156] The filament is more likely a spheroid-shaped nucleus, which is composed of metallic rutile NbO_2, as shown in Fig. 6(a).[152] Another explanation is that the movement of oxygen ions leads to the formation of oxygen vacancies, and the resulting oxygen vacancy channels are a sign of the completion of electroforming, but essentially, it is the same. The anoxic regions, where these oxygen vacancies are enriched, lead to a decrease of x in NbO_x, close to 2, leading to the accumulation of niobium dioxide, as shown in Fig. 6(b).[153] The oxides of these metal phases dominate in the channels and therefore accumulate, leading to an irreversible increase in conductivity, *i.e.* the completion of electroforming. During subsequent voltage sweeps, these channels undergo a Mott insulator–metal transition, enabling resistance switching.

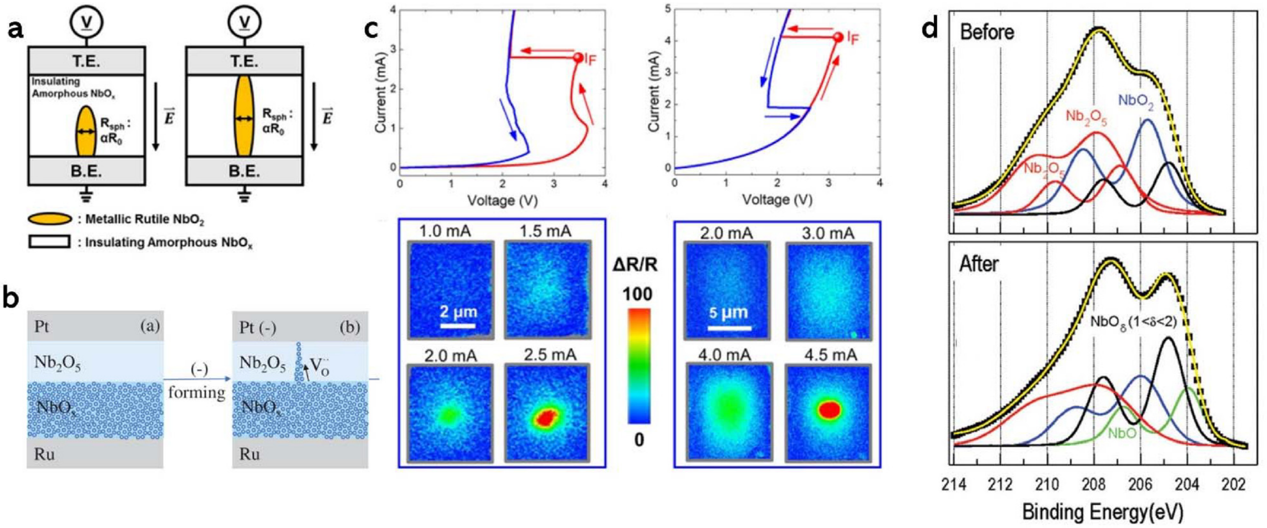

Fig. 6 (a) Metallic rutile NbO$_2$ nucleation process during electroforming.[152] (b) Schematics of the electroforming mechanisms in the NbO$_x$ device.[153] (c) Electroforming characteristic and *in situ* thermos reflectance mapping of devices with areas measuring 5 × 5 μm^2 and 10 × 10 μm^2.[154] (d) XPS spectra before and after electroforming.[155]

It has been reported that S-type NDRs are the result of electrothermal instability in these channels.[157]

Electroforming time and number of cycles may vary from experiment to experiment.[156] What is more, niobium oxide of different crystallinities and different chemical compositions requires different electroforming conditions.[158] As shown in Fig. 6(c), the researchers performed situ thermo-reflectance measurements using a camera-based thermo-reflectance imaging system. The research found that after applying different amounts of current electroforming, a large contrast in the thermal reflection at the electroforming center proved the conjecture of the electroforming model.[154] Further, Fig. 6(d) illustrates directly the characterization of changes in the composition of the different phases of niobium oxide within the device before and after electroforming through XPS spectroscopy tests, illustrating the role of the electroforming process in oxygen ion migration, which leads to the formation of niobium dioxide and local regions with even less oxygen content.[155]

4.2.1.2 Structure transitions. The insulator–metal transition that occurs in niobium oxide is also associated with a change in structure, the Peierls transition. The increase in the lattice constant causes the boundary of the Brillouin zone to move. When the Brillouin zone moves to the Fermi surface, owing to the existence of an energy gap at the boundary of the Brillouin zone, which lowers the energy of the electron system, the energy band splits, and the electrons fill the energy band, turning it from a half-full band to a full energy band; this is when the material transforms from a metal to an insulator, and *vice versa*. This transition is known as the Peierls transition.[159–162]

The structural change that occurs in niobium oxide is, specifically, the transition from the original body-centered tetragonal (BCT) phase, which is a high-resistance state, to the low-resistance metallic rutile phase, as shown in Fig. 7(a). This transformation corresponds to the NDR-2 stage. A detailed account of the different NDR stages is provided in Subsubsection 4.2.3. Niobium oxides other than niobium monoxide are usually periodically arranged in octahedral crystals.[163] Nb-4d in octahedral crystals has a fivefold degenerate orbital and splits into two orbitals: a high-energy e_g orbital with a double degenerate orbital and a low-energy t_{2g} orbital with a triple degenerate orbital. After niobium oxide turns into a BCT phase, the t_{2g} orbital further splits into a π* orbital and a $d_{\parallel}$ orbital, while dimerization of the Nb–Nb pair causes $d_{\parallel}$ to split again into the high-energy band $d_{\parallel}$* and the low-energy band $d_{\parallel}$, as shown in Fig. 7(b). Additionally, the existence of soft phonon modes specifically located at the tetragonal *P*-point within the rutile Brillouin zone has been empirically verified and theoretically confirmed as pivotal initiators of the Nb–Nb dimerization process.[165,166] The diminishing of Nb–Nb dimers over a wide temperature range suggests the involvement of a secondary Peierls mechanism, which controls the opening of a pseudo-gap, thereby driving the metal-to-insulator transition in NbO$_2$.[164,167] The role of the Nb dimer is also further verified by probing changes in the length of the niobium–niobium dimer by temperature-dependent extended X-ray absorption fine structure spectroscopy (T-EXAFS) (Fig. 7(c)).[164] As shown in Fig. 7(d), after the splitting of the energy bands, a phase of completed insulation is formed, *i.e.* a transition from a metallic phase to an insulator phase is completed, and *vice versa* in a similar way. During this process, NDRs are generated, and the successive NDR behavior is a result of the gradual enlargement, or gradual growth, of the region in which MIT occurs.[126]

4.2.1.3 Temperature effects. It is clear that temperature is critical for the insulator–metal transition to occur in niobium

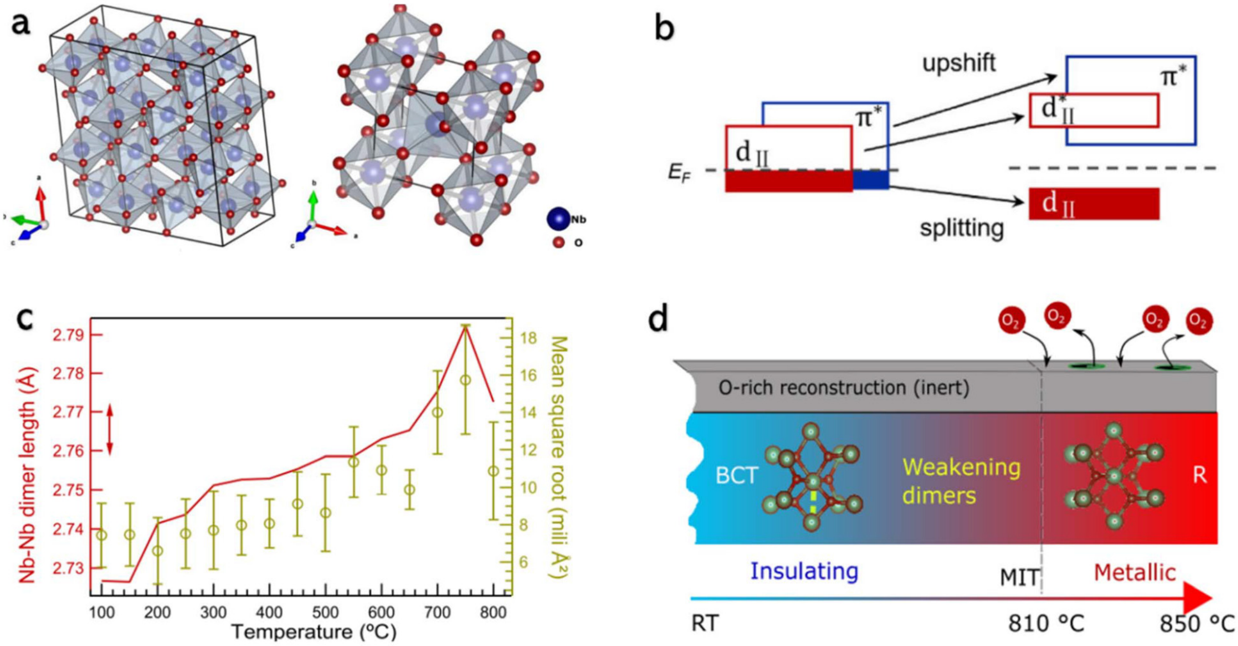

Fig. 7 (a) Body-centered tetragonal phase and rutile phase of niobium oxide.[163] (b) $d_{||}$ energy band split during MIT.[126] (c) Nb–Nb dimer length variation with temperature, which is characterized by temperature-dependent extended X-ray absorption fine structure spectroscopy (T-EXAFS). (d) Schematic representation of the insulator–metal transition of niobium oxide.[164]

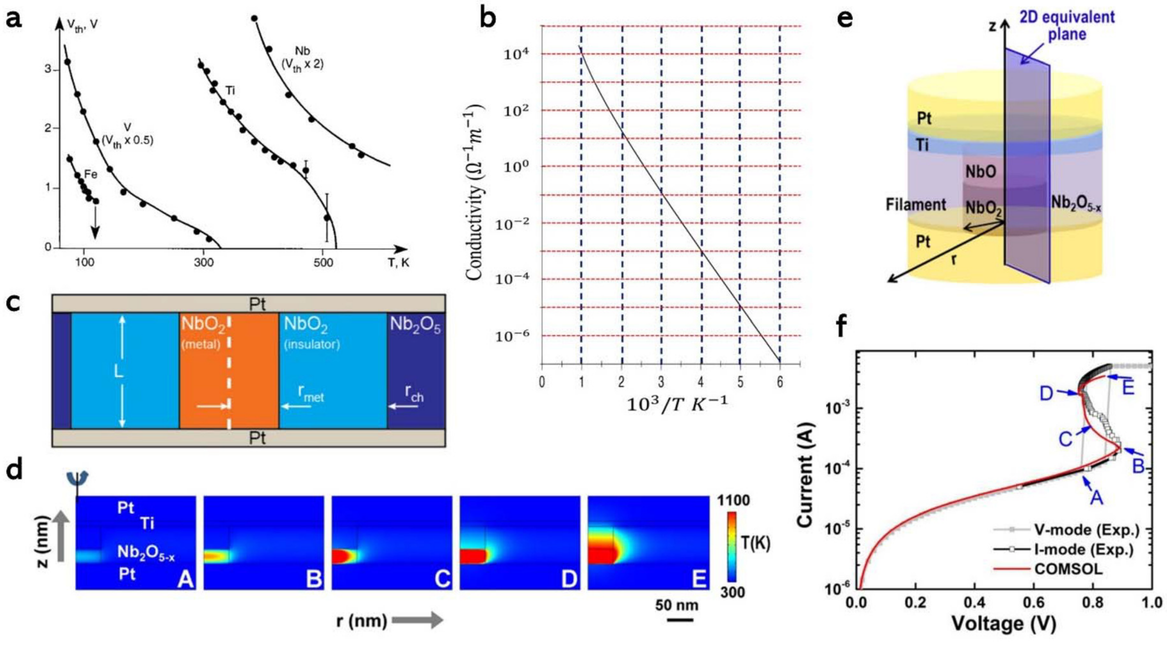

Fig. 8 (a) Temperature dependence of threshold voltage in metal–oxide–metal (MOM) structures with different elements.[157] (b) Variation of niobium oxide conductivity with temperature calculated from the fit.[168] (c) Cross-section of the device in operation, with metallic phase niobium dioxide in the middle cylindrical region.[114] (d) 2D simulation of the temperature in the device structure during scanning. MIT occurs in the red region. (e) Geometry of the analogue device with the conducting channel/filament in the middle.[170] (f) Simulated and actual device *I*–*V* characteristic curves.[170]

oxide, as the causes of structural phase transitions are usually temperature dependent, as shown in Fig. 7(d). Temperature intuitively affects the electrical properties of niobium oxide devices. For oxides, such as vanadium, iron, and niobium, the threshold voltage decreases as the temperature increases, but this change is non-linear, as shown in Fig. 8(a).[157] The successful fitting of the fitted function for the temperature *versus* conductivity relationship (Fig. 11b) serves as complementary evidence for the second-order Peierls transition as the MIT mechanism in niobium dioxide.[168] In addition, the NDR effect may also be due to the self-heating Schottky emitter.[169]

As shown in Fig. 8(c) [114] and Fig. 8(e),[170] many models have been proposed to describe temperature variations in the device, and the areas with large temperature variations are exactly those where functional layers, or channels, are formed.[171] As observed in ref. 172 and Fig. 8(f),[170] different positions of the NDR curves generated during the current scanning process correspond to different temperatures, and these points correspond to the two-dimensional temperature map simulation depicted in Fig. 8(d),[170] proving the feasibility of the models. However, this also raises the question of when NDR occurs, which corresponds to a temperature of around 400 K. This temperature is much lower than the temperature at which niobium oxide undergoes the Mott insulator transition, which is around 1080 K.[100,169,173]

In subsequent sections, we discuss studies that elucidate that conduction behaviour is dominated by mechanisms such as electric field drive and Poole–Frenkel emissions.

4.2.2 Electrically driven mechanisms.

The prevailing explanation for the phenomenon of resistance switching in niobium oxide, also known as threshold switching NDR, is based on a Joule-heat-assisted semiconductor conductivity mechanism, which is usually electrically driven. Examples include a field-induced thermal runaway and a nonlinear transfer mechanism consisting of multiple mechanisms, as shown in Fig. 9(a) and (b).[126] Additionally, the mismatch between the resistance change occurring at the threshold voltage, which is larger than the resistance change that occurs with the phase transition in niobium dioxide, has increased the controversy about the Mott MIT in niobium oxide, leading to the support of an electrically driven mechanism.[62,174] This section focuses on the Poole–Frenkel effect, small polar-conduction mechanism, and activation energy E_a, which play a role in electrically driven mechanisms.

4.2.2.1 *Poole–Frenkel effect.*

The Poole–Frenkel (PF) effect describes how, in an electric field, electrons can easily enter the conduction band without large thermal energy, which is similar to Schottky emissions.[178] Schottky emission and the Poole–Frenkel effect occur owing to the reduction of the Coulomb potential barrier when an external electric field is applied. Donor sites, acceptor sites, traps, and electrons in the valence band are all affected by the PF effect. Because of the existence of traps and the fact that they carry positive charges (fixed image charge) when empty, the PF effect diminishes the barrier amplitude more significantly than the Schottky emission.[179] From a different viewpoint, under a DC electric field, the dielectric layer produces spatial polarization, and the movement of oxygen vacancies results in the accumulation of a large number of positive charges on the negative electrode surface. Once the electric field strength between the positive and negative electrodes reaches a certain value, it forces the electrode to emit electrons, or directly from the dielectric layer on the electrodes to emit electrons,[179,180] as shown in Fig. 9(c).[175]

Shin *et al.*[62] investigated the field-switching characteristics of niobium oxide devices, explaining the first stage of the switching mechanism, the electric-field-assisted PF mechanism, and the second stage of the thermal runaway based on the PF conduction model. Random thermal fluctuations give electrons enough energy to leave the localized state and move

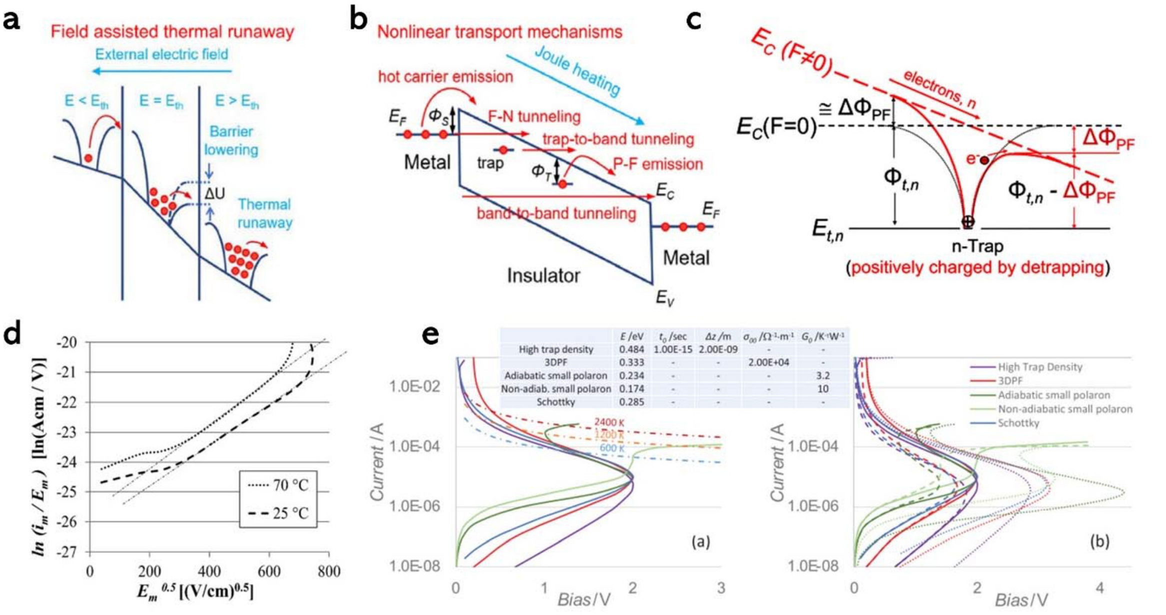

	E /eV	t_0 /sec	Δz /m	σ_{00} /$\Omega^{-1}\cdot m^{-1}$	G_0 /$K^{-1}W^{-1}$
High trap density	0.484	1.00E-15	2.00E-09	-	-
3DPF	0.333	-	-	2.00E+04	-
Adiabatic small polaron	0.234	-	-	-	3.2
Non-adiab. small polaron	0.174	-	-	-	10
Schottky	0.285	-	-	-	-

Fig. 9 (a) Field-assisted thermal runaway model of electrical-driven NDR. (b) Nonlinear transport mechanisms of electrical-driven NDR.[126] (c) Schematic of the PF effect with and without electric field.[175] (d) Plot of PF characteristics at different temperatures, indicating PF conduction occurring below the threshold voltage.[176] (e) Simulation of the current–voltage characteristics of five conduction mechanisms.[177]

into the conduction band. Once in the conduction band, the electrons can move through the crystal for a short time before relaxing again into another localized state, that is when the localized dissipated power reaches a specific value, thermal runaway allows the barrier to be lowered and threshold switching occurs.[181] It has also been hypothesized that self-heating effects lead to the collapse of the electronically ordered state, resulting in the current-controlled NDR effect (CC-NDR). The difference here with the temperature factor discussed in the MIT chapter above is that it is based on nonlinear transport mechanisms, such as the PF effect, which focuses more on changes at the electronic level rather than the structural level.

To verify this assumption, the researchers constructed quasi-static circuits and built physical models, revealing that a significant reduction in device resistance occurs at 150 K in response to the PF effect, such as the PF plot at 25 °C and 70 °C (Fig. 9(d))[176] and the simulation of the current–voltage characteristics of five conduction mechanisms (Fig. 9(e)).[177] The images illustrate how lower currents lead to reduced Joule heating. Incorporating thermal isolation causes the *I–V* characteristics to deviate from the influence of ambient temperature, consequently altering the NDR. Additionally, the combination of activation energy and thermal isolation significantly lowers sub-threshold currents, maintaining the NDR within the desired range.[177] In a word, these explain that the PF conduction mechanisms play a significant role in the threshold effect and the negative differential resistance effect.

4.2.2.2 *Small polaron-conduction mechanism.* The CC-NDR is usually thought to arise from strong electron coupling to phonons in small polaron hopping systems.[182] The electric field increases the effective radius of the polariton and decreases the binding energy of the polariton; eventually, the trapped carriers are released.[62] This can be referred to as the field-triggered thermal runaway model (FTTR), in which the NDR effect is triggered by a combination of a change in conductivity driven by an electric field and a decrease in electronic conductivity due to Joule heating. A PF effect type of barrier reduction was included in the model. The FTTR-based model overcomes the contradiction between large temperature dependence and small hysteresis at threshold switching in the MIT model.[183,184]

4.2.2.3 *Activation energy (E_a).* The electrically triggered NDR effect is related to the level of activation energy. The activation energy E_a is the minimum energy required to overcome the reaction barrier and initiate a reaction. As shown in Fig. 10(a), the electric field-triggered thermal runaway model (FTTR) model illustrates that owing to the Poole–Frenkel effect, the activation energy is reduced, and a certain number of carriers are excited to escape.[183] As shown in Fig. 10(b), when the activation energy is small, *i.e.* below 0.15 eV, no NDR is generated.[185] Increasing the activation energy, E_a, causes the leakage current to decrease, but it leads to an increase in the threshold voltage, and if the threshold voltage exceeds the breakdown limit, the device breaks down, as shown in Fig. 10(d).[186]

4.2.3 Principles of multiple NDR effects. Negative differential resistors in niobium oxide are current-controlled S-type rather than voltage-controlled N-type dependencies. There are two types of S-type NDRs, the typical S-type NDR behavior

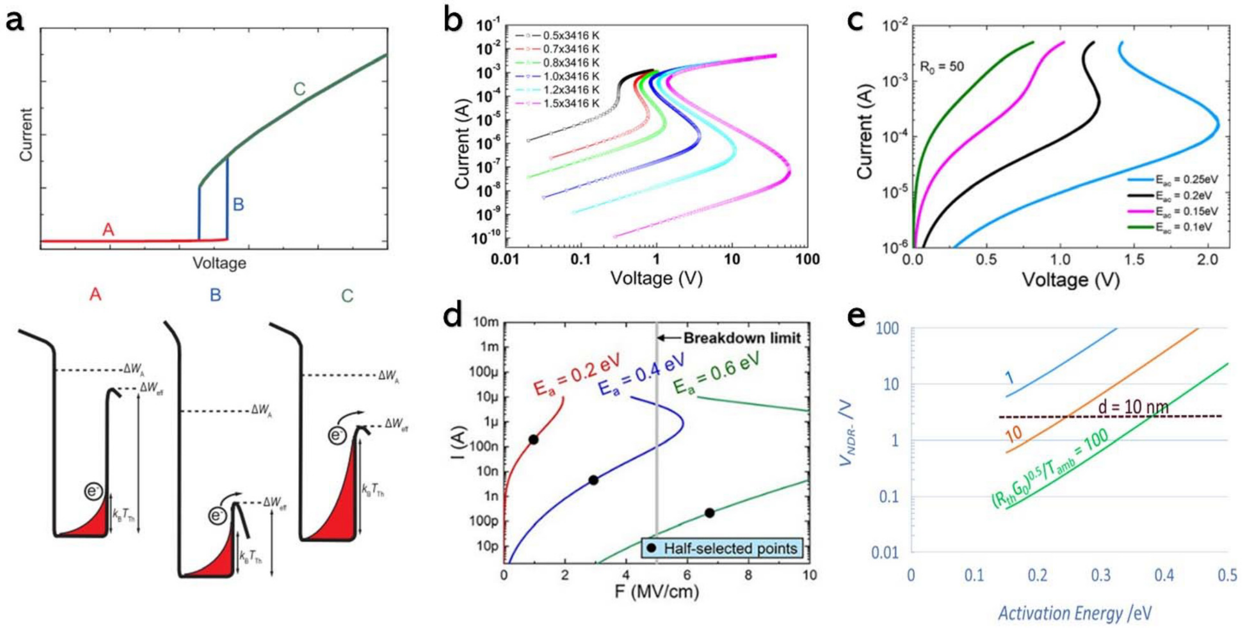

Fig. 10 (a) Electric FTTR model.[183] (b) Calculated *I–V* characteristic curves for different activation temperatures.[182] (c) Effect of activation energy on negative differential resistance.[185] (d) The effect of the change in activation energy on the leakage current (*i.e.*, the current corresponding to the black dot in the figure) is such that too much activation energy can cause the threshold electric field to break through the limit.[186] (e) Plots of activation energy *versus* NDR turning point voltage corresponding to different voltage prefactors (1, 10, 100).[177]

(S-NDR) and the Snap-Back NDR behavior (SB-NDR), which are called NDR-1 and NDR-2, respectively. NDR-1, or S-NDR, is easy to observe and appears before SB-NDR in the scanning process. The question of how to obtain SB-NDR and the underlying principle of SB-NDR generation have attracted the interest of researchers.

First, only a certain oxygen content of niobium oxide can produce a negative differential resistance (NDR) effect, which collates the oxygen content intervals that can produce an NDR, as shown in Fig. 11(a).[187] Temperature is a factor that affects SB-NDR, as shown in Fig. 11(b).[173] The S-type and SB-NDR were observed at high temperatures (323 K) and slightly lower temperatures (293 K), respectively. This phenomenon can be explained by the shell model, in which the niobium oxide layer between the upper and lower electrodes can be treated as a core in the middle, acting as a parallel resistor. This was mentioned in the previous section on the temperature dependence of the Mott and Peierls transition. When the current is applied, the shell resistance (R_s) and maximum negative resistance of the core (R_{NDR}) decrease with temperature, but the heat dissipation of the core is poor, so the temperature of the core is high and the core resistance decreases more than the shell resistance.[173]

The area of the device also impacts the NDR, and a larger device area results in a larger shell layer, which in turn corresponds to a smaller resistance. The magnitude of the shell layer resistance and the interface (between the electrode and the functional layer of niobium oxide) resistance has a crucial influence on the generation of SB-NDR.[189] Experimentally, as shown in Fig. 11(c), it is proven that a device with a small area usually tends to show S-type NDR, and a device with a large area usually shows SB-NDR.[173] The left part of Fig. 11(c) indicates that the thickness and the area affect the NDR effect when $x = 2.05$ in NbO_x, and it can be observed that the size of the area slightly affects the negative differential effect of niobium oxide with a high oxygen content. The device area cannot be used as the only basis for judgment; for example, when x is 1.92, in NbO_x, a smaller device area can also show SB-NDR. However (in the right part of Fig. 11(c)), if x is 2.6, then owing to the high oxygen content, niobium oxide shows insulating properties with large resistance, making it difficult to observe SB-NDR by varying the device area. As shown in Fig. 11(d), in terms of thickness, a thick niobium oxide layer leads to the disappearance of SB-NDR.[173] In this case, the size of the electrode area also slightly affects the threshold voltage. As shown in Fig. 11(e) and (f), it is also worth mentioning that, to generate SB-NDR, the shell resistance R_s must be less than R_{NDR}.[148,188] As shown in Fig. 11(f), when R_s is greater than R_{NDR}, the memristor device shows a smooth S-NDR characteristic without hysteresis. When R_s is less than R_{NDR} and less than R_C, the memristor device shows SB-NDR characteristics with hysteresis. R_C is defined as $R_C = \frac{V_{th}-V_h}{I_h-I_{th}}$, where the V_{th} is the threshold voltage, V_h is the hold voltage, I_{th} is the threshold current, and I_h is the hold current. When R_s is less

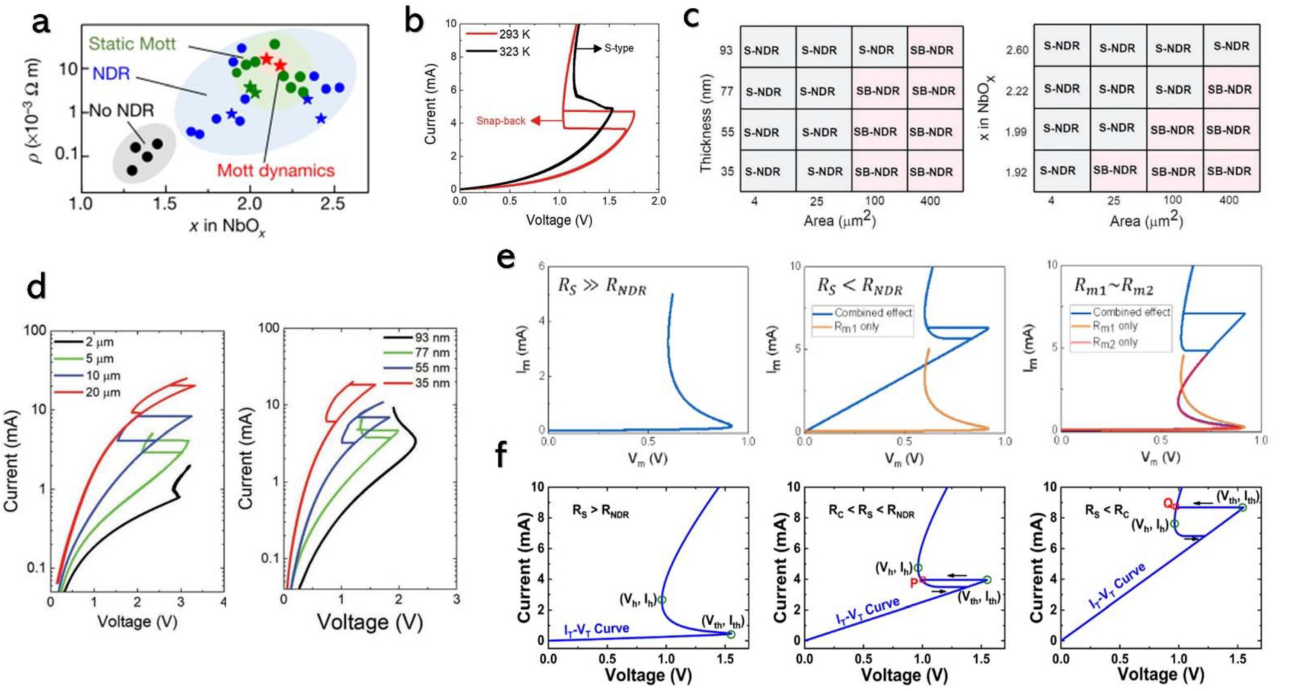

Fig. 11 (a) Relationship between niobium oxide oxygen content and NDR effect, and the corresponding resistivity.[187] (b) Influence of substrate temperature on the negative differential resistance effect. (c) Effect of device area, thickness and oxygen content on the negative differential resistance of niobium oxide, expressed as a matrix. (d) NDR characteristic *IV* curves are presented under different conditions.[173] (e) Different NDR characteristic curves exhibited at different shell resistances.[148] (f) S-NDR and SB-NDR characteristic curves are exhibited when the shell resistance is equal to 1200 Ω, 400 Ω, and 180 Ω.[188]

than R_C, the device shows SB-NDR characteristics with hysteresis; this hysteresis occurs at a different location, and the magnitude relationship between V_{th} and V_h changes.[188]

In a more fundamental way, the crystal structures of niobium oxide play a significant role when it comes to composite NDRs. The structural transition between the body-centered cubic tetragonal phase and the rutile phase is mentioned in the previous section, and the transition presupposes the presence of NbO_2-enriched regions, or dendritic channels, or oxygen vacancy channels.[190] The appearance of electrical resistance is also primarily owing to the amount of NbO_2 within the functional layer. Electroforming and annealing processes contribute to the formation of such NbO_2 crystals, and researchers have also found irreversible crystallization during current scanning. The researchers measured temperature mapping using the *operando* thermal reflection technique. Fig. 12(a) shows the temperature variations during current scanning, with NDR-1 occurring around 390 K and NDR-2 around 990 K. Fig. 12(b) shows the temperatures corresponding to different data points (α, β, γ, δ). Using synchrotron X-ray spectro microscopy, the researchers discovered that the crosspoint area remained unchanged both in the absence of current and when a sufficiently large current was present to trigger NDR-1. As shown in Fig. 12(c) and (e), the logarithmic ratio, which represents the optical density (OD), reveals that a chemical or electronic response to the current occurs near the magnitude of the current sufficient to trigger NDR-1, while at the magnitude of the current sufficient to trigger NDR-2, the electronic response to the current occurs near the magnitude of the current sufficient to trigger NDR-2. The overall OD value is larger near the current size sufficient to trigger NDR-2. As shown in Fig. 12(d), the no-current and low-current cases resulted in a spectral difference at the 0-K edge possibly owing to lattice expansion caused by Joule heating. The downshifting of both the π* and σ* bands demonstrates the MIT-induced increase in conductivity, as well as the Peierls distortion appearing in the lattice structure.[100]

In summary, NDR-1 is current-controlled, with a thermal runaway owing to nonlinear electron transport (Poole–Frenkel conduction, thermionic emission, and polaron hopping), which is independent of the crystallinity of the material. However, the high-current counterpart, SB-NDR, is temperature controlled, with the transformation of crystalline NbO_2 from an insulating phase to a metallic phase, which has a lower thermal conductivity, and a further increase in the internal temperature, with a further decrease in resistance.

4.3 Performance modulation of NDR in niobium oxide memristors

The threshold voltage and holding voltage of the NDR characteristic curve during the current scan correspond one-to-one with the threshold voltage and holding voltage of the voltage window in the voltage scan. Therefore, the resistance switching performance, selectivity, retention, cycling, and other properties of the memristor can be modulated by modulating the effect of the NDR. Typically, comparative studies are conducted

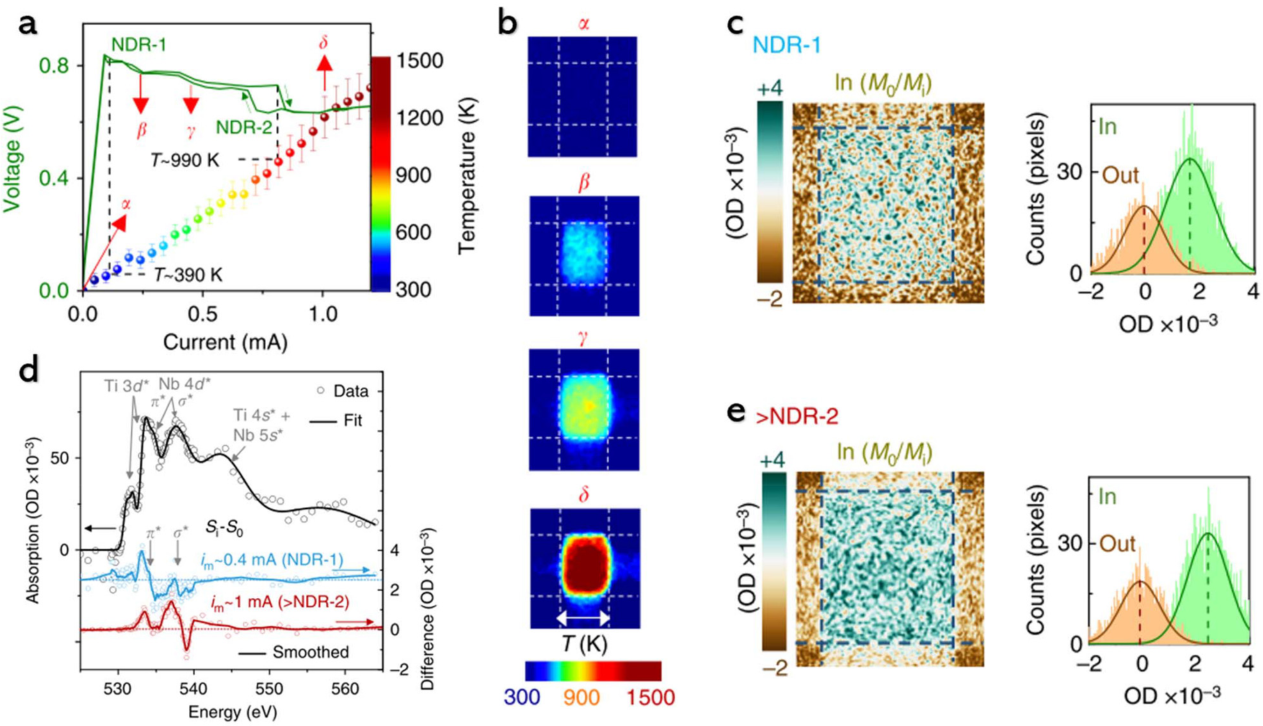

Fig. 12 (a) Experiment I–V characteristic curves and the temperature at different data points. (b) Temperature maps of the device at different data points. (c) Variation in optical density under irradiation by asynchronous X-ray pulses at low currents. (d) X-ray absorption spectra of the device. (e) Variation in optical density under irradiation by asynchronous X-ray pulses at high currents.[100]

directly through the voltage-scanned resistance switching window to achieve modulation,[126,191] but some researchers also adjust the current-scanning NDR characteristics for regulation.

The previous sections discussed more about exploring the mechanisms of NDR generation and the discussion about performance. This subsection focuses more on the application aspect of the NDR for performance modulation. The NDR characteristic inherently leads to self-sustained oscillations of the device. By controlling the NDR characteristics, the oscillation characteristics of the device can be adjusted. Self-induced oscillation can be generated only when the source voltage and load resistance meet certain conditions.[192] At present, from the intuitive control of the resistance switching curve under the voltage sweep, the relationship between the NDR characteristics and the oscillation characteristics is not well defined, and further research is anticipated in this area.

4.3.1 Doping of niobium oxide. To improve the uniformity and stability of the niobium oxide device, some researchers have doped niobium oxide with titanium, aluminum, gold and other metals.[126] As shown in Fig. 13(a) and (e), both the threshold voltage and the holding voltage decrease, and the two voltages are closer to each other as the niobium oxide-doped titanium increases, resulting in a smaller window and disappearance of NDR.[185] Because of the high conductivity of titanium, filamentary conduction (the formation of conductive filaments) is affected by titanium doping, so the electroforming process is altered, as shown in Fig. 13(b).[185] Titanium doping can regulate the oxygen vacancies and optimize the device performance, but excess titanium doping can lead to a disappearance of the resistive characteristic, which is more suitable for use in selectors (Fig. 13(c)), but also has a homogeneous self-compliant characteristic.[193]

Researchers have obtained high-amplitude pulse spikes by doping gold nanodots in niobium oxide devices.[194] The gold nanodots can increase the threshold voltage and turn-on current by modulating the oxygen content at the electrode-oxide interface. As shown in Fig. 13(d), the NDR characteristics of the devices with the addition of gold nanodots have a larger transition voltage and a larger transition amplitude. This is related to the high conductivity of gold, which plays a role in electronic nonlinear transport in the NDR-1 region, while its high thermal conductivity also influences the thermally induced Mott-MIT in the NDR-2 region.[194]

The aluminum element is also a good doping choice; doping aluminum in niobium oxide devices can limit the migration of oxygen ions and enhance the reliability and cyclability of the device.[195] The doped device, also known as the optimized device OD, has a better resistance switching window and a larger resistance switching ratio.[196] During the electroforming process, oxygen ions undergo directional migration, forming oxygen-rich regions (Nb_2O_5), oxygen-deficient regions (NbO_2) in the functional layer of niobium oxide, and NbO_2 aggregates to form conductive filaments (CFs).[197] The Schottky distance is the distance from which the conductive filament reaches the bottom electrode. Doped with Al, the Schottky barrier height rises, and thermally excited electrons find it relatively difficult to cross the barrier. Therefore, when doping with Al, the resistance rises, allowing the device to obtain a higher threshold voltage. In addition, Al

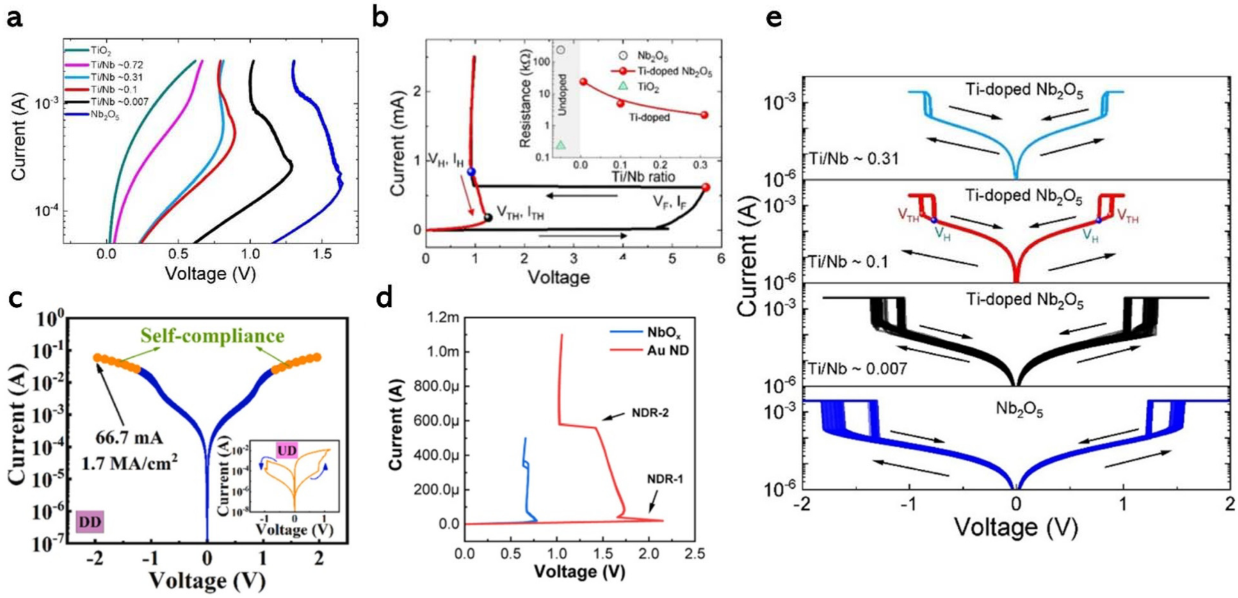

Fig. 13 (a) Plots of variation in the negative differential resistance effect obtained by doping niobium oxide with different amounts of titanium.[185] (b) Electroforming process of the device; the inset page shows the low-field device resistances.[185] (c) *I*–*V* characteristic curves of the doped device (DD) are compared to those of the undoped device (UD) in the absence of compliance current.[193] (d) Comparison of negative differential resistance behavior before and after Au doping.[194] (e) Threshold switching diagrams for devices with different doping levels under voltage sweeps.[185]

doping can constrain oxygen vacancies; the inhibited random migration of oxygen vacancies can improve the uniformity of the device.[195]

4.3.2 Modulation of NDR behavior by temperatures. The annealing process is a crystallization process, and after annealing, the sample undergoes a significant increase in crystallinity and conductivity but a decrease in forming voltage. More essentially, the localized Soret effect based on the current localization and thermophoresis of oxygen plays a significant role in the annealing process.[198] The temperature of the annealing process affects crystallinity and, therefore, the NDR characteristics. As shown in Fig. 14(a), the device before annealing does not have NDR-2 characteristics, and the transition voltage increases with annealing temperature.[158] However, further increasing the temperature may reduce the transition voltage, as shown in Fig. 14(b).[198]

Upon device operation, an increase in ambient temperature leads to a decrease in the transition voltage and an increase in the leakage current, as shown in Fig. 14(c) and (d), which are well fitted to the computational and experimental data. This may be due to the increased energy of electrons inside the NbO_2 functional layer, which results in the collapse of the charge-ordered state, making it more susceptible to field-assisted thermal runaway, namely, reduced switching threshold voltage.[182] Similarly, after the temperature of the device increases, both the threshold voltage and the holding voltage decrease as the temperature increases. Above 378 K, even the NDR effect disappears (Fig. 14e).[199] As the temperature increases, the oscillation frequency increases and the amplitude decreases (Fig. 14f).[199] However, this thermal response needs to be within a certain temperature range, and by proper heating, the pulse pattern can be modulated to optimize the performance of the neural network and enhance recognition capability.[200]

4.3.3 Impact of device size on NDR behavior. The influence of device thickness, device size, and oxygen content on the NDR behavior was described earlier when the origin of the multiple NDR effect was introduced.[173] More information on the influences in terms of device size is provided in this section.

In a memristor array, owing to the demands of micro-nano-fabrication, a sufficiently thick device is required between the word line and the bit line, and an upper current limit needs to be set to balance the threshold voltage and the leakage current to avoid the current flowing through the word line and the ground line to the neighboring devices. Additionally, reducing the device diameter helps to reduce the threshold voltage and leakage current. As can be seen from the change in device size, the ratio of I_{on}/I_{off} has undergone some changes, while the threshold voltage has changed significantly, as shown in Fig. 15(a).[182] The effect of device size on NDR may also be due to the leakage of current through screw dislocations. The NDR phenomenon is not easily observed in devices with larger areas.[55] This modulation of the threshold switching voltage allows the device to be adapted to different application scenarios and to operate stably without being as susceptible to environmental influences as temperature.

When constructing composite circuits, such as selectors and nerve pulse circuits, in addition to the performance of

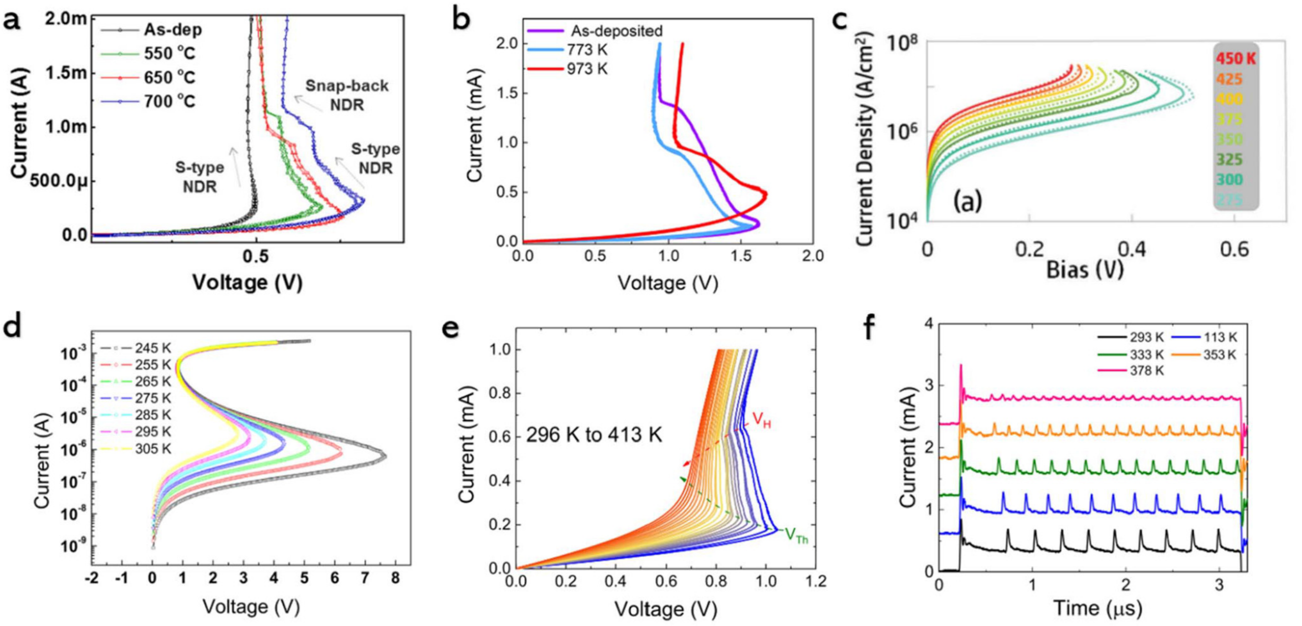

Fig. 14 (a) NDR behavior of niobium oxide devices at different annealing temperatures.[158] (b) *I*–*V* characteristic curves for as-deposited, inter-diffused (773 K) and crystallized (973 K) devices.[198] (c) *I*–*V* characteristic curves obtained from measurements (solid line) and calculations (dashed line) at different ambient temperatures.[169] (d) Calculated *I*–*V* characteristic curves at different ambient temperatures.[182] (e) Variation of the *I*–*V* characteristic curve with device temperature. (f) Variation of pulse oscillation with temperature.[199]

the memristor, the parameters of other auxiliary electronic components are also key elements that can affect the performance of the circuit. For example, as shown in Fig. 15(b) and (c), by adjusting the size of the shunt resistance and device capacitance, different NDR characteristic curves are obtained. As the shunt resistance increases, the on-start current I_{on} decreases (leakage current decreases), and as the device capacitance increases, the device exhibits a multi-slope NDR effect, which plays an important role in oscillator circuits.[198] In the absence of an external shunt capacitor, the parasitic capacitance of the device is usually considered small. As shown in Fig. 15(g), the *I–V* characteristics of the device were measured with different capacities of capacitors connected in parallel; the parts with different slopes are marked in various colors, with the blue line indicating the case without parallel capacitors. By comparison, the effect on the different slope regions can be better observed by the change in capacitance value. The different slopes also correspond to a change in the oscillatory characteristics, and the period of the oscillations usually increases with an increase in capacitance.[201]

In a memristor, device performance depends not only on the functional layer alone but also on the interfacial effects between the electrodes and the functional layer, adsorption of oxygen, and so on.[4,203] As shown in Fig. 15(d) and (e),[156] the SB-NDR region appears as the bottom electrode size increases, but the electrode size has little effect on the current density of the annealed device. In addition, the level of thermal conductivity of the metal electrodes affects the performance. For example, when high thermal conductivity gold is replaced by platinum, the threshold voltage and current undergo a decrease while increasing the thickness of the electrode; the threshold voltage and current undergo a general increase, as shown in Fig. 15(f). The effect of thickness is also due to its impact on heat transfer. It has been shown that electrode materials with higher thermal conductivity can increase the electroforming voltage, the threshold switching voltage, and the threshold switching power of the device.[202]

4.4 Recent progress of NDR for niobium oxide memristors

4.4.1 Steady states. Steady state analysis of memristors has been a hot research topic because it is the basis for con-

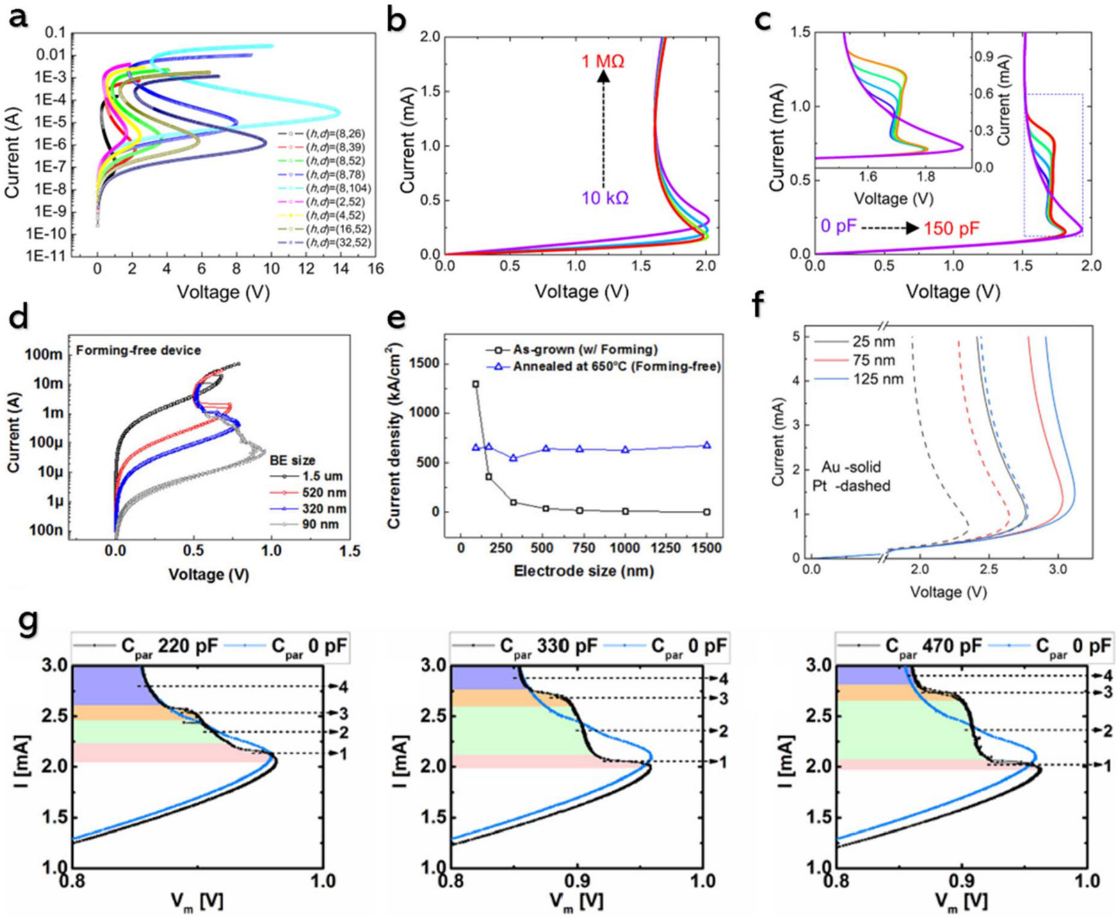

Fig. 15 (a) *I–V* characteristic curves corresponding to devices of different sizes (unit: nm).[182] (b) Effect of shunt resistance on quasi-static NDR characteristics. (c) Effect of device capacitance on quasi-static NDR characteristics.[198] (d) Effect of different bottom electrode sizes on NDR characteristics. (e) Effect of electrode area on current density after annealing and as-grown devices.[156] (f) Effect of different sizes of gold and platinum electrodes on the NDR characteristics of devices.[202] (g) Effect of high and low values of shunt capacitance on device NDR characteristics.[201]

structing oscillating circuits.[204–207] Wright *et al.* conducted a steady-state analysis of the dynamic neuro-resistor model, which is based on the original phenomenological model of the NbO_2 Mott memristor. The authors give three numerical examples of dynamic neural resistors in addition to steady-state analysis. Periodic output voltage spikes can be generated in response to DC or voltage inputs by alternating the threshold switching of the memristor. The turn-on voltage of the threshold switch corresponds to the inflection point at which the NDR starts, and the turn-off voltage of the threshold switch corresponds to the inflection point at which the NDR ends.[191]

Recently, in a study of the response of memristors to AC signals, a fading memory effect was proposed by some researchers.[208–212] For example, Messaris *et al.*[172] found that the NbO_2 memristor can exhibit two different steady-state responses when stimulated with sinusoidal current inputs of appropriate amplitude at sufficiently high input frequencies. The generation of bi-stability is related to the local fading memory effect. When a sinusoidal current is input, the device maintains a single steady-state response for each output frequency until the frequency increases to a threshold value, where the device transitions to bi-stability. The device's two steady state transitions and volatile threshold switching properties can be used in sensors to create a new generation of artificial senses.[172]

4.4.2 Application of oscillating circuits. Due to the negative differential resistance region, the memristor can oscillate in response to pulsed signals. Oscillation occurs only when the conductance of the nonlinear element (memristor) in the circuit is within the NDR region.[213] Based on the conception of bionics, memristor neuron circuits can be made to have simpler circuit compositions than CMOS. By adjusting the resistance value of the ECRAM in the oscillation circuit, various pulse modes can be achieved without requiring modifications to the circuit structure or the replacement of electronic components.[214] In an oscillation circuit, the period of the pulse is mainly determined by the magnitude of the DC voltage,[215–217] the load resistance and the parallel capacitor,[8,214] while the response time and attenuation time of the pulse are closely related to the resistance-switching characteristics of the memristor in the pulse circuit.[114] Oscillation circuits have various structural models, and each model can simulate various pulse characteristics. For example, the Hodgkin–Huxley (H–H) model consisting of local active memristors (LAMs) can be used to simulate most types of neuronal action potentials.[218–220] Apart from the H–H model, there is another simpler oscillation circuit model called the leaky integrate and fire (LIF) model.[115,221] This model involves connecting a memristor in parallel with a capacitor and then in series with a load resistor. To make the LIF circuit oscillate, the memristor must have good volatile switching characteristics, and the resistance value of the load resistor must be much greater than the low-resistance state of the memristor, and much less than the high-resistance state of the memristor.[221] Simultaneously, the parallel capacitor must maintain a continuous voltage that varies much more slowly than the current during resistance switching.[114]

Recently, Liang *et al.* designed a fully current-controlled memristor-based oscillator composed of two current-controlled (CC) locally active memristors. As shown in Fig. 16(a) and (b), by observing the static characteristics of the circuit under a DC scan and setting the bias current, the desired value of the boundary current in the NDR region can be obtained. Specific conditions are required for stable oscillations in the device, which are correlated with the current value I_D of the DC source. Fig. 16(c) shows the Jacobian matrix eigenvalues in the range $I_L \leq I_D \leq I_H$. When the current value of the DC source (I_D) is less than the first oscillating current, I_{osc1}, the oscillating waveform is in gradual convergence, as shown in Fig. 16(d)[222] and in the upper panel of Fig. 16(g).[223] A stable oscillating waveform is produced when I_D is greater than I_{osc1}, as shown in the lower half panel of Fig. 16(g). The migration trajectories of Poles s_{p12} of the equivalent impedance function $Z(s, Q)$ of the small-signal model of the oscillator are shown in Fig. 16(e). Current values near the sub critical Hopf bifurcation point may produce stable periodic oscillations, while a large value of current can break the stability of the neural circuit. Hopf bifurcation is the point at which self-excited oscillations begin or end from equilibrium when a parameter exceeds a critical value. By modulating the pulse width, or the period of the input periodic square wave, it is possible to achieve single-peak, double-peak, and more-peak biphasic action potentials in a single pulse period, as shown in Fig. 16(f). These studies provide a theoretical basis for the application of LAMs in oscillatory neural networks.[222]

4.4.3 Neural networks for bionic applications. In 2013, Pickett *et al.* proposed building neuronal circuits with two niobium oxide memristors, with all-or-none spikes for signal gain, and different period spikes.[128] Since then, researchers have conducted a series of bionic experiments with niobium oxide neuron circuits, such as simulating touch,[7,200,224] vision (image recognition),[8,217,225,226] and hearing.[6,227,228]

Biomimetic neuron devices with third-order dynamics (time derivative of voltage, substrate temperature and memristor temperature) can simulate three complex neuronal behaviors, spiking nociception, and spatiotemporal multimodal messaging, as shown in Fig. 17(a). Kim *et al.* prepared Ti/NbO_x/Pt Mott neuron arrays on flexible polyimide (PI) and silicon substrates, as shown in Fig. 17(b). Fig. 17(c) depicts the neural array, which integrates both spatial and temporal thermal information through inter-device heat conduction mechanisms. The two devices exhibited different NDR behaviors, as shown in Fig. 17(d). Different substrates have different thermal properties that can affect temperature transfer attenuation and conductivity. Fig. 17(e) shows the input voltages in word lines V_w and V_{th} of the device, which show the spatiotemporal integration behaviors during the standby period (P1), the increased frequency in P2 is due to the increased temperature, and the decrease in oscillation frequency is due to the inactivation of adjacent neurons occur-

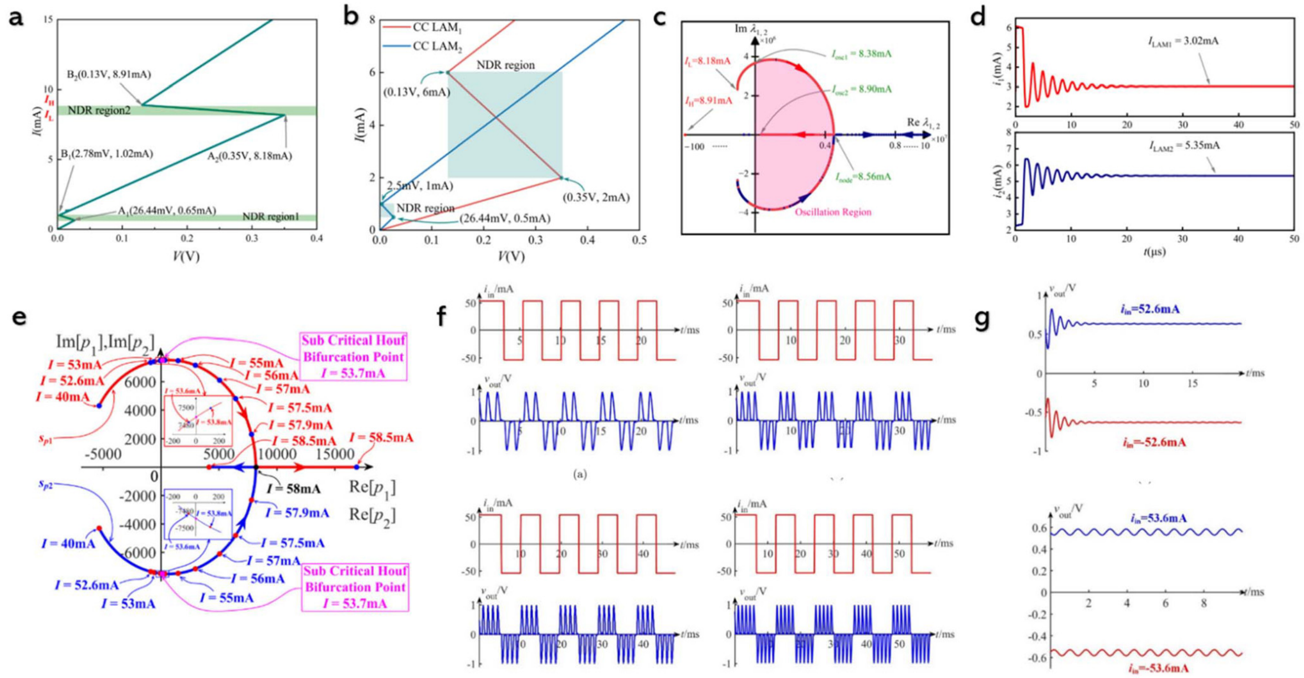

Fig. 16 (a) Fully CC-LAM-based oscillator. (b) *IV* curves of different CC LAM. (c) Jacobian matrix eigenvalues in the range $I_L \le I_D \le I_H$. (d) Simulation results of the oscillator at I_D = 8.37 mA.[222] (e) Migration trajectories of Poles s_{p12} of $Z(s, Q)$. (f) Biphasic action potentials are generated by the neuron circuit. (g) Stationary state at ±52.6 mA input DC and two symmetrical self-sustained oscillation waveforms at an input DC of ±53.6 mA.[223]

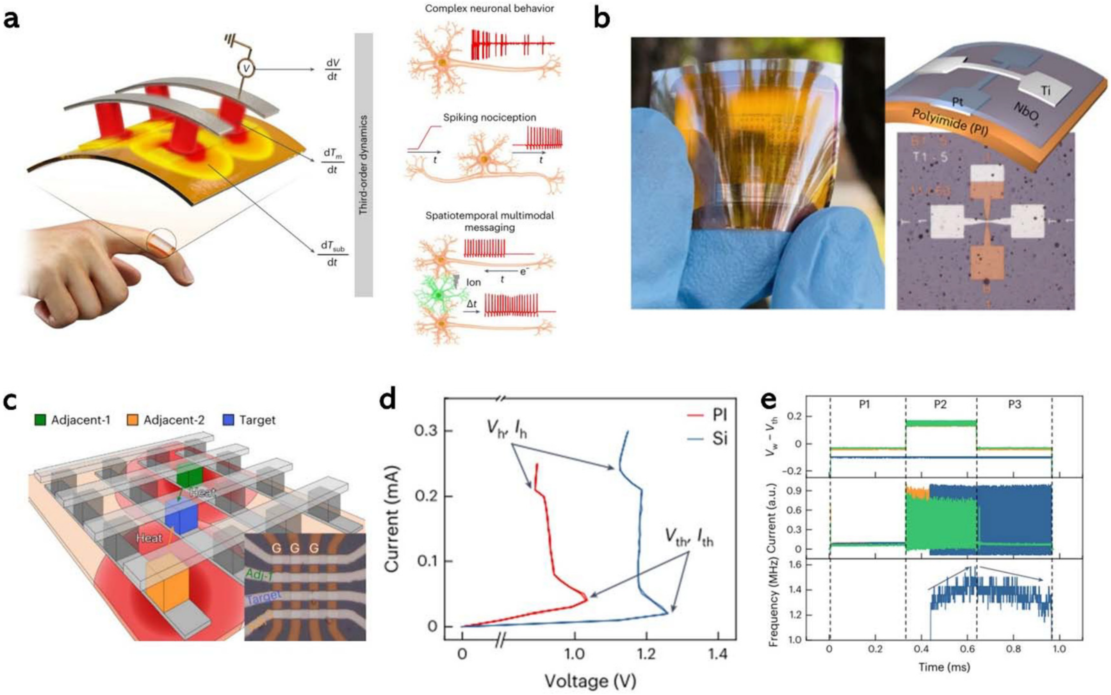

Fig. 17 (a) Schematic representation of a flexible bionic neuron and three complex neuronal behaviors that this bionic neuron can simulate. (b) Model and optical image of the Mott neuron. (c) Schematic of the neuron array. (d) NDR curves of the Mott neuron integrated on different substrates. (e) Oscillatory response of neighboring and target neurons with frequency.[129]

ring in P3. Such devices, which exploit natural thermal processes in computing, enable functionally dense, energy-efficient and new hybrid physical computing primitives.[129]

Image recognition has been an important direction of application for niobium oxide memristor neural networks.[229] Lu *et al.* utilized a locally responsive Nb_2O_5 memristor, incorporating parasitic capacitance, as a Leaky Integrate-and-Fire (LIF) neuronal model. They investigated the potential for inducing spiking oscillations in this neuron by employing small-signal equivalent circuitry analysis and exploring Hopf bifurcation dynamics. Fig. 18(a) and (b) show the voltage-current characteristics of the memristor in different scanning modes, and the experimental results are in good agreement with the simulation results. As shown in Fig. 18(c) and (d), when the voltage across the device reaches a threshold voltage, the capacitor discharges and the neuron sends out an output spike, changing the width of the pulse and the number of pulses. This demonstrated that a memristor neuron can achieve pulse modulation, which further mimics the behavior of the neuro-morphology. The circuit construction of a neural network of a memristor usually consists of three parts (Fig. 18(e)): the first part is used to read the input voltage signal, the second part is Neurons, and the third part is lateral inhibition, which is used to filter the neurons that are first to reach the threshold voltage of the NMOS, *i.e.* to achieve the "winner-take-all". As shown in Fig. 18(f), the fundamental process that achieves the recognition function of the memristor neural network is the modulation of the conductance values instead of the weights in deep learning through the signals input from the word line, such as the input vector corresponding to H (high voltage indicates 1, low voltage indicates 0). Each device in the memristor array changes its resistance state and rearranges itself to correspond to the input pattern. The image recognition neural network built by a memristor exhibits low power consumption and high time efficiency, which has potential applications in neuromorphic computing.[230]

Furthermore, image recognition can be used for artificial visual neurons, thus offering the potential for highly efficient neuromorphic vision systems.[226] Li *et al.* constructed an artificial visual pulse neuron by integrating NbO_x memristor and In_2O_3 phototransistor, each with time-dependent neuronal and synaptic functions, to encode rate and time-to-first-spike (TTFS) for visual information. Multiplexed rate and temporal fusion coding achieve excellent computational power and efficiency, demonstrating the possibility of developing efficient neuromorphic hardware. Fig. 19(a) shows the framework of the artificial visual pulse neuron. Fig. 19(b) and (c) show the memory output pulse current waveforms under different optical environments. The artificial neuron offers an expedited spike latency encoding range spanning from 13.00 μs down to 1.04 μs, along with an adjustable firing frequency encoding that can be tuned between 0.35 MHz and 1.85 MHz. It further distinguishes itself with minimal energy expenditure of merely 1.06 nJ per spike, exceptional endurance exceeding 10^{10} cycles, and the capability to encode information in a multiplexed fashion. As shown in Fig. 19(d), the rate and time fusion coding (RTF) of the external visual information is fed into the

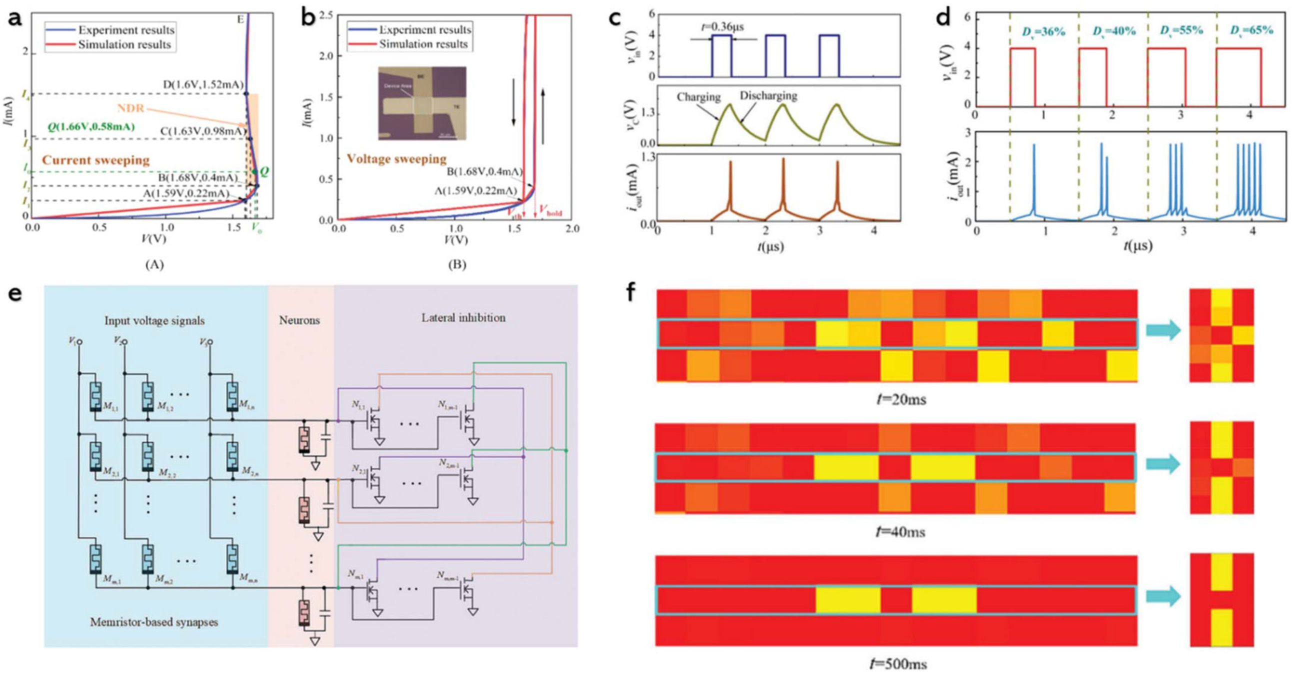

Fig. 18 (a) Current sweep *I*–*V* plot. (b) Voltage sweep *I*–*V* plot. (c) Neuromorphic behaviors under the 0.36 μs voltage pulse. (d) Neuromorphic behaviors under different input pulse widths. (e) Circuit construction of memristor neuron networks. (f) Change in the resistance value of the synaptic array of the memristor after the input of "H" (which constitutes the input vector using high and low levels of voltage).[230]

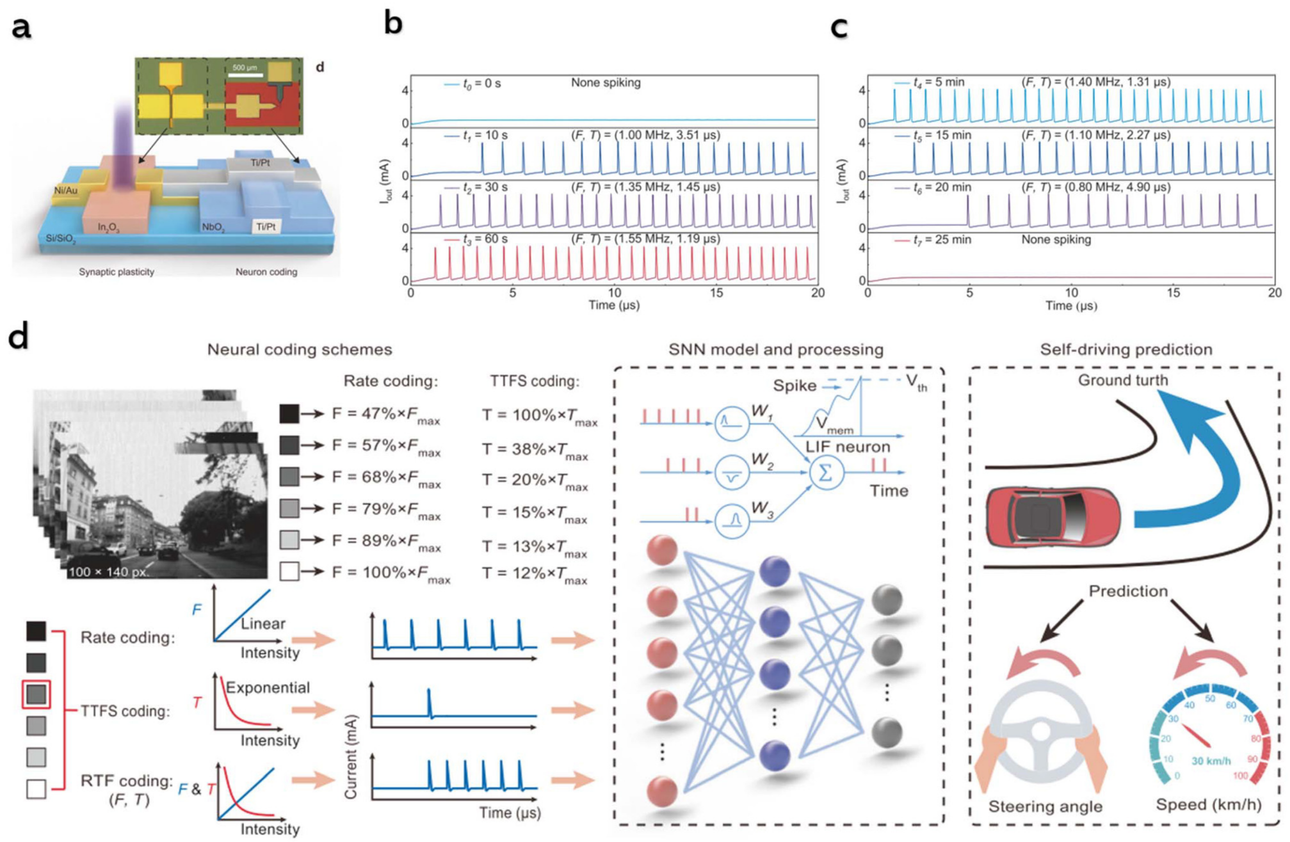

Fig. 19 (a) Schematic and optical images of an artificial neuron. (b) Memory output pulse current waveforms with increased synaptic weights after UV irradiation. (c) Memory output pulse current waveforms with reduced synaptic weights after light pulses. (d) Gray-scale images are encoded into multiple series of spike trains through rate coding, TTFS coding, and RTF coding schemes and fed into a trained SNN to predict vehicle speed and steering angle.[225]

trained signal-to-noise network, which has an efficient processing speed for external signals and provides the hardware possibility of neuro-morphism for high-precision steering and speed prediction of self-driving vehicles.[225]

Recently, FitzHugh–Nagumo (FN) circuits using NDR memristors based on FitzHugh–Nagumo and FitzHugh–Rinzel models have been proven reliable in building a neuromorphic hardware system.[231–233] In 2019, Boriskov *et al.* fabricated FN circuits using NbO_2 switches with stable NDR. The FitzHugh–Nagumo model is the first simplification of the Hodgkin–Huxley model. The FN model allows for the modeling of self-excitation and restoration of the membrane potential through positive and negative feedback, thus describing the electrical activity of the neuron. The FN circuit design is comparable to a tunnel diode; the only difference is that the inductance is connected in series to the FN circuit. The presence of inductance in the series is essential to ensure the functioning of the FN circuit. This is possible only if the S-switch with stable NDR (NbO_2 switch) is connected to the circuit. Furthermore, NbO_2 demonstrates stable electrical switching up to ~300 °C, which makes NbO_2 promising for applications in neuroelectronics, thermal oscillators and brain–machine interface neurodynamic models.[234,235]

In general, the significance of the negative differential in memristors is often underestimated, yet it is indispensable. In oscillator circuits, the memristor provides negative feedback in the negative differential region. The circuit oscillates only when the device conductance resides in the negative differential resistance region, which is influenced by device conductivity. The oscillating current and voltage signals are fundamental for spiking neural networks, amplifiers, high frequency oscillators, and high-speed switches. Therefore, negative differential resistance plays a crucial role in device performance and application scenarios. For example, in Terahertz Metamaterial Absorbers, the NDR effect induced by applying voltage to an n-type GaAs leads the device to function in the electron accumulation domain mode, thereby affecting device performance.[236]

5. Conclusion

In this review, we comprehensively introduced the history of the discovery, study and application of NDR effects, particularly in niobium oxide memristors. We underscore that NDR effects in niobium oxide memristors are primarily driven by mechanisms such as the Mott metal–insulator transition (MIT), Peierls transition, and electrically induced nonlinear conduction mechanisms such as the Poole–Frenkel effect and small polaron conduction. By fine-tuning NDR characteristics, memristor performance can be substantially improved, paving the way for applications in neuronal circuits and neural networks. These advancements, combined with signal processing technologies such as neural network algorithms and deep learning, enable a range of functionalities, including pulse signal regulation, image recognition, bionic synapses, memory-computing integration, and sensory capabilities.

Despite these promising developments, a comprehensive understanding of the synergistic interactions among various NDR mechanisms remains lacking, along with clarity of their respective roles and contributions to the overall NDR effect. Additionally, the challenge of controlling the oxygen content in niobium oxide complicates phase consistency, impacting reproducibility and uniformity in NDR effects. Although the S-type NDR has significant potential, its practical applications remain largely unexplored. Recent progress in developing reliable and efficient oscillation circuits based on NDR effects has led to potential applications in pulse neural networks, including advanced fields such as logic circuits, wireless communications, and neural network architectures.

Looking ahead, the application of NDR in memristors offers exciting avenues for next-generation computing technologies. Future studies could focus on enhancing control over NDR behavior to enable its integration in complex neuromorphic systems, ultimately mimicking brain-like synaptic responses with high energy efficiency. By tailoring the NDR response, memristors may be further adapted for adaptive learning systems and dynamic signal processing, opening the door to more sophisticated edge computing and real-time data processing applications. Moreover, NDR-based memristors can contribute to reconfigurable logic circuits that respond to varying input conditions, enhancing the flexibility and functionality of electronic devices.

Additionally, the exploration of hybrid NDR effects could lead to multi-functional memristor architectures capable of handling both storage and processing tasks, crucial for in-memory computing systems that reduce data transfer bottlenecks. Advances in material engineering to stabilize oxygen content and phase uniformity in niobium oxide could significantly improve the consistency and scalability of NDR devices, making them viable for mass production and commercial applications. As research progresses, NDR-enabled memristors can redefine the landscape of high-speed computing, AI hardware, and adaptable sensor networks, positioning them as foundational technologies for future electronics.

Author contributions

Hongyi Lu: writing – original draft, conceptualization, investigation, formal analysis, data curation. Shiyu Xie: writing – original draft, conceptualization, investigation. Weijian Zhang: writing – review & editing, formal analysis, validation. Yue Chen: writing – review & editing, conceptualization, supervision. Jianming Tao: writing – review & editing. Chinmayee Mandar Mhaskar: writing – review & editing. Ayan Roy Chaudhuri: writing – review & editing, funding acquisition. Yingbin Lin: writing – review & editing. Jiaxin Li: writing – review & editing. Sanjay Mathur: writing – review & editing, funding acquisition. Zhigao Huang: writing – review & editing, funding acquisition.

Conflicts of interest

The authors declare that they have no known competing financial interests or personal relationships that could have appeared to influence the work reported in this paper.

Data availability

No primary research results, software or code has been included and no new data were generated or analysed as part of this review.

Acknowledgements

The authors acknowledge the financial support by the National Natural Science Foundation of China (No. 62474041 and 52403294); the Natural Science Foundation of the Fujian Province (2023J01521); Key Research and Industrialization Projects of Technological Innovation in Fujian Province (2023XQ010); Fujian Province Technology Innovation Key Research and Industrialization Projects (2024XQ007); Foreign Science and Technology Cooperation Project of Fuzhou Science and Technology Bureau (No. 2024-Y-006); SPARC, Ministry of Education, Government of India (Letter No. SPARC/2024-2025/SEMI/P3099); and Program of China Scholarship Council (Grant No. 202508350013).

References

1 X. Wu, V. Saxena, K. Zhu and S. Balagopal, A CMOS Spiking Neuron for Brain-Inspired Neural Networks with Resistive Synapses and in Situ Learning, *IEEE Trans. Circuits Syst.*, 2015, **62**, 1088–1092, DOI: **10.1109/TCSII.2015.2456372**.

2 M. Ishii, S. Kim, S. Lewis, A. Okazaki, J. Okazawa and M. Itol, On-Chip Trainable 1.4M 6T2R PCM Synaptic Array with 1.6K Stochastic LIF Neurons for Spiking RBM, in *2019 IEEE Int. Electron Devices Meet, IEEE*, 2019, pp. 14.2.1–14.2.4, DOI: **10.1109/IEDM19573.2019.8993466**.

3 G. Indiveri, B. Linares-Barranco, T. J. Hamilton, A. van Schaik, R. Etienne-Cummings, T. Delbruck, S.-C. Liu, P. Dudek, P. Häfliger, S. Renaud, J. Schemmel, G. Cauwenberghs, J. Arthur, K. Hynna, F. Folowosele,

S. Saighi, T. Serrano-Gotarredona, J. Wijekoon, Y. Wang and K. Boahen, Neuromorphic Silicon Neuron Circuits, *Front. Neurosci.*, 2011, **5**, 73, DOI: 10.3389/fnins.2011.00073.

4 M. K. Song, J. H. Kang, X. Zhang, W. Ji, A. Ascoli, I. Messaris, A. S. Demirkol, B. Dong, S. Aggarwal, W. Wan, S. M. Hong, S. G. Cardwell, I. Boybat, J. S. Seo, J. S. Lee, M. Lanza, H. Yeon, M. Onen, J. Li, B. Yildiz, J. A. del Alamo, S. Kim, S. Choi, G. Milano, C. Ricciardi, L. Alff, Y. Chai, Z. Wang, H. Bhaskaran, M. C. Hersam, D. Strukov, H. S. P. Wong, I. Valov, B. Gao, H. Wu, R. Tetzlaff, A. Sebastian, W. Lu, L. Chua, J. J. Yang and J. Kim, Recent Advances and Future Prospects for Memristive Materials, Devices, and Systems, *ACS Nano*, 2023, **17**, 11994–12039, DOI: 10.1021/acsnano.3c03505.

5 W. Zhang, P. Yao, B. Gao, Q. Liu, D. Wu, Q. Zhang, Y. Li, Q. Qin, J. Li, Z. Zhu, Y. Cai, D. Wu, J. Tang, H. Qian, Y. Wang and H. Wu, Edge learning using a fully integrated neuro-inspired memristor chip, *Science*, 2023, **381**, 1205–1211, DOI: 10.1126/science.ade3483.

6 J. Yu, F. Zeng, Q. Wan, Z. Lu and F. Pan, Emulation of auditory senses depending on chaotic dynamics of threshold switching memristor, *InfoMat*, 2023, **5**, 1–11, DOI: 10.1002/inf2.12458.

7 X. Zhang, Y. Zhuo, Q. Luo, Z. Wu, R. Midya, Z. Wang, W. Song, R. Wang, N. K. Upadhyay, Y. Fang, F. Kiani, M. Rao, Y. Yang, Q. Xia, Q. Liu, M. Liu and J. J. Yang, An artificial spiking afferent nerve based on Mott memristors for neurorobotics, *Nat. Commun.*, 2020, **11**, 51, DOI: 10.1038/s41467-019-13827-6.

8 Q. Duan, Z. Jing, X. Zou, Y. Wang, K. Yang, T. Zhang, S. Wu, R. Huang and Y. Yang, Spiking neurons with spatiotemporal dynamics and gain modulation for monolithically integrated memristive neural networks, *Nat. Commun.*, 2020, **11**, 3399, DOI: 10.1038/s41467-020-17215-3.

9 M. Dragoman and D. Dragoman, Negative differential resistance in novel nanoscale devices, *Solid-State Electron.*, 2022, **197**, 108464, DOI: 10.1016/j.sse.2022.108464.

10 D. Dragoman and M. Dragoman, Enhanced architectures for room-temperature reversible logic gates in graphene, *Appl. Phys. Lett.*, 2014, **105**, 113109, DOI: 10.1063/1.4896140.

11 M. Dragoman, A. Dinescu and D. Dragoman, Wafer-Scale Fabrication and Room-Temperature Experiments on Graphene-Based Gates for Quantum Computation, *IEEE Trans. Nanotechnol.*, 2018, **17**, 362–367, DOI: 10.1109/TNANO.2018.2803079.

12 Y. Li, Z. Wang, R. Midya, Q. Xia and J. J. Yang, Review of memristor devices in neuromorphic computing: materials sciences and device challenges, *J. Phys. D:Appl. Phys.*, 2018, **51**, 503002, DOI: 10.1088/1361-6463/aade3f.

13 B. K. Ridley, Negative Differential Resistance: A Brief History and Review. Boston, MA: Springer US, 1993, pp. 1–21, DOI: 10.1007/978-1-4615-2822-7_1.

14 R. A. Pucel, Theory of the Esaki diode frequency converter, *Solid-State Electron.*, 1961, **3**, 167–207, DOI: 10.1016/0038-1101(61)90002-8.

15 W. T. Read, A proposed high-frequency, negative-resistance diode, *Bell Syst. Tech. J.*, 1958, **37**, 401–446, DOI: 10.1002/j.1538-7305.1958.tb01527.x.

16 B. C. Salamov, S. Büyükakkaş, M. Özer and K. Çolakoğlu, Behaviour of current in gas discharge system between parallel-plane electrodes, *EPJ Appl. Phys.*, 1998, **2**, 275–279, DOI: 10.1051/epjap:1998193.

17 E. Lozneanu, V. Popescu and M. Sanduloviciu, Negative differential resistance related to self-organization phenomena in a dc gas discharge, *J. Appl. Phys.*, 2002, **92**, 1195–1199, DOI: 10.1063/1.1490156.

18 Y. A. Astrov, A. N. Lodygin, L. M. Portsel and E. V. Beregulin, Comparative study of noise in low-current Townsend discharge in nitrogen and argon, *Phys. Rev. E*, 2017, **95**, 1–7, DOI: 10.1103/PhysRevE.95.043206.

19 P. Fantini, N. Polino, A. Ghetti and D. Ielmini, Threshold Switching by Bipolar Avalanche Multiplication in Ovonic Chalcogenide Glasses, *Adv. Electron. Mater.*, 2023, **9**, 1–8, DOI: 10.1002/aelm.202300037.

20 K. Kobashi, R. Hayakawa, T. Chikyow and Y. Wakayama, Negative Differential Resistance Transistor with Organic p–n Heterojunction, *Adv. Electron. Mater.*, 2017, **3**, 1700106, DOI: 10.1002/aelm.201700106.

21 A. Fischer, P. Pahner, B. Lüssem, K. Leo, R. Scholz, T. Koprucki, K. Gärtner and A. Glitzky, Self-heating, bistability, and thermal switching in organic semiconductors, *Phys. Rev. Lett.*, 2013, **110**, 1–5, DOI: 10.1103/PhysRevLett.110.126601.

22 S. Biswas, M. Dutta and M. A. Stroscio, Negative differential resistance in conductive polymer and semiconducting quantum dot nanocomposite systems, *Appl. Phys. Lett.*, 2009, **95**, 182102, DOI: 10.1063/1.3258350.

23 A. Ascoli, S. Slesazeck, H. Mähne, R. Tetzlaff and T. Mikolajick, Nonlinear Dynamics of a Locally-Active Memristor, *IEEE Trans. Circuits Syst. I: Regul. Pap.*, 2015, **62**, 1165–1174, DOI: 10.1109/TCSI.2015.2413152.

24 J. Bisquert, R. Fenollosa, A. Cordero and J. R. Torregrosa, Bifurcation and Frequency Properties of S-Type Neuronic Oscillators, *J. Phys. Chem. Lett.*, 2025, **16**, 3616–3631, DOI: 10.1021/acs.jpclett.5c00288.

25 B. Bowers, Wireless: From Marconi's Black Box to the Audion (review), *Technol. Cult.*, 2003, **44**, 398–399, DOI: 10.1353/tech.2003.0056.

26 A. W. Hull, The Dynatron: A Vacuum Tube Possessing Negative Electric Resistance, *Proc. IRE*, 1918, **6**, 5–35, DOI: 10.1109/JRPROC.1918.217353.

27 O. V. Lossev, CII. Luminous carborundum detector and detection effect and oscillations with crystals, *London, Edinburgh Dublin Philos. Mag. J. Sci.*, 1928, **6**, 1024–1044, DOI: 10.1080/14786441108564683.

28 F. E. Terman, R. R. Buss, W. R. Hewlett and F. C. Cahill, Some Applications of Negative Feedback with Particular Reference to Laboratory Equipment, *Proc. IRE*, 1939, **27**, 649–655, DOI: 10.1109/JRPROC.1939.228752.

29 C. Brunetti, A practical negative resistance oscillator, *Rev. Sci. Instrum.*, 1939, **10**, 85–88, DOI: 10.1063/1.1751492.

30 W. C. Hahn and G. F. Metcalf, Velocity-Modulated Tubes, *Proc. IRE*, 1939, **27**, 106–116, DOI: **10.1109/JRPROC.1939.229013**.

31 W. N. Tuttle, Bridged-T and Parallel-T Null Circuits for Measurements at Radio Frequencies, *Proc. IRE*, 1940, **28**, 23–29, DOI: **10.1109/JRPROC.1940.228817**.

32 E. J. Ryder, Mobility of holes and electrons in high electric fields, *Phys. Rev.*, 1953, **90**, 766–769, DOI: **10.1103/PhysRev.90.766**.

33 H. Krömer, Zur Theorie des Germaniumgleichrichters und des Transistors, *Z. Phys.*, 1953, **134**, 435–450, DOI: **10.1007/BF01332747**.

34 H. Krömer, Proposed Negative-Mass Microwave Amplifier, *Phys. Rev.*, 1958, **109**, 1856, DOI: **10.1103/PhysRev.109.1856**.

35 W. Shockley, Negative resistance arising from transit time in semiconductor diodes, *Bell Syst. Tech. J.*, 1954, **33**, 799–826, DOI: **10.1002/j.1538-7305.1954.tb03742.x**.

36 L. Esaki, New phenomenon in narrow germanium p-n junctions, *Phys. Rev.*, 1958, **109**, 603–604, DOI: **10.1103/PhysRev.109.603**.

37 M. E. Hines, High-Frequency Negative-Resistance Circuit Principles for Esaki Diode Applications, *Bell Syst. Tech. J.*, 1960, **39**, 477–513, DOI: **10.1002/j.1538-7305.1960.tb03933.x**.

38 B. K. Ridley and T. B. Watkins, The possibility of negative resistance effects in semiconductors, *Proc. Phys. Soc.*, 1961, **78**, 293–304, DOI: **10.1088/0370-1328/78/2/315**.

39 T. W. Hickmott, Low-frequency negative resistance in thin anodic oxide films, *J. Appl. Phys.*, 1962, **33**, 2669–2682, DOI: **10.1063/1.1702530**.

40 J. Voelcker, The Gunn effect, *IEEE Spectrum*, 1989, **26**, 24, DOI: **10.1109/6.29344**.

41 J. A. Copeland, A new mode of operation for bulk negative resistance oscillators, *Proc. IEEE*, 1966, **54**, 1479–1480, DOI: **10.1109/PROC.1966.5158**.

42 C. N. Berglund, Thermal Filaments in Vanadium Dioxide, *IEEE Trans. Electron Devices*, 1969, **16**, 432–437, DOI: **10.1109/T-ED.1969.16773**.

43 C. N. Berglund and R. H. Walden, A Thin-Film Inductance Using Thermal Filaments, *IEEE Int. Electron Devices*, 1970, **17**, 137–148, DOI: **10.1109/T-ED.1970.16939**.

44 C. N. Berglund and N. Klein, Thermal Effects on Switching of Solids from an Insulating to a Conductive State, *Proc. IEEE*, 1971, **59**, 1099–1110, DOI: **10.1109/PROC.1971.8337**.

45 B. D. H. Tellegen, Stability of negative resistances, *Int. J. Electron.*, 1972, **32**, 681–686, DOI: **10.1080/00207217208938331**.

46 J. G. Simmons and R. R. Verderber, New conduction and reversible memory phenomena in thin insulating films, *Proc. R. Soc. London, Ser. A*, 1967, **301**, 77–102, DOI: **10.1098/rspa.1967.0191**.

47 N. F. Mott, Metal-Insulator Transitions, *Rev. Mod. Phys.*, 1968, **40**, 677–683, DOI: **10.1351/pac198052010065**.

48 G. Dearnaley, A. M. Stoneham and D. V. Morgan, Electrical phenomena in amorphous oxide films, *Rep. Prog. Phys.*, 1970, **33**, 1129–1191, DOI: **10.1088/0034-4885/33/3/306**.

49 P. R. Berger and A. Ramesh, Negative Differential Resistance Devices and Circuits, in *Compr. Semicond. Sci. Technol*, Elsevier, 2011, pp. 176–241. DOI: **10.1016/B978-0-44-453153-7.00013-4**.

50 N. Alain, Negative Differential Conductance Materials for Flexible Electronics, *J. Appl. Polym. Sci.*, 2014, **131**, 40169, DOI: **10.1002/app.41233**.

51 M. N. A. R. Al-Mudares and B. K. Ridley, Monte carlo simulation of scattering-induced negative differential resistance in algaas/gaas quantum wells, *J. Phys. C:Solid State Phys.*, 1986, **19**, 3179–3192, DOI: **10.1088/0022-3719/19/17/014**.

52 M. M. Glazov and E. L. Ivchenko, Electron-electron scattering effect on spin relaxation in multi-valley nanostructures, *EPL*, 2009, **87**, 57005, DOI: **10.1209/0295-5075/87/57005**.

53 B. K. Ridley, On the effect of plasmon-phonon coupling and phonon reabsorption on scattering-induced NDR, *Superlattices Microstruct.*, 1986, **2**, 159–164, DOI: **10.1016/0749-6036(86)90081-9**.

54 Y. Zhao, Z. Wan, U. Hetmanuik and M. P. Anantram, Negative Differential Resistance in Graphene Boron Nitride Heterostructure Controlled by Twist and Phonon-Scattering, *IEEE Electron Device Lett.*, 2016, **37**, 1242–1245, DOI: **10.1109/LED.2016.2595522**.

55 D. Li, J. Shao, L. Tang, C. Edmunds, G. Gardner, M. J. Manfra and O. Malis, Temperature-dependence of negative differential resistance in GaN/AlGaN resonant tunneling structures, *Semicond. Sci. Technol.*, 2013, **28**, 074024, DOI: **10.1088/0268-1242/28/7/074024**.

56 M. P. Vaughan and B. K. Ridley, Effect of non-parabolicity on the density of states for high-field mobility calculations in dilute nitrides, *Phys. Status Solidi C*, 2007, **4**, 686–688, DOI: **10.1002/pssc.200673342**.

57 D. L. Woolard, H. Tian, M. A. Littlejohn, R. J. Trew and K. W. Kim, Impact of k-space transfer and band nonparabolicity on electron transport in a GaAs ballistic diode, *Semicond. Sci. Technol.*, 1992, **7**, B354–B356, DOI: **10.1088/0268-1242/7/3B/091**.

58 R. G. van Welzenis and B. K. Ridley, On the properties of InSb quantum wells, *Solid-State Electron.*, 1984, **27**, 113–120, DOI: **10.1016/0038-1101(84)90101-1**.

59 J. Chen, M. A. Reed, A. M. Rawlett and J. M. Tour, Large on-off ratios and negative differential resistance in a molecular electronic device, *Science*, 1999, **286**, 1550–1552, DOI: **10.1126/science.286.5444.1550**.

60 J. Gaudioso, L. J. Lauhon and W. Ho, Vibrationally mediated negative differential resistance in a single molecule, *Phys. Rev. Lett.*, 2000, **85**, 1918–1921, DOI: **10.1103/PhysRevLett.85.1918**.

61 S. Sarkar, A. Pramanik and P. Sarkar, Quantum transport behavior of Ni-based dinuclear complexes in presence of zigzag graphene nanoribbon as electrode, *Chem. Phys.*, 2016, **478**, 173–177, DOI: **10.1016/j.chemphys.2016.03.012**.

62 S. H. Shin, T. Halpern and P. M. Raccah, High-speed high-current field switching of NbO_2, *J. Appl. Phys.*, 1977, **48**, 3150–3153, DOI: 10.1063/1.324047.

63 P. H. Bolivar, P. Leisching, K. Leo, J. Shah and K. Köhler, Observation of Bloch Oscillations in a Semiconductor Superlattice, *Opt. InfoBase Conf. Pap.*, 1993, **84**, 142–146, DOI: 10.1364/ueo.1993.d5.

64 T. Hartmann, F. Keck, H. J. Korsch and S. Mossmann, Dynamics of Bloch oscillations, *New J. Phys.*, 2004, **6**(2), DOI: 10.1088/1367-2630/6/1/002.

65 M. Ben Dahan, E. Peik, J. Reichel, Y. Castin and C. Salomon, Bloch oscillations of atoms in an optical potential, *Phys. Rev. Lett.*, 1996, **76**, 4508–4511, DOI: 10.1103/PhysRevLett.76.4508.

66 B. K. Ridley, W. J. Schaff and L. F. Eastman, Theory of the GaN crystal diode: Negative mass negative differential resistance, *J. Appl. Phys.*, 2005, **97**, 094503, DOI: 10.1063/1.1889235.

67 A. Dyson and B. K. Ridley, Negative-mass transport in semiconductor diodes, *Phys. Rev. B: Condens. Matter Mater. Phys.*, 2005, **72**, 193301, DOI: 10.1103/PhysRevB.72.193301.

68 D. Dragoman and M. Dragoman, Metamaterials for ballistic electrons, *J. Appl. Phys.*, 2007, **101**, 104316, DOI: 10.1063/1.2734876.

69 G. Chen, E. M. Gallo, O. D. Leaffer, T. McGuckin, P. Prete, N. Lovergine and J. E. Spanier, Tunable hot-electron transfer within a single core-shell nanowire, *Phys. Rev. Lett.*, 2011, **107**, 156802, DOI: 10.1103/PhysRevLett.107.156802.

70 C. L. Ho, M. C. Wu, W. J. Ho and J. W. Liaw, Light-induced negative differential resistance in planar InP/InGaAs/InP double-heterojunction p-i-n photodiode, *Appl. Phys. Lett.*, 1999, **74**, 4008–4010, DOI: 10.1063/1.123243.

71 J. S. Jung, E. H. Cho, S. Jo, K. H. Kim, D. H. Choi and J. Joo, Photo-induced negative differential resistance of organic thin film transistors using anthracene derivatives, *Org. Electron.*, 2013, **14**, 2204–2209, DOI: 10.1016/j.orgel.2013.05.019.

72 S. Mansouri, A. Jouili, L. E. Mir, A. A. Al-Ghamdi and F. Yakuphanoglu, Studies of photosensitivity and photo-induced negative differential resistance (NDR) of TIPS-pentacene-poly(3-hexyl)thiophene blend organic thin film transistor, *Synth. Met.*, 2015, **207**, 1–12, DOI: 10.1016/j.synthmet.2015.05.016.

73 W. Liu, H. Guo, W. Li, X. Wan, S. C. Bodepudi, K. Shehzad and Y. Xu, Light-induced negative differential resistance in gate-controlled graphene-silicon photodiode, *Appl. Phys. Lett.*, 2018, **112**, 201109, DOI: 10.1063/1.5026382.

74 K. W. Lee, C. W. Jang, D. H. Shin, J. M. Kim, S. S. Kang, D. H. Lee, S. Kim, S.-H. Choi and E. Hwang, Light-induced negative differential resistance in graphene/Si-quantum-dot tunneling diodes, *Sci. Rep.*, 2016, **6**, 30669, DOI: 10.1038/srep30669.

75 B. Jacob, J. Silva, J. M. L. Figueiredo, J. B. Nieder and B. Romeira, Light-induced negative differential resistance and neural oscillations in neuromorphic photonic semiconductor micropillar sensory neurons, *Sci. Rep.*, 2025, **15**, 6805, DOI: 10.1038/s41598-025-90265-z.

76 M. S. A. Zaslavsky, D. C. Tsui and M. Santos, Magnetotunneling in double-barrier heterostructures, *Phys. Rev. B: Condens. Matter Mater. Phys.*, 1989, **40**, 9829, DOI: 10.1103/PhysRevB.40.9829.

77 L. D. Macks, S. A. Brown, R. G. Clark, R. P. Starrett, M. A. Reed, M. R. Deshpande, C. J. L. Fernando and W. R. Frensley, Resonant tunneling in double-quantum-well triple-barrier heterostructures, *Phys. Rev. B: Condens. Matter Mater. Phys.*, 1996, **54**, 4857–4862, DOI: 10.1103/PhysRevB.54.4857.

78 R. Singh, Z. Luo, Z. Lu, A. S. Saleemi, C. Xiong and X. Zhang, Thermal stability of NDR-assisted anomalous Hall effect based magnetic device, *J. Appl. Phys.*, 2019, **125**, 203901, DOI: 10.1063/1.5088916.

79 M. D. Penrose, On a continuum percolation model, *Adv. Appl. Probab.*, 1991, **23**, 536–556, DOI: 10.2307/1427621.

80 J. W. Essam, Percolation theory, *Rep. Prog. Phys.*, 1980, **43**, 833–912, DOI: 10.1088/0034-4885/43/7/001.

81 Y. Song, H. Jeong, J. Jang, T. Y. Kim, D. Yoo, Y. Kim, H. Jeong and T. Lee, 1/f Noise Scaling Analysis in Unipolar-Type Organic Nanocomposite Resistive Memory, *ACS Nano*, 2015, **9**, 7697–7703, DOI: 10.1021/acsnano.5b03168.

82 P. Sharma, L. S. Bernard, A. Bazigos, A. Magrez and A. M. Ionescu, Graphene Negative Differential Resistance Circuit with Voltage-Tunable High Performance at Room Temperature, *IEEE Electron Device Lett.*, 2015, **36**, 865–867, DOI: 10.1109/LED.2015.2445858.

83 K. Liu, S. Y. T. Tzeng and Y. Tzeng, Two-level model of oscillating electric-field-induced current instability and chaos in n-GaAs, *J. Phys.: Condens. Matter*, 2007, **19**, 116208, DOI: 10.1088/0953-8984/19/11/116208.

84 J. Chen, L. Xu, J. Lin, Y. Geng, L. Wang and D. Ma, Negative differential resistance and multilevel memory effects in organic devices, *Semicond. Sci. Technol.*, 2006, **21**, 1121–1124, DOI: 10.1088/0268-1242/21/8/024.

85 T. J. Shieh, Computer analysis of the negative differential resistance switching phenomenon of double-injection devices, *IEEE Trans. Electron Devices*, 1989, **36**, 1787–1792, DOI: 10.1109/16.34244.

86 A. A. Akopyan and Z. S. Gribnikov, Double injection for weak heating of current carriers, *Solid-State Electron.*, 1976, **19**, 41–46, DOI: 10.1016/0038-1101(76)90131-3.

87 K. C. Kao, Double injection in solids with non-ohmic contacts. II. Solids with defects, *J. Phys. D:Appl. Phys.*, 1984, **17**, 1449–1467, DOI: 10.1088/0022-3727/17/7/018.

88 C.-F. Yang and J.-G. Hwu, Double Negative Differential Resistance Properties in MISIM Structure with Substrate Grounded and Two Electrode Terminals Biased with Constant Offset Voltage, *ECS Meet. Abstr.*, 2017, **MA2017-02**, 826–826, DOI: 10.1149/MA2017-02/14/826.

89 D. D. Smith, Grating-Induced Frequency Multiplication in Planar Gunn Diodes, in *2015 IEEE Compd. Semicond. Integr. Circuit Symp*, IEEE, 2015, pp. 1–4. DOI: 10.1109/CSICS.2015.7314505.

90 J. N. Baillargeon, K. Y. Cheng, J. Laskar and J. Kolodzey, Three-terminal delta-doped barrier switching device with S-shaped negative differential resistance, *Appl. Phys. Lett.*, 1989, **55**, 663–665, DOI: 10.1063/1.101815.

91 Y. Zheng and R. Lake, Self-consistent transit-time model for a resonant tunnel diode, *IEEE Trans. Electron Devices*, 2004, **51**, 535–541, DOI: 10.1109/TED.2004.824683.

92 E. Alekseev and D. Pavlidis, Large-signal microwave performance of GaN-based NDR diode oscillators, *Solid-State Electron.*, 2000, **44**, 941–947, DOI: 10.1016/S0038-1101(00)00011-3.

93 V. P. Kesan, D. P. Neikirk, B. G. Streetman, P. A. Blakey and T. D. Linton, The Influence of Transit-Time Effects on the Optimum Design and Maximum Oscillation Frequency of Quantum Well Oscillators, *IEEE Trans. Electron Devices*, 1988, **35**, 405–413, DOI: 10.1109/16.2472.

94 T. Harumoto, H. Fujiki, J. Shi, Y. Nakamura and Y. Sutou, Negative differential resistance based on phase transformation, *Mater. Horiz.*, 2023, **10**, 5143–5151, DOI: 10.1039/d3mh00657c.

95 T. Harumoto, H. Fujiki, Y. Sutou and J. Shi, Hydrogen gas sensing negative differential resistance device based on phase transformation of metal hydride, *Next Mater.*, 2025, **6**, 100298, DOI: 10.1016/j.nxmate.2024.100298.

96 F. D. Manchester and A. San-Martin, The H-Pd (Hydrogen-Palladium) System, *Phase Diagram Eval. Sect. II*, 1994, **15**(1), 62–83, DOI: 10.1007/BF02667685.

97 A. Pozio and S. Tosti, Pd-Ag electrical resistivity in hydrogen and deuterium: Temperature effect, *Materials*, 2019, **12**, 1–13, DOI: 10.3390/ma12213551.

98 A. Dyson and B. K. Ridley, Negative differential resistance associated with hot phonons, *J. Appl. Phys.*, 2012, **112**, 063707, DOI: 10.1063/1.4754012.

99 D. F. Guo, Switches with double carrier confinement structures for multiple-valued logic applications, *Semicond. Sci. Technol.*, 1998, **13**, 957–962, DOI: 10.1088/0268-1242/13/8/022.

100 S. Kumar, Z. Wang, N. Davila, N. Kumari, K. J. Norris, X. Huang, J. P. Strachan, D. Vine, A. L. D. Kilcoyne, Y. Nishi and R. S. Williams, Physical origins of current and temperature controlled negative differential resistances in NbO_2, *Nat. Commun.*, 2017, **8**, 658, DOI: 10.1038/s41467-017-00773-4.

101 Y. Ke, S. Wang, G. Liu, M. Li, T. J. White and Y. Long, Vanadium Dioxide: The Multistimuli Responsive Material and Its Applications, *Small*, 2018, **14**, 1–29, DOI: 10.1002/smll.201802025.

102 X. Hu, W. Wang, B. Sun, Y. Wang, J. Li and G. Zhou, Refining the Negative Differential Resistance Effect in a TiOx-Based Memristor, *J. Phys. Chem. Lett.*, 2021, **12**, 5377–5383, DOI: 10.1021/acs.jpclett.1c01420.

103 L. Yuan, J. A. Cooper, M. R. Melloch and K. J. Webb, Experimental demonstration of a silicon carbide IMPATT oscillator, *IEEE Electron Device Lett.*, 2001, **22**, 266–268, DOI: 10.1109/55.924837.

104 B. K. Ridley, Specific negative resistance in solids, *Proc. Phys. Soc.*, 1963, **82**, 954–966, DOI: 10.1088/0370-1328/82/6/315.

105 L. Chua, Memristor-The missing circuit element, *IEEE Trans. Circuit Theory*, 1971, **18**, 507–519, DOI: 10.1109/TCT.1971.1083337.

106 L. Chua, Resistance switching memories are memristors, *Appl. Phys. A:Mater. Sci. Process.*, 2011, **102**, 765–783, DOI: 10.1007/s00339-011-6264-9.

107 L. O. Chua and S. M. Kang, Memristive devices and systems, *Proc. IEEE*, 1976, **64**, 209–223, DOI: 10.1109/PROC.1976.10092.

108 D. B. Strukov, G. S. Snider, D. R. Stewart and R. S. Williams, The missing memristor found, *Nature*, 2008, **453**, 80–83, DOI: 10.1038/nature06932.

109 B. Sun, S. Ranjan, G. Zhou, T. Guo, Y. Xia, L. Wei, Y. N. Zhou and Y. A. Wu, Multistate resistive switching behaviors for neuromorphic computing in memristor, *Mater. Today Adv.*, 2021, **9**, 100125, DOI: 10.1016/j.mtadv.2020.100125.

110 R. Wang, J.-Q. Yang, J.-Y. Mao, Z.-P. Wang, S. Wu, M. Zhou, T. Chen, Y. Zhou and S.-T. Han, Recent Advances of Volatile Memristors: Devices, Mechanisms, and Applications, *Adv. Intell. Syst.*, 2020, **2**, 2000055, DOI: 10.1002/aisy.202000055.

111 M. A. Zidan, J. P. Strachan and W. D. Lu, The future of electronics based on memristive systems, *Nat. Electron.*, 2018, **1**, 22–29, DOI: 10.1038/s41928-017-0006-8.

112 K. Roy, A. Jaiswal and P. Panda, Towards spike-based machine intelligence with neuromorphic computing, *Nature*, 2019, **575**, 607–617, DOI: 10.1038/s41586-019-1677-2.

113 M. D. Pickett, D. B. Strukov, J. L. Borghetti, J. J. Yang, G. S. Snider, D. R. Stewart and R. S. Williams, Switching dynamics in titanium dioxide memristive devices, *J. Appl. Phys.*, 2009, **106**, 074508, DOI: 10.1063/1.3236506.

114 M. D. Pickett and R. S. Williams, Sub-100fJ and sub-nanosecond thermally driven threshold switching in niobium oxide crosspoint nanodevices, *Nanotechnology*, 2012, **23**, 215202, DOI: 10.1088/0957-4484/23/21/215202.

115 C. Wan, M. Pei, K. Shi, H. Cui, H. Long, L. Qiao, Q. Xing and Q. Wan, Toward a Brain–Neuromorphics Interface, *Adv. Mater.*, 2024, **36**, 2311288, DOI: 10.1002/adma.202311288.

116 J. J. Wang, S. G. Hu, X. T. Zhan, Q. Luo, Q. Yu, Z. Liu, T. P. Chen, Y. Yin, S. Hosaka and Y. Liu, Predicting House Price with a Memristor-Based Artificial Neural Network, *IEEE Access*, 2018, **6**, 16523–16528, DOI: 10.1109/ACCESS.2018.2814065.

117 P. Yao, H. Wu, B. Gao, J. Tang, Q. Zhang, W. Zhang, J. J. Yang and H. Qian, Fully hardware-implemented memristor convolutional neural network, *Nature*, 2020, **577**, 641–646, DOI: 10.1038/s41586-020-1942-4.

118 G. Yuan, X. Ma, C. Ding, S. Lin, T. Zhang, Z. S. Jalali, Y. Zhao, L. Jiang, S. Soundarajan and Y. Wang, An Ultra-Efficient Memristor-Based DNN Framework with Structured Weight Pruning and Quantization Using

ADMM, in *2019 IEEE/ACM Int. Symp. Low Power Electron. Des*, IEEE, 2019, pp. 1–6. DOI: **10.1109/ISLPED.2019.8824944**.

119 W. Wang, L. Li, H. Peng, J. Xiao and Y. Yang, Synchronization control of memristor-based recurrent neural networks with perturbations, *Neural Networks*, 2014, **53**, 8–14, DOI: **10.1016/j.neunet.2014.01.010**.

120 W. Zhang, C. Li, T. Huang and X. He, Synchronization of memristor-based coupling recurrent neural networks with time-varying delays and impulses, *IEEE Trans. Neural Netw. Learn. Syst.*, 2015, **26**, 3308–3313, DOI: **10.1109/TNNLS.2015.2435794**.

121 X. Zhang, Z. Wu, J. Lu, J. Wei, J. Lu, J. Zhu, J. Qiu, R. Wang, K. Lou, Y. Wang, T. Shi, C. Dou, D. Shang, Q. Liu and M. LiuFully memristive SNNs with temporal coding for fast and low-power edge computing, presented at the 2020 IEEE International Electron Devices Meeting (IEDM), San Francisco, CA, USA, 2020, pp. 29.6.1–29.6.4, DOI: **10.1109/IEDM13553.2020.9371937**.

122 Y. Xiao, B. Jiang, Z. Zhang, S. Ke, Y. Jin, X. Wen and C. Ye, A review of memristor: material and structure design, device performance, applications and prospects, *Sci. Technol. Adv. Mater.*, 2023, **24**, 2162323, DOI: **10.1080/14686996.2022.2162323**.

123 C. Yang, H. Wang, Z. Cao, X. Chen, G. Zhou, H. Zhao, Z. Wu, Y. Zhao and B. Sun, Memristor–Based Bionic Tactile Devices: Opening the Door for Next–Generation Artificial Intelligence, *Small*, 2024, **20**, 23088918, DOI: **10.1002/smll.202308918**.

124 I. Valov, Redox–Based Resistive Switching Memories (ReRAMs): Electrochemical Systems at the Atomic Scale, *ChemElectroChem*, 2014, **1**, 26–36, DOI: **10.1002/celc.201300165**.

125 Y. Wang, R. B. Comes, S. A. Wolf and J. Lu, Threshold Switching Characteristics of Nb/NbO$_2$/TiN Vertical Devices, *IEEE J. Electron Devices Soc.*, 2016, **4**, 11–14, DOI: **10.1109/JEDS.2015.2503922**.

126 P. Chen, X. Zhang, Q. Liu and M. Liu, NbO$_2$-based locally active memristors: from physical mechanisms to performance optimization, *Appl. Phys. A*, 2022, **128**, 1113, DOI: **10.1007/s00339-022-06258-6**.

127 D. Kuzum, S. Yu and H.-S. P. Wong, Synaptic electronics: materials, devices and applications, *Nanotechnology*, 2013, **24**, 382001, DOI: **10.1088/0957-4484/24/38/382001**.

128 M. D. Pickett, G. Medeiros-Ribeiro and R. S. Williams, A scalable neuristor built with Mott memristors, *Nat. Mater.*, 2013, **12**, 114–117, DOI: **10.1038/nmat3510**.

129 G. Kim, J. H. In, Y. Lee, H. Rhee, W. Park, H. Song, J. Park, J. B. Jeon, T. D. Brown, A. A. Talin, S. Kumar and K. M. Kim, Mott neurons with dual thermal dynamics for spatiotemporal computing, *Nat. Mater.*, 2024, **23**, 1237–1244, DOI: **10.1038/s41563-024-01913-0**.

130 S. Li, X. Liu, S. K. Nandi, D. K. Venkatachalam and R. G. Elliman, High-endurance megahertz electrical self-oscillation in Ti/NbO$_x$ bilayer structures, *Appl. Phys. Lett.*, 2015, **106**, 212902, DOI: **10.1063/1.4921745**.

131 C. Delacour and A. Todri-Sanial, Mapping Hebbian Learning Rules to Coupling Resistances for Oscillatory Neural Networks, *Front. Neurosci.*, 2021, **15**, 694549, DOI: **10.3389/fnins.2021.694549**.

132 J. Ying, F. Min and G. Wang, Neuromorphic behaviors of VO$_2$ memristor-based neurons, *Chaos, Solitons Fractals*, 2023, **175**, 114058, DOI: **10.1016/j.chaos.2023.114058**.

133 C. Y. Han, Z. R. Han, S. L. Fang, S. Q. Fan, J. Q. Yin, W. H. Liu, X. Li, S. Q. Yang, G. H. Zhang, X. L. Wang and L. Geng, Characterization and Modelling of Flexible VO$_2$ Mott Memristor for the Artificial Spiking Warm Receptor, *Adv. Mater. Interfaces*, 2022, **9**, 2200394, DOI: **10.1002/admi.202200394**.

134 K. L. Chopra, Current-Controlled Negative Resistance in Thin Niobium Oxide Films, *Proc. IEEE*, 1963, **51**, 941–942, DOI: **10.1109/PROC.1963.2339**.

135 D. V. Geppert, A new negative-resistance device, *Proc. IEEE*, 1963, **51**, 223–223, DOI: **10.1109/PROC.1963.1689**.

136 W. R. Hiatt and T. W. Hickmott, Bistable switching in niobium oxide diodes, *Appl. Phys. Lett.*, 1965, **6**, 106–108, DOI: **10.1063/1.1754187**.

137 T. W. Hickmott, Electroluminescence, Bistable Switching, and Dielectric Breakdown of Nb$_2$O$_5$ Diodes, *J. Vac. Sci. Technol.*, 1969, **6**, 828–833, DOI: **10.1116/1.1492715**.

138 T. W. Hickmott and W. R. Hiatt, Electrode effects and bistable switching of amorphous Nb$_2$O$_5$ diodes, *Solid-State Electron.*, 1970, **13**, 1033–1047, DOI: **10.1016/0038-1101(70)90100-0**.

139 G. Gaule, P. LaPlante, S. Levy and S. Schneider, Metal-oxide devices for rapid high current switching, in *1976 Int. Electron Devices Meet., IRE*, 1976, pp. 279–282. DOI: **10.1109/IEDM.1976.189038**.

140 H. R. Philipp and L. M. Levinson, NbO$_2$ devices for subnanosecond transient protection, *J. Appl. Phys.*, 1979, **50**, 4814–4822, DOI: **10.1063/1.326544**.

141 G. C. Vezzoli, Recovery curve for threshold-switching NbO$_2$, *J. Appl. Phys.*, 1979, **50**, 6390–6395, DOI: **10.1063/1.325730**.

142 G. C. Vezzoli, L. W. Doremus, S. Levy, G. K. Gaulé, B. Lalevic and M. Shoga, The on-state of single-crystal and polycrystalline NbO$_2$, *J. Appl. Phys.*, 1981, **52**, 833–839, DOI: **10.1063/1.328424**.

143 J. C. Lee and W. W. Durand, Electrically stimulated optical switching of NbO$_2$ thin films, *J. Appl. Phys.*, 1984, **56**, 3350–3352, DOI: **10.1063/1.333863**.

144 Y. L. Boiko, B. T. Pancheha, P. A. Kopach and V. Pozdeev, Transformations in a metal/insulator/semiconductor structure with an amorphous insulator film caused by contacts, *Thin Solid Films*, 1985, **130**, 341–355, DOI: **10.1016/0040-6090(85)90365-7**.

145 V. Eyert, The metal-insulator transition of NbO$_2$: An embedded Peierls instability, *Europhys. Lett.*, 2002, **58**, 851–856, DOI: **10.1209/epl/i2002-00452-6**.

146 G. A. Gibson, Designing Negative Differential Resistance Devices Based on Self–Heating, *Adv. Funct. Mater.*, 2018, **28**, 1704175, DOI: **10.1002/adfm.201704175**.

147 A. H. Wilson, The theory of electronic semi-conductors, *Proc. R. Soc. Lond. A*, 1931, **133**, 458–491, DOI: **10.1098/rspa.1931.0162**.

148 S. Li, X. Liu, S. K. Nandi, S. K. Nath and R. G. Elliman, Origin of current-controlled negative differential resistance modes and the emergence of composite characteristics with high complexity, *Adv. Funct. Mater.*, 2019, **29**, 1905060, DOI: **10.1002/adfm.201905060**.

149 A. Gadó, P. Holmberg, B. Magnéli and A. Kallner, Wolfram Tantalum and Wolfram Niobium Oxides of the $MnO_{3n-2}(ReO_3)$ Series, *Acta Chem. Scand.*, 1965, **19**, 2010–2011, DOI: **10.3891/ACTA.CHEM.SCAND.19-2010**.

150 J. B. Goodenough, Narrow-band electrons in transition-metal oxides, *Czech. J. Phys.*, 1967, **17**, 304–336, DOI: **10.1007/BF01691621**.

151 T. W. Hickmott, Impurity conduction and negative resistance in thin oxide films, *J. Appl. Phys.*, 1964, **35**, 2118–2122, DOI: **10.1063/1.1702801**.

152 J. Park, E. Cha, I. Karpov and H. Hwang, Dynamics of electroforming and electrically driven insulator-metal transition in NbO_x selector, *Appl. Phys. Lett..*, 2016, **108**, 232101, DOI: **10.1063/1.4953323**.

153 Z. Zhou, M. Yang, Z. Fu, H. Wang, X. Ma and H. Gao, Electrode-induced polarity conversion in Nb_2O_5/NbO_x resistive switching devices, *Appl. Phys. Lett..*, 2020, **117**, 243502, DOI: **10.1063/5.0020501**.

154 S. K. Nandi, S. K. Nath, A. E. El-Helou, S. Li, T. Ratcliff, M. Uenuma, P. E. Raad and R. G. Elliman, Electric Field-And Current-Induced Electroforming Modes in NbO_x, *ACS Appl. Mater. Interfaces*, 2020, **12**, 8422–8428, DOI: **10.1021/acsami.9b20252**.

155 K. Jung, Y. Kim, Y. S. Park, W. Jung, J. Choi, B. Park, H. Kim, W. Kim, J. Hong and H. Im, Unipolar resistive switching in insulating niobium oxide film and probing electroforming induced metallic components, *J. Appl. Phys.*, 2011, **109**, 054511, DOI: **10.1063/1.3552980**.

156 J. Lee, J. Kim, T. Kim and H. Sohn, Negative Differential Resistance Characteristics in Forming–Free NbO_x with Crystalline NbO_2 Phase, *Phys. Status Solidi RRL*, 2021, **15**, 2000610, DOI: **10.1002/pssr.202000610**.

157 F. A. Chudnovskii, L. L. Odynets, A. L. Pergament and G. B. Stefanovich, Electroforming and switching in oxides of transition metals: The role of metal-insulator transition in the switching mechanism, *J. Solid State Chem.*, 1996, **122**, 95–99, DOI: **10.1006/jssc.1996.0087**.

158 J. Lee, J. Kim, J. Jeong and H. Sohn, Electroforming and threshold switching characteristics of NbO_x films with crystalline NbO_2 phase, *J. Vac. Sci. Technol., B:Nanotechnol. Microelectron.:Mater., Process., Meas., Phenom.*, 2021, **39**, 053206, DOI: **10.1116/6.0001215**.

159 M. C. Cross and D. S. Fisher, A new theory of the spin-Peierls transition with special relevance to the experiments on TTFCuBDT, *Phys. Rev. B: Condens. Matter Mater. Phys.*, 1979, **19**, 402–419, DOI: **10.1103/PhysRevB.19.402**.

160 P. A. Lee, T. M. Rice and P. W. Anderson, Fluctuation effects at a peierls transition, *Phys. Rev. Lett.*, 1973, **31**, 462–465, DOI: **10.1103/PhysRevLett.31.462**.

161 K. Luo and X. Dai, Transverse Peierls Transition, *Phys. Rev. X*, 2023, **13**, 11027, DOI: **10.1103/PhysRevX.13.011027**.

162 A. O'Hara, T. N. Nunley, A. B. Posadas, S. Zollner and A. A. Demkov, Electronic and optical properties of NbO_2, *J. Appl. Phys.*, 2014, **116**, 115135, DOI: **10.1063/1.4903067**.

163 C. Nico, T. Monteiro and M. P. F. Graça, Niobium oxides and niobates physical properties: Review and prospects, *Prog. Mater. Sci.*, 2016, **80**, 1–37, DOI: **10.1016/j.pmatsci.2016.02.001**.

164 G. J. Páez Fajardo, S. A. Howard, E. Evlyukhin, M. J. Wahila, W. R. Mondal, M. Zuba, J. E. Boschker, H. Paik, D. G. Schlom, J. T. Sadowski, S. A. Tenney, B. Reinhart, W. C. Lee and L. F. J. Piper, Structural Phase Transitions of NbO_2: Bulk versus Surface, *Chem. Mater.*, 2021, **33**, 1416–1425, DOI: **10.1021/acs.chemmater.0c04566**.

165 R. M. Axe, J. D. Pynn and R. Thomas, Neutron scattering studies of the structural phase transformation in NbO_2, *Ferroelectrics*, 1977, **16**, 149–151, DOI: **10.1080/00150197708237142**.

166 A. O'Hara and A. A. Demkov, Nature of the metal-insulator transition in NbO_2, *Phys. Rev. B: Condens. Matter Mater. Phys.*, 2015, **91**, 094305, DOI: **10.1103/PhysRevB.91.094305**.

167 M. J. Wahila, G. Paez, C. N. Singh, A. Regoutz, S. Sallis, M. J. Zuba, J. Rana, M. B. Tellekamp, J. E. Boschker, T. Markurt, J. E. N. Swallow, L. A. H. Jones, T. D. Veal, W. Yang, T.-L. Lee, F. Rodolakis, J. T. Sadowski, D. Prendergast, W.-C. Lee, W. A. Doolittle and L. F. J. Piper, Evidence of a second-order Peierls-driven metal-insulator transition in crystalline NbO_2, *Phys. Rev. Mater.*, 2019, **3**, 074602, DOI: **10.1103/PhysRevMaterials.3.074602**.

168 S. W. Olin, S. A. Razek, L. F. J. Piper and W. C. Lee, Mechanism of the Resistivity Switching Induced by the Joule Heating in Crystalline NbO_2, *Adv. Quantum Technol.*, 2022, **5**, 2200067, DOI: **10.1002/qute.202200067**.

169 G. A. Gibson, S. Musunuru, J. Zhang, K. Vandenberghe, J. Lee, C.-C. Hsieh, W. Jackson, Y. Jeon, D. Henze, Z. Li and R. S. Williams, An accurate locally active memristor model for S-type negative differential resistance in NbOx, *Appl. Phys. Lett.*, 2016, **108**, 02305, DOI: **10.1063/1.4939913**.

170 X. Liu, S. Li, S. K. Nandi, D. K. Venkatachalam and R. G. Elliman, Threshold switching and electrical self-oscillation in niobium oxide films, *J. Appl. Phys.*, 2016, **120**, 124102, DOI: **10.1063/1.4963288**.

171 P. Chen, X. Zhang, J. Qiu, Y. Li, S. Jia, L. Cheng, D. Yang, X. Wang, J. Chen, X. Chen, M. Wang, Q. Liu and M. Liu, Thermal Engineering of NbO_2 –Based Memristor for Low–Power and High–Capacity Oscillatory Neural Networks, *Adv. Funct. Mater.*, 2025, 2423800, DOI: **10.1002/adfm.202423800**.

172 I. Messaris, A. S. Demirkol, A. Ascoli, V. Ntinas, D. Prousalis, N. Schmitt and R. Tetzlaff, Frequency Dependent Bistability in a Volatile Threshold Switch, in *2024 13th Int. Conf. Mod. Circuits Syst. Technol*, IEEE, 2024, pp. 1–4. DOI: **10.1109/MOCAST61810.2024.10615946**.

173 S. K. Nandi, S. K. Nath, A. E. El-Helou, S. Li, X. Liu, P. E. Raad and R. G. Elliman, Current Localization and Redistribution as the Basis of Discontinuous Current Controlled Negative Differential Resistance in NbO_x, *Adv. Funct. Mater.*, 2019, **29**, 1906731, DOI: **10.1002/adfm.201906731**.

174 K. Seta and K. Naito, Calorimetric study of the phase transition in doped NbO_2, *J. Chem. Thermodyn.*, 1982, **14**, 937–949, DOI: **10.1016/0021-9614(82)90003-9**.

175 H. Schroeder, Poole-Frenkel-effect as dominating current mechanism in thin oxide films—An illusion?!, *J. Appl. Phys.*, 2015, **117**, 215103, DOI: **10.1063/1.4921949**.

176 S. Slesazeck, H. Mähne, H. Wylezich, A. Wachowiak, J. Radhakrishnan, A. Ascoli, R. Tetzlaff and T. Mikolajick, Physical model of threshold switching in NbO_2 based memristors, *RSC Adv.*, 2015, **5**, 102318–102322, DOI: **10.1039/c5ra19300a**.

177 G. A. Gibson, Designing Negative Differential Resistance Devices Based on Self-Heating, *Adv. Funct. Mater.*, 2018, **28**, 1704175, DOI: **10.1002/adfm.201704175**.

178 F.-C. Chiu, A Review on Conduction Mechanisms in Dielectric Films, *Adv. Mater. Sci. Eng.*, 2014, **2014**, 578168, DOI: **10.1155/2014/578168**.

179 J. R. Yeargan and H. L. Taylor, The Poole-Frenkel effect with compensation present, *J. Appl. Phys.*, 1968, **39**, 5600–5604, DOI: **10.1063/1.1656022**.

180 R. M. Hill, Poole-frenkel conduction in amorphous solids, *Philos. Mag.*, 1971, **23**, 59–86, DOI: **10.1080/14786437108216365**.

181 Q. Luo, J. Yu, X. Zhang, K.-H. Xue, J.-H. Yuan, Y. Cheng, T. Gong, H. Lv, X. Xu, P. Yuan, J. Yin, L. Tai, S. Long, Q. Liu, X. Miao, J. Li and M. Liu, $Nb_{1-x}O_2$ based Universal Selector with Ultra-high Endurance (>10 ^{12}), high speed (10 ns) and Excellent V th Stability, in *2019 Symp, VLSI Technol, IEEE*, 2019, pp. 236–T237, DOI: **10.23919/VLSIT.2019.8776546**.

182 J. Wu, T. Hu, Y. Yin, J. Li, W. Zhou, Y. Gao, L. Jiang, Z. Huang and J. Chu, Current-controlled negative differential resistance in small-polaron hopping system, *AIP Adv.*, 2019, **9**, 055223, DOI: **10.1063/1.5097616**.

183 C. Funck, S. Menzel, N. Aslam, H. Zhang, A. Hardtdegen, R. Waser and S. Hoffmann-Eifert, Multidimensional Simulation of Threshold Switching in NbO_2 Based on an Electric Field Triggered Thermal Runaway Model, *Adv. Electron. Mater.*, 2016, **2**, 1600169, DOI: **10.1002/aelm.201600169**.

184 C. Ruscher, E. Salje and A. Hussain, The effect of high polaron concentration on the polaron transport in $NbO_{2.5-x}$: Optical and electrical properties, *J. Phys. C:Solid State Phys.*, 1988, **21**, 3737–3749, DOI: **10.1088/0022-3719/21/20/009**.

185 S. K. Nath, S. K. Nandi, T. Ratcliff and R. G. Elliman, Engineering the threshold switching response of Nb_2O_5-Based memristors by Ti doping, *ACS Appl. Mater. Interfaces*, 2021, **13**, 2845–2852, DOI: **10.1021/acsami.0c19544**.

186 Z. Wang, S. Kumar, R. S. Williams, Y. Nishi and H.-S. P. Wong, Intrinsic limits of leakage current in self-heating-triggered threshold switches, *Appl. Phys. Lett.*, 2019, **114**, 183501, DOI: **10.1063/1.5089261**.

187 S. Kumar, R. S. Williams and Z. Wang, Third-order nanocircuit elements for neuromorphic engineering, *Nature*, 2020, **585**, 518–523, DOI: **10.1038/s41586-020-2735-5**.

188 X. Liu, P. Zhang, S. K. Nath, S. Li, S. K. Nandi and R. G. Elliman, Understanding composite negative differential resistance in niobium oxide memristors, *J. Phys. D: Appl. Phys.*, 2022, **55**, 105016, DOI: **10.1088/1361-6463/ac3bf4**.

189 S. K. Nath, S. K. Nandi, A. El-Helou, X. Liu, S. Li, S. Li, T. Ratcliff, P. E. Raad and R. G. Elliman, Schottky-barrier-induced asymmetry in the negative-differential-resistance response of Nb/NbO_x/Pt cross-point devices, *Phys. Rev. Appl.*, 2020, **13**, 1, DOI: **10.1103/PhysRevApplied.13.064024**.

190 S. Kim, S. Choi and W. Lu, Comprehensive physical model of dynamic resistive switching in an oxide memristor, *ACS Nano*, 2014, **8**, 2369–2376, DOI: **10.1021/nn405827t**.

191 J. P. Wright, S. A. Sarles and J. S. Pei, DC operating points of Mott neuristor circuits, *Microelectron. Eng.*, 2024, **284–285**, 112124, DOI: **10.1016/j.mee.2023.112124**.

192 J. M. Ang, P. A. Dananjaya, S. C. W. Chow, G. J. Lim, C. S. Seet and W. S. Lew, Enhancement of temperature-modulated NbO_2 -based relaxation oscillator via interfacial and bulk treatments, *Nanotechnology*, 2023, **34**, 185202, DOI: **10.1088/1361-6528/acb778**.

193 D. Chen, A. Chen, Z. Yu, Z. Zhang, Q. Tan, J. Zeng, J. Ji, X. Pan, G. Ma, H. Wan, Y. Rao, L. Tao, X. Peng, J. Duan, H. Wang and T. C. Chang, Forming-free, ultra-high on-state current, and self-compliance selector based on titanium-doped NbO_x thin films, *Ceram. Int.*, 2021, **47**, 22677–22682, DOI: **10.1016/j.ceramint.2021.04.282**.

194 W. Park, G. Kim, J. H. In, H. Rhee, H. Song, J. Park, A. Martinez and K. M. Kim, High Amplitude Spike Generator in Au Nanodot-Incorporated NbO_x Mott Memristor, *Nano Lett.*, 2023, **23**, 5399–5407, DOI: **10.1021/acs.nanolett.2c04599**.

195 A. Chen, Y. Fu, G. Ma, G. Yang, N. Liu, X. Zhao, Z. Zhang, L. Tao, H. Wan, Y. Rao, J. Duan, L. Shen, J. Zhang, P. Sun, D. Yang, T. C. Chang and H. Wang, The Co-Improvement of Selectivity and Uniformity on NbO_X-Based Selector by Al-Doping, *IEEE Electron Device Lett.*, 2022, **43**, 870–873, DOI: **10.1109/LED.2022.3165789**.

196 G. Ma, Z. Yang, A. Chen, X. Wan, N. Liu, X. Zhao, Z. Yu and H. Wang, Improved Selectivity and Reliability in NbO_x-Based Selector by Co-Approaches of Al Doping and Ta Interlayer, *IEEE Electron Device Lett.*, 2022, **43**, 1444–1446, DOI: **10.1109/LED.2022.3195275**.

197 S. Li, X. Liu, S. K. Nandi and R. G. Elliman, Anatomy of filamentary threshold switching in amorphous niobium oxide, *Nanotechnology*, 2018, **29**, 375705, DOI: **10.1088/1361-6528/aacee4**.

198 S. K. Nandi, S. K. Nath, S. K. Das, B. J. Murdoch, T. Ratcliff, D. G. McCulloch and R. G. Elliman, Effect of Interdiffusion and Crystallization on Threshold Switching Characteristics of Nb/Nb_2O_5/Pt Memristors, *ACS Appl. Mater. Interfaces*, 2023, **15**, 58613–58622, DOI: **10.1021/acsami.3c14431**.

199 S. K. Nandi, S. Li, X. Liu and R. G. Elliman, Temperature dependent frequency tuning of NbO_x relaxation oscillators, *Appl. Phys. Lett.*, 2017, **111**, 202901, DOI: **10.1063/1.4999373**.

200 J. Zhu, X. Zhang, R. Wang, M. Wang, P. Chen, L. Cheng, Z. Wu, Y. Wang, Q. Liu and M. Liu, A Heterogeneously Integrated Spiking Neuron Array for Multimode–Fused Perception and Object Classification, *Adv. Mater.*, 2022, **34**, 1–9, DOI: **10.1002/adma.202200481**.

201 M. Herzig, M. Weiher, A. Ascoli, R. Tetzlaff, T. Mikolajick and S. Slesazeck, Multiple slopes in the negative differential resistance region of NbO_x -based threshold switches, *J. Phys. D:Appl. Phys.*, 2019, **52**, 325104, DOI: **10.1088/1361-6463/ab217a**.

202 S. K. Nath, S. K. Nandi, S. K. Das, Y. Liang and R. G. Elliman, Thermal transport in metal-NbOx-metal cross-point devices and its effect on threshold switching characteristics, *Nanoscale*, 2023, **15**, 7559–7565, DOI: **10.1039/d3nr00173c**.

203 G. Leonetti, M. Fretto, F. C. Pirri, N. De Leo, I. Valov and G. Milano, Effect of electrode materials on resistive switching behaviour of NbO_x-based memristive devices, *Sci. Rep.*, 2023, **13**, 17003, DOI: **10.1038/s41598-023-44110-w**.

204 B. C. Bao, Z. Liu and J. P. Xu, Steady periodic memristor oscillator with transient chaotic behaviours, *Electron. Lett.*, 2010, **46**, 228–230, DOI: **10.1049/el.2010.3114**.

205 H. Lin, C. Wang, Q. Hong and Y. Sun, A Multi-Stable Memristor and its Application in a Neural Network, *IEEE Trans. Circuits Syst.*, 2020, **67**, 3472–3476, DOI: **10.1109/TCSII.2020.3000492**.

206 C. Wang, Z. Si, X. Jiang, A. Malik, Y. Pan, S. Stathopoulos, A. Serb, S. Wang, T. Prodromakis and C. Papavassiliou, Multi-State Memristors and Their Applications: An Overview, *IEEE J. Emerg. Sel. Topics Circuits Syst.*, 2022, **12**, 723–734, DOI: **10.1109/JETCAS.2022.3223295**.

207 J. Ying, G. Wang, Y. Dong and S. Yu, Switching Characteristics of a Locally-Active Memristor with Binary Memories, *Int. J. Bifurc. Chaos*, 2019, **29**, 1930030, DOI: **10.1142/S0218127419300301**.

208 A. Ascoli, N. Schmitt, I. Messaris, A. S. Demirkol, R. Tetzlaff and L. O. Chua, The State Change Per Cycle Map: a novel system-theoretic analysis tool for periodically-driven ReRAM cells, *Front. Electron. Mater.*, 2023, **3**, 1–19, DOI: **10.3389/femat.2023.1228899**.

209 N. Schmitt, A. Ascoli, I. Messaris, A. S. Demirkol, S. Menzel, V. Rana, R. Tetzlaff and L. O. Chua, Theoretico-experimental analysis of bistability in the oscillatory response of a TaO_x ReRAM to pulse train stimuli, *Frontal Nanotechnol.*, 2024, **6**, 1–30, DOI: **10.3389/fnano.2024.1301320**.

210 I. Messaris, A. Ascoli, A. S. Demirkol and R. Tetzlaff, High Frequency Response of Non-Volatile Memristors, *IEEE Trans. Circuits Syst. I: Regul. Pap.*, 2023, **70**, 566–578, DOI: **10.1109/TCSI.2022.3219368**.

211 Y. V. Pershin and V. A. Slipko, Bifurcation analysis of a TaO memristor model, *J. Phys. D:Appl. Phys.*, 2019, **52**, 505304, DOI: **10.1088/1361-6463/ab4537**.

212 A. Ascoli, N. Schmitt, I. Messaris, A. S. Demirkol, J. P. Strachan, R. Tetzlaff and L. Chua, An analytical approach to engineer multistability in the oscillatory response of a pulse-driven ReRAM, *Sci. Rep.*, 2024, **14**, 5626, DOI: **10.1038/s41598-024-55255-7**.

213 J. Qiu, P. Chen, M. Wang, D. Yang, J. Cao, M. Liu, J. Yu, X. Zhang, H. Cheng, Q. Liu and M. Liu, Compact Artificial Synapse-Neuron Module with Chemically Mediated Spiking Behaviors, *ACS Nano*, 2025, **19**, 12298–12307, DOI: **10.1021/acsnano.5c01406**.

214 Y. Xiao, Y. Liu, B. Zhang, P. Chen, H. Zhu, E. He, J. Zhao, W. Huo, X. Jin, X. Zhang, H. Jiang, D. Ma, Q. Zheng, H. Tang, P. Lin, W. Kong and G. Pan, Bio-plausible reconfigurable spiking neuron for neuromorphic computing, *Sci. Adv.*, 2025, **11**, eadr6733, DOI: **10.1126/sciadv.adr6733**.

215 S. Kim, J. Heo, S. Kim and M.-H. Kim, Dual functionality of NbO x memristors for synaptic and neuronal emulations in advanced neuromorphic systems, *J. Mater. Chem. C*, 2024, **12**, 16294–16308, DOI: **10.1039/D4TC03212H**.

216 Y. Wang, H. Xu, W. Wang, X. Zhang, Z. Wu, R. Gu, Q. Li and Q. Liu, A Configurable Artificial Neuron Based on a Threshold-Tunable TiN/NbO_x/Pt Memristor, *IEEE Electron Device Lett.*, 2022, **43**, 631–634, DOI: **10.1109/LED.2022.3150034**.

217 X. Zhang, W. Wang, Q. Liu, X. Zhao, J. Wei, R. Cao, Z. Yao, X. Zhu, F. Zhang, H. Lv, S. Long and M. Liu, An Artificial Neuron Based on a Threshold Switching Memristor, *IEEE Electron Device Lett.*, 2018, **39**, 308–311, DOI: **10.1109/LED.2017.2782752**.

218 X. Zhang, Z. Wu and L. Chua, Hearts are Poised near the Edge of Chaos, *Int. J. Bifurc. Chaos*, 2020, **30**, 2030023, DOI: **10.1142/S0218127420300232**.

219 L. Chua, V. Sbitnev and H. Kim, Neurons are poised near the edge of chaos, *Int. J. Bifurc. Chaos*, 2012, **22**, 1250098, DOI: **10.1142/S0218127412500988**.

220 Y. Yang, X. Zhang, P. Chen, L. Cheng, C. Li, Y. Ding and Q. Liu, Memristive Hodgkin–Huxley Neurons with Diverse Firing Patterns for High–Order Neuromorphic Computing, *Adv. Intell. Syst.*, 2025, **7**, 2400383, DOI: **10.1002/aisy.202400383**.

221 P. Chen, X. Zhang, Z. Wu, Y. Wang, J. Zhu, Y. Hao, G. Feng, Y. Sun, T. Shi, M. Wang and Q. Liu, High-Yield and Uniform NbO_x-Based Threshold Switching Devices for Neuron Applications, *IEEE Trans. Electron Devices*, 2022, **69**, 2391–2397, DOI: **10.1109/TED.2022.3161614**.

222 Y. Liang, S. Wang, Z. Lu, Y. Li and K. Wang, Designing a Fully Current-Controlled Memristors-Based Oscillator, *Int. J. Bifurc. Chaos*, 2024, **34**, 2450042, DOI: 10.1142/S0218127424500421.

223 Y. Yan, P. Jin, J. Shi, G. Wang, Y. Liang, Y. Dong and L. Chen, Neuron circuit made of a single locally-active memristor, *Mod. Phys. Lett. B*, 2025, **39**, 2550042, DOI: 10.1142/S0217984925500423.

224 Y. Li, J. Lu, D. Shang, Q. Liu, S. Wu, Z. Wu, X. Zhang, J. Yang, Z. Wang, H. Lv and M. Liu, Oxide–Based Electrolyte–Gated Transistors for Spatiotemporal Information Processing, *Adv. Mater.*, 2020, **32**, 2003018, DOI: 10.1002/adma.202003018.

225 F. Li, D. Li, C. Wang, G. Liu, R. Wang, H. Ren, Y. Tang, Y. Wang, Y. Chen, K. Liang, Q. Huang, M. Sawan, M. Qiu, H. Wang and B. Zhu, An artificial visual neuron with multiplexed rate and time-to-first-spike coding, *Nat. Commun.*, 2024, **15**, 3689, DOI: 10.1038/s41467-024-48103-9.

226 D. Li, G. Liu, F. Li, H. Ren, Y. Tang, Y. Chen, Y. Wang, R. Wang, S. Wang, L. Xing, Q. Huang and B. Zhu, Double-opponent spiking neuron array with orientation selectivity for encoding and spatial-chromatic processing, *Sci. Adv.*, 2025, **11**, eadt3584, DOI: 10.1126/sciadv.adt3584.

227 Z. Lu, F. Zeng, D. Ma, Q. Wan, J. Yu and F. Pan, Modulation of Phase-Locking Characteristics of NbO_x Memristor by Ag Doping, *ACS Appl. Mater. Interfaces*, 2024, **16**, 60501–60510, DOI: 10.1021/acsami.4c12956.

228 Y. Li, Y. Liu, W. Sun, C. G. Jenson, S. M. Sadaf, Q. Yu, J. Song, Y. Zhang and X. Liu, Asymmetrical response of NbO_2 -based neuristor for three-dimensional sound localization, *J. Phys. D:Appl. Phys.*, 2025, **58**, 245302, DOI: 10.1088/1361-6463/adde6d.

229 Y. Zhang, Z. Wang, J. Zhu, Y. Yang, M. Rao, W. Song, Y. Zhuo, X. Zhang, M. Cui, L. Shen, R. Huang and J. J. Yang, Brain-inspired computing with memristors: Challenges in devices, circuits, and systems, *Appl. Phys. Rev.*, 2020, **7**, 011308, DOI: 10.1063/1.5124027.

230 Z. Lu, Q. Zhu, S. Shi, K. Wang and Y. Liang, Nb 2 O 5 memristive neurons–based unsupervised learning network, *Int J Circuit Theory Appl*, 2024, **52**, 5554–5571, DOI: 10.1002/cta.4044.

231 J. P. Keener, Analog Circuitry for the van der Pol and FitzHugh–Nagumo Equations, *IEEE Transactions on Systems, Man, and Cybernetics*, 1983, **SMC-13**, 1010–1014, DOI: 10.1109/TSMC.1983.6313098.

232 J. Rinzel, A Formal Classification of Bursting Mechanisms in Excitable Systems, In *Mathematical Topics in Population Biology, Morphogenesis and Neurosciences*, 1987, vol. 71, pp. 267–281, DOI: 10.1007/978-3-642-93360-8_26.

233 Y. Pei, B. Yang, X. Zhang, H. He, Y. Sun, J. Zhao, P. Chen, Z. Wang, N. Sun, S. Liang, G. Gu, Q. Liu, S. Li and X. Yan, Ultra robust negative differential resistance memristor for hardware neuron circuit implementation, *Nat. Commun.*, 2025, **16**, 48, DOI: 10.1038/s41467-024-55293-9.

234 P. Boriskov and A. Velichko, Switch elements with S-shaped current-voltage characteristic in models of neural oscillators, *Electronics*, 2019, **8**, 922, DOI: 10.3390/electronics8090922.

235 A. Pergament, G. Stefanovich, V. Malinenko and A. Velichko, Electrical Switching in Thin Film Structures Based on Transition Metal Oxides, *Adv. Condens. Matter Phys.*, 2015, **2015**, 654840, DOI: 10.1155/2015/654840.

236 C. Chen, M. Chai, M. Jin and T. He, Terahertz Metamaterial Absorbers, *Adv. Mater. Technol.*, 2022, **7**, 2101171, DOI: 10.1002/admt.202101171.